



UNIVERSITEIT • STELLENBOSCH • UNIVERSITY
jou kennisvenoot • your knowledge partner

Metrology and modelling of high frequency probes

J. Badenhorst

Thesis presented in partial fulfilment of the requirements for the
degree of Master of Science in Engineering at the University of

Stellenbosch

Supervisor: Prof. H.C. Reader

March 2008

Declaration

I, the undersigned, hereby declare that the work contained in this thesis is my own original work and that I have not previously in its entirety or in part submitted it at any university for a degree.

Signature:

Date:

Abstract

This study investigates high frequency probes through good metrology and computation software such as CST. A factor that can strongly influence the accuracy of measurements, is common mode (CM) current. Therefore, the main focus of this project was the CM current on the outside of an SMA, flanged, probe used for measuring material properties.

In the course of the investigation, a clamp-on CM current probe (CP) was calibrated using a CST model and good measurements. This calibration data indicated that the CP was invasive on the measurement setup and could not deliver the accuracy required for the CM current measurement.

In light of this, a second method was implemented where the material probe was placed within a cylindrical shield. A cavity was formed between the probe and the walls of the shield in which the electric fields could be simulated and measured. These field measurements allowed measurements to be conducted in both the time- (TD) and frequency-domain (FD).

For the TD measurements, a sampling oscilloscope was used. As the basic principle of a sampling oscilloscope differs from its real-time counterpart, this principle, as well as the systematic errors associated with these devices, was explored.

The results of the final measurements indicated that the TD results were within an acceptable range of both the FD results, measured on the VNA, and the results predicted by CST. This study shows that CST can be used to simulate complex measurement setups and deliver reliable results in cases where an accurate measurement cannot be guaranteed.

Opsomming

Hierdie studie ondersoek hoë frekwensie probes deur goeie metrologie en berekening sagteware soos CST. 'n Faktor wat goeie metings sterk kan beïnvloed, is gemene modus (GM) stroom. Die hoof fokus van die studie was om die GM stroom aan die buitekant van 'n SMA probe te meet, hierdie probe word gebruik om elektriese eienskappe van materiale te meet.

Gedurende die studie was 'n GM aanknip stroom probe (SP) gekalibreer deur die gebruik van 'n CST model en akkurate metings. Die data van die kalibrasie het daarop gedui dat die SP 'n indringing maak op die meet opstelling en nie die nodige akkuraatheid lewer vir die GM stroom nie.

As gevolg van dié rede is 'n tweede metode geïmplementeer waar die materiale probe in 'n silinderies afskerming geplaas was. Hierdie vorm 'n holte tussen die probe en die afskerming wat toelaat dat die elektriese velde gesimuleer en gemeet kan word. Hierdie metings laat toe dat dit in beide die tyd (TG) en frekwensie gebied (FG) gemeet kan word.

Vir die TG metings was 'n versyferings ossilloskoop gebruik. Die versyferings ossilloskoop werk op 'n verskillende beginsel as die van normale ossilloskope. Hierdie beginsel asook die sistematiese foute van die instrumente was ondersoek. Die resultate vir die finale metings het gewys dat die TG resultate binne 'n aanvaarbare gebied van beide die FG, gemeet op die VNA en simulasie resultate soos voorspel deur CST. Die studie het gewys dat CST gebruik kan word om komplekse strukture te kan simuleer wat betroubare resultate lewer in gevalle waar 'n akkurate meting nie altyd gewaarborg kan word nie.

Table of contents

Chapter 1 : Introduction	1
1.1. Thesis structure and scope	1
Chapter 2 : Current and material property probes	3
2.1. Introduction	3
2.2. Current-probe calibration	3
2.2.1. Specially constructed jigs for current probe calibration	4
2.2.2. Calibration through mathematical compensation	7
2.2.3. Modelling of current probes.....	9
2.2.4. Comparison to method implemented in Chapter 4.....	10
2.2.5. Conclusion for the current probe calibration techniques	11
2.3. Material property measurement with SMA probe	11
2.4. Investigation of the CM current on the material property probes.....	12
2.4.1. Proposed investigation	13
2.5. Conclusion	15
2.6. References for Chapter 2.....	15
Chapter 3 : CST modelling and data processing	16
3.1. Introduction	16
3.2. Modelling probe-related problems in CST.....	16
3.2.1. Model for the EMCO probe enclosure.....	16
3.2.2. Model for the SMA material probe.....	17
3.2.3. E-Field probe.....	19
3.3. CST data processing.....	20
3.3.1. Data processing for current probe.....	20
3.3.1.1. Method 1 - Using data files and MATLAB.....	21
3.3.1.2. Method 2 - Using CST post-processing	23
3.3.1.3. Difference between Method 1 and 2	24
3.3.2. Data processing for SMA material probe with field probe.....	25
3.4. Conclusion	27
3.5. References for Chapter 3.....	28

Chapter 4 : Current probe calibration for common mode current investigation29

- 4.1. Introduction 29
- 4.2. Current probe calibration..... 30
 - 4.2.1. Background30
 - 4.2.2. Theoretical modelling32
 - 4.2.3. Calculations and Smith Chart.....34
- 4.3. CST Final modelling for the large EPE..... 36
- 4.4. Experimental setup and measurement procedure 37
 - 4.4.1. Spectrum Analyser measurement setup and procedure for the large EPE without using a VNA38
 - 4.4.2. Vector Network Analyser setup and measurement procedure for the large EPE40
- 4.5. Results and experiment refinement 42
 - 4.5.1. Final Spectrum Analyser based measurement.....42
 - 4.5.2. Final Vector Network Analyser measurement45
- 4.6. Conclusion for the probe calibration..... 45
- 4.7. References for Chapter 4..... 47

Chapter 5 : Sampling oscilloscope setup and time-base correction48

- 5.1. Introduction 48
- 5.2. Sampling oscilloscope..... 48
 - 5.2.1. How sampling oscilloscopes work.....49
 - 5.2.1.1. Classic sequential equivalent-time sampling method..... 49
 - 5.2.1.2. Modern method used in scopes such as the Agilent 54750A 50
- 5.3. Time-base correction from NIST 51
 - 5.3.1. The TBC method51
- 5.4. Measurement setup and components 51
 - 5.4.1. Impulse generator52
 - 5.4.2. Signal sources.....56
 - 5.4.3. Final Setup56
 - 5.4.4. Example using the impulse generator57
 - 5.4.5. Results from TBC (To TBC or Not to TBC !?)59
- 5.5. Conclusion 60

5.6. References for Chapter 5.....	61
Chapter 6 : Material and Field Probes: modelling and measurements	62
6.1. Introduction	62
6.2. Modelling.....	63
6.2.1. Mprobe	63
6.2.2. Shield and the Field Probe	64
6.2.3. Final model.....	65
6.3. Experimental setup and measurements.....	68
6.3.1. Frequency-domain measurements using the VNA.....	68
6.3.1.1. Frequency-domain setup for the VNA.....	70
6.3.1.2. Frequency-domain measurements	70
6.3.1.3. Results for the VNA measurements for the final field probe	72
6.3.2. Time-domain measurements on the Agilent Sampling oscilloscope	73
6.3.2.1. Time-domain setup on the Agilent sampling oscilloscope.....	74
6.3.2.2. Measurements	75
6.3.2.3. Results.....	76
6.4. Conclusion	79
6.5. References for Chapter 6.....	81
Chapter 7 : Final conclusion and future recommendations	82
7.1. Summary of the study	82
7.2. Future recommendations	83
Appendix A : Matlab functions for Current probe Calibration.....	I
Appendix B : Smith Chart method	VII
Appendix C : Probe calibration from Chapter 4.....	IX
Appendix D : Matlab code for the TBC data from Chapter 5.....	XIII
Appendix E : TBC corrected Impulse with SRD.....	XXII
Appendix F : Results for the parameter sweep from section 6.2.2	XXIII
Appendix G : Frequency-domain results for Chapter 6	XXV
Appendix H : Time-domain results for Chapter 6	XXVIII
Appendix I : Final results for the sampling scope compared to the VNA....	XXXIII

List of Figures

- Figure 1-1: Difference between common mode and differential mode current 1

- Figure 2-1: An illustration of the measuring jig described by Pommerenke et al. [2].....4
- Figure 2-2: A close up view of how the gap is “closed”, (after fig. 4 in [2])5
- Figure 2-3: Circuit diagram (after Fig.8 in [2])5
- Figure 2-4: Test fixture used by Ruddle [3]. The fixture was open at the sides7
- Figure 2-5: The model used in [3],showing the four junctions and three regions used (at the top of the diagram). Q(f), P(f) and R(f) are the scattering matrices which are formed by this configuration8
- Figure 2-6: An illustration of the initial proposed setup for the measurement of the CM current on the outside of the SMA probe’s cable using the clamp-on CP..... 14
- Figure 2-7: An illustration of the setup for the measurement of the electric field around the SMA probe’s cable 14

- Figure 3-1: CST model of the EMCO probe enclosure 17
- Figure 3-2: The model for the Mprobe and its connector 18
- Figure 3-3: The Mprobe with shield, showing the parameters that determine the dimensions of the shield 19
- Figure 3-4: Cross-section of the E-field probe used to probe the electric field in the shield region 19
- Figure 3-5: A model of the material block placed at the face of the Mprobe (a.) Shows the material block when air was used for an open measurement (b.) Shows a block of Teflon (lossy) used for a material measurement.....20
- Figure 3-6: Results from CST's H-Field monitors. The the magnetic field lines are shown for the current flowing on the conductor at a specific position on the z-direction.....22
- Figure 3-7: A sample from a surface current data file exported from CST22
- Figure 3-8: Diagram of the EPE showing the curves used for the integration of the H-field24

Figure 3-9: A graph showing the difference between the calculated data from both methods and the data provided by the manufacturer. Here the manufacturer's data is the reference value for the transfer impedance of the current probe, the frequency values reported in Table 4-8	26
Figure 3-10: The default Gaussian impulse for CST. This pulse has a bandwidth of 3 GHz	26
Figure 3-11: The output seen at the port of the field probe	27
Figure 3-12: The positions of the field probe (a.) and the corresponding field strengths (b.) for the E-Field monitor at 1 GHz. The results at this frequency were used to pick the location of these measuring points.....	28
Figure 4-1: A common experimental setup illustrating differential mode and common mode currents occurring in the laboratory.....	29
Figure 4-2: A version of the CISPR 16 [1] calibration enclosure, designed by Christo Nicholls (MScEng, 2007).....	30
Figure 4-3: EMCO Probe Enclosure (EPE).....	32
Figure 4-4: A circuit diagram of a signal generator with a known load.....	35
Figure 4-5: CST model created for the large EPE	37
Figure 4-6: Experimental setup for the spectrum analyser measurements.....	38
Figure 4-7: A flow diagram showing the method used for the spectrum analyser.....	39
Figure 4-8: A flow diagram of the SA method when the measurement was automated through the GPIB interface.	40
Figure 4-9: Setup for the network analyser, port three is terminated in a matched load.....	41
Figure 4-10: A final setup for the large EPE used for the spectrum analyser method	42
Figure 4-11: Transfer impedance of the large EPE determined using the spectrum analyser method	43
Figure 4-12: Transfer impedance of the small EPE determined using the spectrum analyser method	43

Figure 4-13: Transfer impedance of the large EPE calculated using the network analyser method.....	44
Figure 4-14: Transfer impedance of the small EPE calculated using the network analyser method.....	44
Figure 4-15: The final results for the transfer impedance. This graph compares the results for both EPEs, measured on the SA and VNA.....	46
Figure 5-1: Real-time sampling with the reconstructed signal	48
Figure 5-2: Sequential equivalent-time sampling showing the reconstructed signal.....	49
Figure 5-3: Diagram illustrating the basic principle behind a sampling oscilloscope in the classical sequential method	50
Figure 5-4: A typical circuit for high-power impulses (after Fig 1c in [3]).....	53
Figure 5-5: The built IGen used in this study. Here the coaxial cable is replaced by a 50 Ω microstrip line with connecting strips for extra length.....	54
Figure 5-6: Circuit diagram of impulse generator with a SRD output and a normal output	54
Figure 5-7: A time-domain representation of both impulses that the IGen can produce	55
Figure 5-8: The spectra of the two impulses generated by the IGen	55
Figure 5-9: The final setup for the TBC measurement and the template for the final measurement with the material-probe.....	57
Figure 5-10: A graph showing the original waveform (dashed), the 100 th waveform and the averaged waveform (solid line)	58
Figure 5-11: The solid line represents the scope-averaged waveform, while the dot-dash line represents the TBC corrected and averaged waveform.....	58
Figure 5-12: Spectrum of the TBC and oscilloscope averaged impulse with no SRD at the output.....	59
Figure 5-13: Spectrum of the TBC and oscilloscope averaged impulse with a SRD at the output.....	60

Figure 6-1: The Mprobe with connector and cable as modelled in CST	63
Figure 6-2: A schematic diagram of the relation of the components and the variables listed in Table 6-1	64
Figure 6-3: The shield structure with the variable relations needed for the CST model.....	65
Figure 6-4: The CST model for the Fprobe as well as the variables used for this model.....	66
Figure 6-5: The E-Field lines inside the shield at 1 GHz.....	66
Figure 6-6: The final CST model for the Mprobe, shield and Fprobe. In this figure the Fprobe is at position 4 (P4) where ProbeH = 125 mm.....	67
Figure 6-7: The physical constructed Mprobe with shield structure. The four measuring positions are clearly visible. The Fprobe is at position P4.....	67
Figure 6-8: The noise floor for a standard and a low noise calibration. This measurement was carried out on the Agilent 8753 VNA using the VNA setup in Table 6-4 measurement # 1.....	70
Figure 6-9: Setup for the experiment using the VNA	71
Figure 6-10: The physical setup for the two VNAs used a. Agilent 8510 and b. Agilent 8753. In both setups the same highly phase stable cables from Suhner were used	71
Figure 6-11: Measured S_{21} for the Fprobe using the VNA when the Fprobe is placed at P4. The measurement also illustrates the noise floor when the measurement was made.....	73
Figure 6-12: Setup used for the experiment using the sampling oscilloscope	74
Figure 6-13: The physical setup of the TD measurement, this shows all the components used.....	75
Figure 6-14: The setup configuration where the standards for the reference impulse were measured, a. shows the connected open standard and b. shows the delay cables used to prevent the measurement of unwanted reflected pulses.....	76
Figure 6-15: The Fprobe was placed at P4 for the measurement discussed in this section	77
Figure 6-16: The normalised output for both the measured and simulated results when the Fprobe is placed at P4.....	77

Figure 6-17: The spectra of the Fprobe output and the output of the CST simulation. The time signal was not normalised in this case. From the magnitude plots, the difference in amplitude between the time signals can be seen.....	78
Figure 6-18: The computed S_{21} compared to the measured S_{21} from the VNA when the Fprobe was placed at P4	79
Figure 6-19: The comparison of the measured and calculated S_{21} against the CST simulated results	80
Figure 6-20: Systematic errors in measurements associated with the cabling of a device under test	80
Figure A 1: A smith chart showing the procedure for calculating the standing wave pattern of the voltage and current	VII
Figure A 2: CST model of the smaller EPE.....	X
Figure A 3: The transfer impedance of the large EPE when the form factor correction is left out, compared against Figure A 4 the difference is visible	XII
Figure A 4: The same results shown in Figure 4-12 compared against Figure A 3 the effect of form factor correction is noticeable.....	XII
Figure A 5: A graph showing the original waveform (dashed), the 100 th waveform and the averaged waveform (solid line), for this impulse a SRD was added to the output of the IGen.....	XXII
Figure A 6: The solid line represents the scope averaged waveform, while the dot dash line represents the TBC corrected and averaged waveform. From this graph the phase difference between the two sets of data is not as clearly seen as in Figure 5-11	XXII
Figure A 7: Magnitude difference for the values of D_S shown in the legend.....	XXIII
Figure A 8: Phase difference for the values of D_S shown in the legend	XXIII
Figure A 9: Magnitude difference for the values of S shown in the legend.....	XXIV
Figure A 10: Phase difference for the values of S shown in the legend	XXIV
Figure A 11: The S_{21} measured for the Fprobe when the length of the probe is cut back from 20mm to 5 mm which were used for the measurements of on the 8510.....	XXV

Figure A 12: CST simulated data compared to the 8510 measurement while the Fprobe is at P4	XXV
Figure A 13: The measured S_{21} for the Fprobe using the VNA when the Fprobe is at P1	XXVI
Figure A 14: The measured S_{21} for the Fprobe using the VNA when the Fprobe is at P2	XXVI
Figure A 15: The measured S_{21} for the Fprobe using the VNA when the Fprobe is at P3	XXVII
Figure A 16: Time signal measured on the sampling scope for the Fprobe at P1	XXVIII
Figure A 17: Spectra for the signal measured at P1	XXVIII
Figure A 18: signal measured on the sampling scope for the Fprobe at P2.....	XXIX
Figure A 19: Spectra for the signal measured at P2	XXIX
Figure A 20: signal measured on the sampling scope for the Fprobe at P3.....	XXX
Figure A 21: Spectra for the signal measured at P3	XXX
Figure A 22: The S_{21} calculated on the sampling scope compared to the measured result from the VNA at P1	XXXI
Figure A 23: The S_{21} calculated on the sampling scope compared to the measured result from the VNA at P2.....	XXXI
Figure A 24: The S_{21} calculated on the sampling scope compared to the measured result from the VNA at P3.....	XXXII
Figure A 25: Compared S_{21} for the calculated, measured and simulated results for the Fprobe at P1.....	XXXIII
Figure A 26: Compared S_{21} for the calculated, measured and simulated results for the Fprobe at P2.....	XXXIII
Figure A 27: Compared S_{21} for the calculated, measured and simulated results for the Fprobe at P3.....	XXXIV

List of tables

Table 4-1: Supplied and calculated transfer impedance. A tolerance of ± 2 dB and ± 0.7 dB for the F-61 and CT-1, respectively, are specified by the manufacturer32

Table 4-2: Dimensions for the EPE seen in Figure 4-3.....33

Table 4-3: Distances for different points along the wire. P1 – P9 are measuring positions and PL is the total distance towards the load33

Table 4-4: The frequencies used for the investigation into the calibration of the 94111-1L current probe33

Table 4-5: Values for the input impedance seen by the source at the input of the EPE with a 50 Ω termination at the end.....34

Table 4-6: The SWP_i determined using the Smith Chart method35

Table 4-7: Variables for the construction of the large EPE's CST Model.....36

Table 4-8: The frequencies (MHz) used for the final calibration experiment of the larger EPE38

Table 4-9: Values (dB_m) for the spectrum analyser method calibration of the large EPE. Chain 1 gives the input power at each frequency and chain 2, the attenuation in the probe path39

Table 5-1: Component values for the impulse generator seen in Figure 5-653

Table 6-1: Dimentions for the final model of the Mprobe, shield enclosure and Fprobe68

Table 6-2: Calibration improvements to decrease the noise floor.....69

Table 6-3: The three individual measurements performed on the VNAs and the objective for each experiment.....71

Table 6-4: The setup of VNA for each measurement72

Table 6-5: The four peaks seen in the measured results with their approximated frequencies72

Table 6-6: The length and time delays of the cables used in the final time-domain measurements74

Table A 1: Form factor from the Large EPE over the measured frequencies IX

Table A 2: Input impedance of the large EPE at each frequency..... IX

Table A 3: Dimensions of the smaller EPE used in the calibration experiments.....	X
Table A 4: The Calibration data for the smaller EPE used in the SA measurements, Chain 1 is the input power and Chain 2 the attenuation in the probe path.....	XI
Table A 5: Input impedance of the small EPE at each frequency	XI
Table A 6: Form factor for the smaller EPE	XI

List of abbreviations

CM	-	Common mode
CP	-	Current probe
D.U.T.	-	Device under test
DM	-	Differential mode
EM	-	Electromagnetic
EMC	-	Electromagnetic compatibility
EPE	-	EMCO probe enclosure
FD	-	Frequency-domain
FDTD	-	Finite difference time domain
Fprobe	-	Field probe
IGen	-	Impulse generator
LPDA	-	Log-periodic dipole array
M.U.T.	-	Material under test
MProbe	-	Material probe
NIST	-	National Institute of Standards and Technology
PEC	-	Perfect electrical conductor
PLL	-	Phase-locked loop
RF	-	Radio frequency
SG	-	Signal generator
SMA	-	Standard military adapter
SWP _I	-	Standing wave pattern of the current
SWP _V	-	Standing wave pattern of the voltage
TBC	-	Time-base Correction
TD	-	Time-domain
TEM	-	Transverse electromagnetic
VNA	-	Vector network analyser

Acknowledgements

The University of Stellenbosch for the use of their facilities as well as financial assistance.

Professor Howard Reader, for being a great mentor and allowing me to benefit from his experience of metrology.

Eskom TESE for the financial backing

My mother Dalene, father Alan and sister Lizelle. Your support during my masters was invaluable

Span C: Sampie Booysen, Braam Otto, Paul van der Merwe, Eric-Jan Moes, Renier Marchand, Elrien Vermaak and Evan Lazer. You made mundane office days very entertaining

J.C. Smit who was always up for a bit of poker and lots of coffee

Martin Siebers, for all the help with the measurement equipment.

Jonathan Hoole and Martin Cavanagh for all the necessary coffee breaks

Lynndal van der Molen for all the moral support and the help with the final touches of the thesis

Chapter 1 : Introduction

In high frequency engineering, accurate measurements are an integral and important part of system design and analysis. Good metrology is normally achieved by calibration and well planned measurements setups. Unwanted common mode (CM) current often disturbs otherwise good measurements. CM current differs from normal differential mode (DM) current and it is valuable to present a clear distinction between the two. Figure 1-1 shows a source that is connected through a cable to some arbitrary device. If a cross-section of the cable is taken anywhere along the length, the DM current will sum to zero.

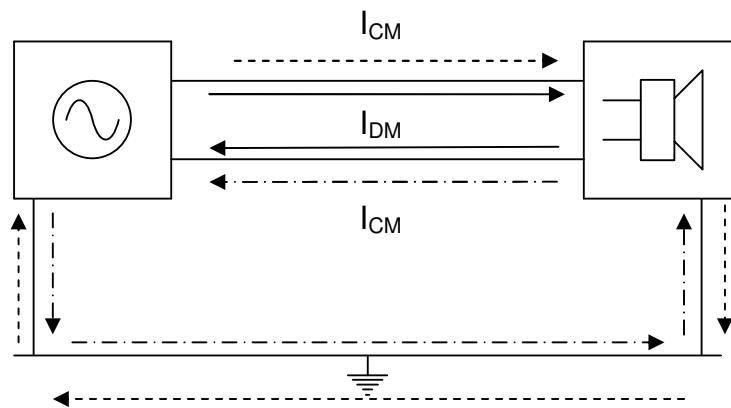


Figure 1-1: Difference between common mode and differential mode current

In this setup both devices share a common ground, which may be the ground wire from the workbench. In Figure 1-1 a possible CM loops is presented. This current paths is not intended current paths and can negatively influence result.

1.1. Thesis structure and scope

This study investigates high frequency probes and CM current issues associated with these probes, focussing on the CM current flowing on the outside of an SMA probe used for material property measurements.

In Chapter 2 various calibration techniques for a clamp-on current probe are discussed. Chapter 2 also sets out the aim of the thesis regarding the CM current flowing on the SMA probe.

Chapter 3 describes the CST modelling for the calibration of the current probe as well as the material probe and its shield-like structure. This chapter also describes the processing procedure for the results from the simulations and experimental measurements.

Chapter 4 details the clamp-on current probe calibration. The calibration demonstrates the environmental effects that need to be considered when working with this class of probe.

Chapter 5 introduces the operation of a sampling oscilloscope and shows this differs from that of its real-time counterparts. The chapter also highlights the systematic time-base errors associated with this measuring device. The NIST (National Institute of Standards and Technology) time-base correction algorithm is demonstrated through an experiment.

Chapter 6 discusses the measurements done for the material probe. These measurements were conducted in the time and frequency-domain. The results for both sets of measurements are compared to the simulations.

Chapter 6 contains the conclusions which can be drawn from this study and outlines recommendations for future study.

Chapter 2 : Current and material property probes

2.1. Introduction

In this chapter, the calibration of a current probe (CP) is discussed. In section 2.2.4, various methods from the literature are compared to the final method implemented in this study (Chapter 4).

Thereafter, the common mode (CM) current on the outside of an open-ended SMA probe will be investigated. This class of probe is used in material property measurements [5]. At the end of the chapter, solution specific issue concerning unwanted CM currents associated with material property probes will be introduced.

2.2. Current-probe calibration

Clamp-on CPs are commonly used in EMC measurements, either as a current monitoring devices or for the injection of disturbances [1]. Various methods of CP calibration are available in the literature. Some procedures, such as those specified in CISPR 16, required special fixtures to be constructed for the calibration of each type of CP. Other methods, such as those outlined in [2] and [3], attempted to create a standard fixture with which a range of CPs could be tested.

Other, more recent work [4] used the simulation software package CST to create a model for the CP, using careful measurements combined with the simulation results. In [4] the CP is used to inject current into systems under investigation. This is referred to as bulk current injector (BCI). The important factor required for this type of calibration is the transfer impedance of the CP. (2.1) references the output voltage of the CP, across a 50 Ω termination, to current flowing on the conductor.

$$Z_T = \frac{V_{probe}}{I_{Conductor}} \quad (2.1)$$

In the sections which follow, these calibration and modelling techniques will be examined. These findings will influence the final choice of calibration, which will be discussed in Chapter 4.

2.2.1. Specially constructed jigs for current probe calibration

In [2], Pommerenke et al. described CP characterisation using a specially constructed jig. In the jig, the conductor is divided into two transmissions lines, A and B, (as seen in Figure 2-1), separated by a sensing resistor, R_{sense} . The entire transmission system is suspended between two metal bulkheads and is connected through the bulkheads with SMA connectors.

Transmission line A (TL-A) was a solid rod, while transmission line B (TL-B) was a semi-rigid cable. As shown in Figure 2-1, R_{sense} formed a gap between TL-A and TL-B where the CP is clamped onto the transmission line. The centre conductor of the semi-rigid cable (TL-B) was connected to the solid rod (TL-A), while the outer conductor of TL-B was connected through a ring of surface mounted (SMT) resistors, which forms R_{sense} . The inner conductor of TL-B gave access to the current flowing on the conductor at the sensing gap.

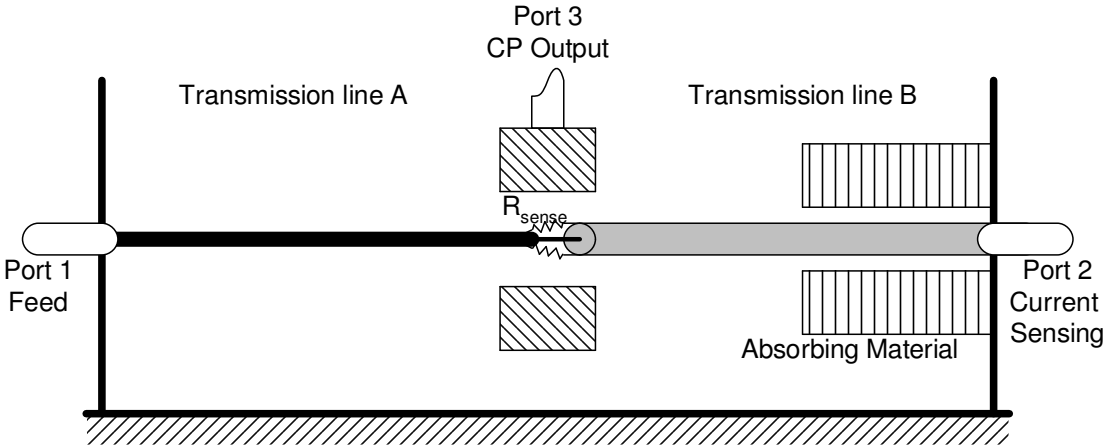


Figure 2-1: An illustration of the measuring jig described by Pommerenke et al. [2]

The sensing resistor R_{sense} consisted of thirty 0805 (80 x 50 mil) SMT resistors. Figure 2-2 shows the basic construction of the sensing resistor. Placing these resistors in a circle around the gap forms a low inductance resistor. If the individual resistors are chosen correctly, the value of R_{sense} can be in the range of 1 - 10 Ω . This makes the voltage measured at port 2 directly proportional to the current flowing inside the gap.

When selecting the correct resistors for R_{sense} , it is vital to ensure that the inductances of the resistors are small. If the inductance becomes a factor, this will introduce a frequency dependency for R_{sense} .

The absorbing material at port 2 (Figure 2-1), did not provide a perfect match and consequently caused reflections. This material was added to reduce the standing-wave ratio of the current (SWR_i). When calibrating a current probe, it is undesirable for the standing wave to go through a null or have a high current gradient at the measuring point.

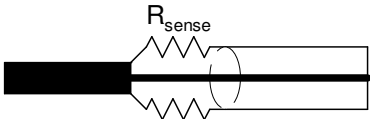


Figure 2-2: A close up view of how the gap is “closed”, (after fig. 4 in [2])

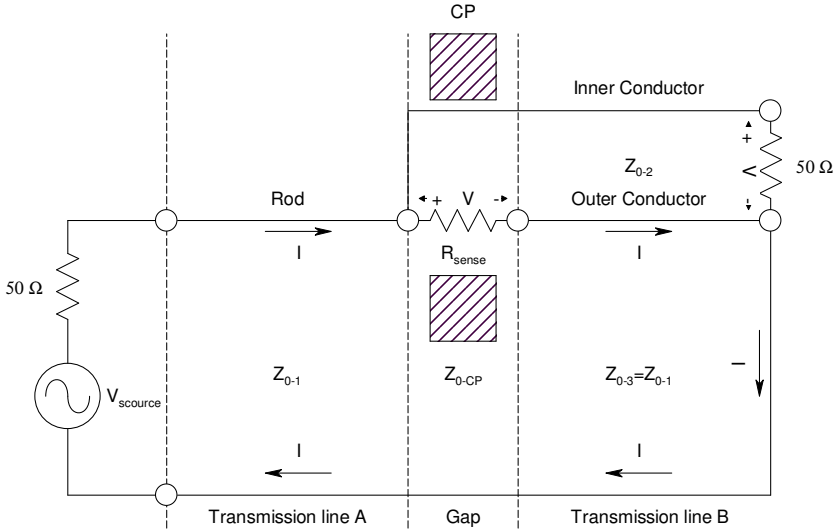


Figure 2-3: Circuit diagram (after Fig.8 in [2])

The circuit diagram in Figure 2-3 illustrates how the circuit is connected, as described in the study by Pommerenke et al. The advantage of this jig above most open wire systems was that no modification was required to the setup – such as removing the CP – to calculate the current flowing on the conductor. An additional advantage was that the characteristic impedances, Z_{0-1} and Z_{0-2} , of the wires over a ground plane did not have an effect on the calibration of the probe. If necessary, Z_{0-1} and Z_{0-2} can be chosen to represent the actual application in which the probe is to be used.

The transfer impedance measurement was made in two steps using a vector network analyser (VNA). The first measurement was made by connecting the feed (port 1) and current (port 2) port and terminating the CP (port 3) in 50 Ω (Figure 2-1),. The S_{21} measurement (S_c) in this configuration gave the current flowing on the wire.

In the second step, the current port was terminated in 50 Ω while the CP was connected to the second port of the network analyser. This S_{21} measurement (S_v) gives voltage at the output of the CP. Using both these measurements, the transfer impedance (Z_T), in dB_Ω , can be determined using:

$$Z_T = S_v - S_c + 20 \log_{10} \left(\frac{R_{sense} \cdot 50}{R_{sense} + 50} \right) \quad (2.2)$$

In [2], Pommerenke et al. proved that the results for Z_T are independent of the test setup's impedance (Z_{0-1} and Z_{0-3} from Figure 2-3) by comparing the results of two measuring jigs. Looking at the results shown in the article, the difference between the two measuring jigs is less than 1 dB, over the frequency range of 0-900 MHz. However, for frequencies greater than 1 GHz, The results varied by as much as 4 dB. According to [2], the CP calibration may be affected by the following secondary factors:

- Proximity of the CP body to the enclosure
- Tilting and off-centre measuring of the CP
- The SWR_i , sharp current gradients and nulls

In summary [2]:

- This method was primarily suitable for CPs used as current monitors
- The geometry of the fixture (height of the conductors) was not a critical parameter in the calibration
- This setup was suitable for a large range of CPs
- This method allowed the complex transfer impedance to be calculated
- This method was an open setup and allowed the secondary factors affecting the calibration to be explored

2.2.2. Calibration through mathematical compensation

In [3], the test fixture, seen in Figure 2-4, was an open structure where a CP can be connected around the conductor. Ruddle proposed a method where the fixture is divided into three regions, with the CP connected in the centre of the conductor as illustrated in Figure 2-5.

When the first (left) and third (right) regions were chosen to be the same length, the system was symmetrical and only half of the calculations were required. Ruddle used a simple one-dimensional transmission line model based upon this symmetry and assumed lossless junctions.

Ruddle estimated the propagation constant of the fixture $\{\beta(f)\}$ from a measured scattering matrix $J(f)$. $J(f)$ is measured when the fixture is empty. From $J_{21}(f)$ and $\beta(f)$ the complex reflection coefficient $\{\rho_1(f)\}$ at the coaxial port can be calculated.

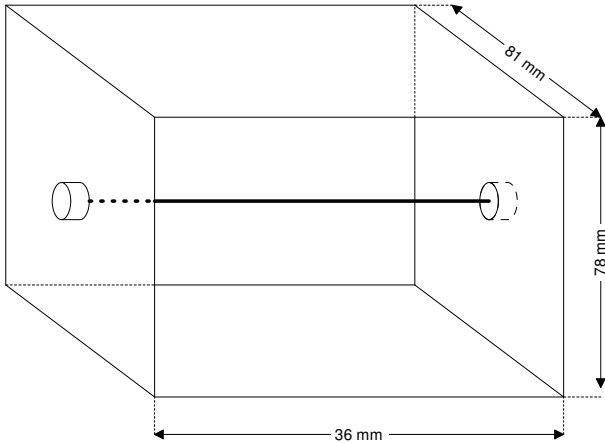


Figure 2-4: Test fixture used by Ruddle [3]. The fixture was open at the sides

Using $\beta(f)$ and $\rho(f)$ along with the input current at the port, the current distribution $\{I(f,z)\}$ could be estimated for any distance along the conductor for the empty fixture. For an oversized fixture, where the CP did not occupy the whole fixture, only the current distribution at the centre of the fixture was important. $Q(f)$ and $R(f)$ represent the scattering matrices for the empty regions (1 and 3) between the ports and the CP.

Ruddle proceeded to measure the complete system with the CP at centre of the fixture and terminated in 50Ω . This gave the scattering matrix $T(f)$. Using these

results, the scattering matrix $P(f)$, for the region occupied by the CP, could be calculated.

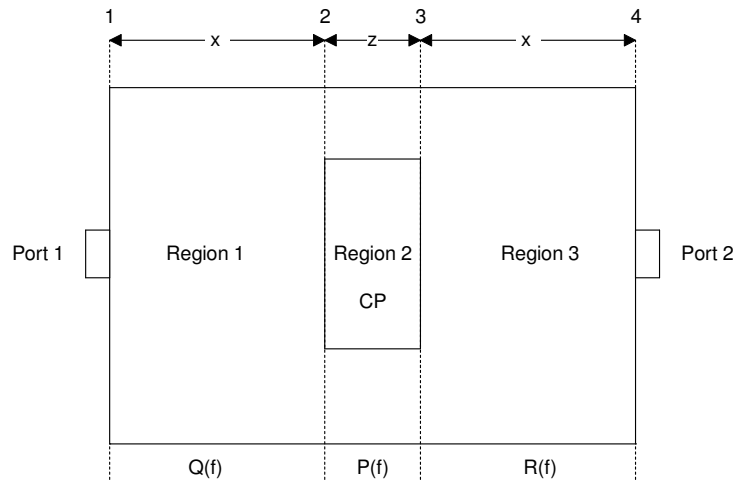


Figure 2-5: The model used in [3], showing the four junctions and three regions used (at the top of the diagram). $Q(f)$, $P(f)$ and $R(f)$ are the scattering matrices which are formed by this configuration

The procedure used by Ruddle characterised the scattering parameters for the CP. For the calibration to calculate Z_T , the results for $P(f)$ must be used to calculate the current distribution with the CP inside the fixture. By measuring from port 1 of the fixture to the output of the CP, and applying the same analysis method for empty fixture, the propagation constant $\gamma(f)$ and reflection coefficient $\rho_2(f)$ for region 2 could be extracted. Using these new results, the voltage relative to the incident voltage V_0 for any position inside region 2 could be calculated $\{V(f)\}$.

The current distribution in this case is derived for the CP inside the fixture. Taking the measured transmission coefficient, $\tau(f)$, from the input of the fixture to the CP output, along with $I(f,z)$ and $V(f,z)$ and Z_0 of the measuring system, an estimated Z_T can be calculated using (2.1):

$$Z_T = Z_0 \frac{\tau(f)V(f, z)}{I(f, z)} \quad (2.3)$$

Different currents were used as reference for estimating the scattering parameters $\{Q(f), P(f) \text{ and } R(f)\}$. From these matrices, a mathematical Z_T was determined. Experimentally measured voltages were then combined with the Z_T values to obtain a value for the current, which could then be compared to a

simulation. It is not clear from the results how successful the procedure is. The Z_T results, for all of the reference currents, had two dips at 433.33 MHz and 550 MHz.

After calibration, Z_T (for all the references) was used to measure the current flowing on a conductor inside an aluminium box. The box had an aperture exposed to a log-periodic dipole array, which causes a current to flow on the centre conductor. Both the ends of the conductor are connected to 50 Ω . A numerical model of the system, excluding the CP, was created using a transmission line matrix (TLM).

The results from the TLM were used to predict the current flowing on the conductor. When Ruddle compared his measured current for all the Z_T s, he discovered that the measured results differed from the predicted current by as much as 5.31 dB (-50.50 dB_A predicted and -45.19 dB_A measured). Ruddle stated that the Z_T results for the current in the centre of the empty fixture as reference delivers the best measured current. According to the paper, this delivers a better estimation for Z_T than using the current at the input of the fixture.

2.2.3. Modelling of current probes

CPs are used in the EMC field not only as measuring devices, but also as devices to inject current onto equipment under test (EUT). These probes have the advantage of being more economical and the current can be injected precisely where it is required. In [4] a FCC F-130A (by Fisher Custom Communications Inc.) was modelled using CST. The model was tuned using the simulation results and careful measurements using a VNA. This probe is well suited for susceptibility testing of spacecraft and automotive systems and is rated up to 400 MHz by FCC.

For the modelling, the metallic body and windings of the probe were taken as perfect electrical conductors (PEC). The magnetic property of the probe's core, unknown to the authors, was modelled using a first order Debye model:

$$\begin{aligned}\hat{\mu}_r(\omega) &= \mu_r'(\omega) - j\mu_r''(\omega) \\ &= \mu_\infty + \frac{\mu_s - \mu_\infty}{1 + j\omega\tau}\end{aligned}\tag{2.4}$$

where: $\mu_s = 375$, $\mu_\infty = \mu_0$ and $\tau = 5e^{-6}$

The reflection coefficients of the probe's input determined the choice of this model. For a correct simulation, the model included the SMA to N-type chain used in the measurement setup.

After completion of the probe model simulation, Di Rienzo et al. used a fixture, (also simulated in CST) with and without the CP's model, to validate their results for the CP. For the validation measurement, the CP was placed in the middle of the fixture. This allowed for symmetry in the measurements and therefore, only half of the measurements were required. (2.5) shows the scattering matrix:

$$S = \begin{pmatrix} S_{11} & S_{21} & S_{13} \\ S_{21} & S_{22} & -S_{13} \\ S_{13} & -S_{13} & S_{33} \end{pmatrix} \quad (2.5)$$

From the results of the simulation and measurements, it was clear that the model and physical structure delivered very similar results. For the individual components, fixture and CP model, the results did not seem to differ by more than 1 dB. For the combined measurement, with the CP in the centre of the fixture, the largest difference between simulation and measurement occurs at higher and lower frequencies.

The greatest difference between the simulated and measured S-parameters was seen for S_{13} and S_{33} , which show a difference of up to 2 dB over the frequency range. This is presumably due to the model used for the magnetic core of the CP.

2.2.4. Comparison to method implemented in Chapter 4

For the CP used in this study, the problem was to calibrate it to a system where the setup is well defined. The intention was to use the CP to measure CM current on the outside of a cable connected to an open-ended SMA probe. Therefore, the standing wave pattern (SWP_i) of the CM current has a maximum on one end and a minimum at the other end of the conductor.

Taking into consideration what was said in [2] about avoiding the high current gradients, a method was proposed whereby the CP is calibrated in an open environment. This was very similar to the fixtures in [2] and [3], but with close attention paid to the SWP_i. In this calibration, the input current was mathematically calculated at a few hand-picked frequencies and a CST model of the fixture created, to obtain the current flowing on the conductor.

From the simulated results, a normalised current form factor (CFF) was created. To obtain the CFF the current flowing on the conductor was normalised to

the current at the input port. This ensured that the voltage measured at the port of the probe changed with the actual measured current and that the transfer impedance was independent of the length of the test fixture.

2.2.5. Conclusion for the current probe calibration techniques

When studying the calibration techniques of CP, many authors tended to compare the results of their calibration to one or more setups employing the same technique. A possible complication in the calibration of a CP, or any measurement probe, is there is no set standard to which the “errors” in the measurement setup may be compared.

It is assumed that most manufacturers use the method proposed in CISPR 16 for calibration of a CP. This method of calibration is regularly criticised in the literature because of the limitation of the test fixture. The CISPR 16 fixture requires a fixture to be built for each CP model. Although most authors stated that this is a valid technique, no one compared their Z_T results to those provided by the manufacturer. For this study, all the results obtained for the calibration were compared to the manufacturer’s results.

The differences of 1 dB seen in the CP calibration discussed in Chapter 4 are similar to those found in [2]. The method used in [2] to measure the current, provided a relative certainty that the current used in the calibration incorporated the effect of the probe.

The resonances seen in the data of [3] at 433.33 and 550 MHz were also experienced in some of the earlier measurements of the CP mentioned in Chapter 4. These resonances are function of the fixture used for the calibration. Ruddle unfortunately uses the Z_T data from the 550 MHz resonance to illustrate his method.

The finding that the input current provides the best reference for Z_T is corroborated by the findings in Chapter 4, where the input current is corrected to represent the current at a specific measuring position.

2.3. Material property measurement with SMA probe

An open-ended, flanged SMA probe was used for material property measurements. These probes have been in use since the 1970s. In [5], Reader et al. described the basic procedure of a material property measurement. They also

described some of the factors to be taken into consideration when choosing the feeding cable used for these measurements.

The probe is calibrated in [5] using open, short and matched load (OSL) standards at the face-plane of the probe. The material under test (M.U.T.) is placed on the probe face, facing upwards, with a 300g weight to prevent lift-off. To demonstrate the method, results for fused silica were calculated using a full-wave inversion method.

From the ϵ' and ϵ'' values, three clear resonant features were visible at 1.12, 2.08 and 2.28 GHz. Although these features were small, they existed in most of the datasets. Initially it was suspected that these phenomena resulted from the directivity error of the load standard

After a methodical investigation, it was discovered that the 1.12 GHz feature was found to be sensitive to the M.U.T. At first, this feature was thought to be energy escaping the face of the probe and M.U.T. A CM CP was placed around the cable, and connected to a hand-held spectrum analyser (SA) to prevent the introduction of new current loops.

When placing the CP on the outside cable of the VNA, it was found that the CM signal was also present. This led to the believe that these features were connected to identifiable CM path lengths in the measurement setup.

2.4. Investigation of the CM current on the material property probes

For this study, a similar setup to [5] was created for an open-ended SMA probe. This SMA probe was not used for material property measurement, however, it recreated similar results to the CM current observed in [5]. This CM current was then characterised using a CP.

Before each measurement, a CST model of the complete setup for the SMA probe was simulated. These simulated results gave a good indication of the expected result when the measurements were performed.

2.4.1. Proposed investigation

Figure 2-6 shows the initial proposed setup for the measurement of the CM current. In this proposed study, a semi-rigid cable would be used for the illustration of the principle of this experimental procedure.

A semi-rigid cable has the advantage of having good transfer impedance ($Z_t \approx 0$), so all currents measured on the outside of the cable can be directly related to the energy escaping from the SMA probe.

The setup shown in Figure 2-6 shows the cable fed through a ground plane. This would force the current distribution, shown in the right side of Figure 2-6, into a null/minimum value at the SMA probe (open-circuited \Leftrightarrow high impedance) and a maximum at the ground plane (short-circuited \Leftrightarrow low impedance). It must be noted that the current distribution shown here is solely for purpose of illustration. The actual current distribution would be directly connected to the wavelength used for excitation. Using the prior knowledge of the current distribution gained from the simulated results, the CP can be placed at hand-picked positions.

After the thorough calibration process described in Chapter 4, it was discovered that the CP did not give the necessary accuracy required for this investigation. Therefore, a second method was proposed where an electric field probe is used for the investigation. Figure 2-7 shows the setup used for this experiment. In this case, the SMA probe is placed in a cylindrical shield like structure and a field probe is used to measure the field strength at different positions through the side of the shield.

This experiment allowed time- (TD) and frequency-domain (FD) measurements to be conducted. TD measurements contained more data, as all the frequencies can be calculated from a single measured result.

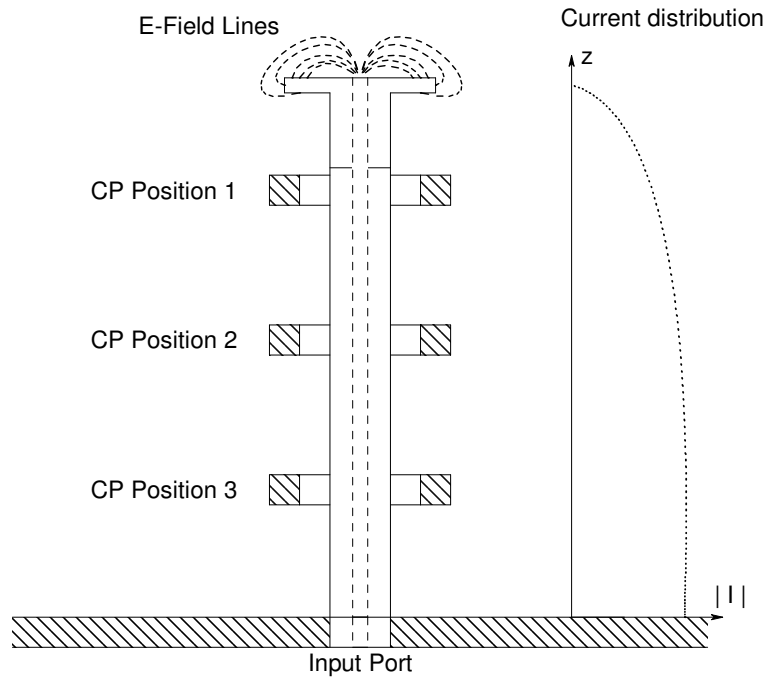


Figure 2-6: An illustration of the initial proposed setup for the measurement of the CM current on the outside of the SMA probe's cable using the clamp-on CP

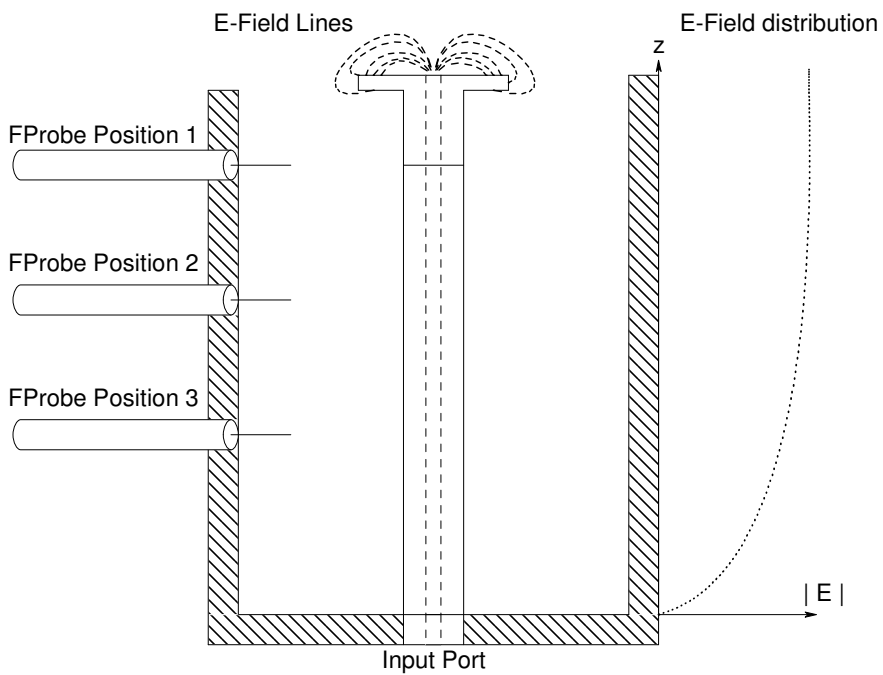


Figure 2-7: An illustration of the setup for the measurement of the electric field around the SMA probe's cable

Measuring in the TD makes reaching a higher signal to noise ratio much easier. In comparison, obtaining a low noise calibration on a VNA makes measurements much longer to conduct. Because the TD solver in CST was used to simulate the model of this setup, simulated TD results are also available.

2.5. Conclusion

From this chapter, the main aim of this study is identified: the investigation of the CM current on the outside of the material property probe. The original intention to use the CP to measure the CM current and the proposed calibration of the CP is outlined in Chapter 4. From this calibration, it was found that the necessary accuracy could not be achieved using the CP, therefore the second method was preferably used (Chapter 6).

2.6. References for Chapter 2

- [1]. G. Cerrie, R. De Loe, V.M. Primiani, S. Pennesi and P. Russo, “*Wide-Band Characterization of Current Probes*”, IEEE Transaction on Electromagnetic Compatibility, volume 45, no 4, November 2003, pp 616-625
- [2]. D. Pommerenke, R. Chundru & S. Chandra, “*A New Test Setup and Method for the Calibration of Current Clamps*”, IEEE Transaction on Electromagnetic Compatibility, volume 47, no 2, May 2005, pp 335-342
- [3]. A.R. Ruddle, “*Calibration of Current Measuring Transducers in Oversized Calibration Fixtures*”, IEEE Transaction on Electromagnetic Compatibility, volume 47, no 1, February 2005, pp 196-201
- [4]. L. Di Rienzo, F. Grassi and S.A. Pignari, “*FIT Modeling of Injection Probes for Bulk Current Injection*”, 23rd Annual Review of Progress in Applied Computational Electromagnetics, March 2007, Italy
- [5]. H.C. Reader and M.D. Janezic, “*Coaxial Probe Dielectric Measurements: Practical Dotting “i’s” and Crossing “t’s”*”, 68th ARFTG Conference, Omni Interlocken Resort, Broomfield, Colorado, December 2006

Chapter 3 : CST modelling and data processing

3.1. Introduction

In this chapter, the modelling of the probes used in the study and their environment will be covered in detail. The modelling of the following probes and measuring jigs will be covered: the EMCO Current probe's enclosure and an SMA material probe with its cylindrical shield. An E-field probe will also be discussed.

This chapter only describes the CST modelling and its functions, but not the results. The results for the current probe will be discussed in Chapter 4 and those for the SMA material probe, in Chapter 6.

3.2. Modelling probe-related problems in CST

3.2.1. Model for the EMCO probe enclosure

The clamp-on current probe was calibrated using a measuring jig referred to as an EMCO probe enclosure (EPE). The EPE was an open wire over a large ground plane as can be seen in Figure 3-1. The wire was connected through the ground shield by SMA female panel mounts. In the modelling of the EPE, the SMA connector was modelled as accurately as possible using detailed measurements [1]. The two ports – one on each side – were fed using both ports available in CST, namely a waveguide and discrete port.

There are significant differences between the two ports. With the waveguide port, CST applies one watt of power over the area of the defined port. On the other hand, a discrete port allows different amplitudes to be specified. (This is especially useful when an antenna array is simulated with an amplitude taper.) Additionally, where the waveguide port is only an S-Parameter port, the discrete port can be defined as either a voltage, current or an S-Parameter port. All three types allow the voltage and current to be monitored. A further advantage of the discrete port over the waveguide port is that the discrete port can be placed inside a structure whereas the waveguide port needs to be placed at the edge of the model.

The following information will be needed from the simulation:

- S-Parameters: The EPE will be used with two calibration procedures, one of which will involve a two-port network analyser.
- Some reference to the simulated current on the conductor: either through the surface current or the magnetic field integrated over a closed path.

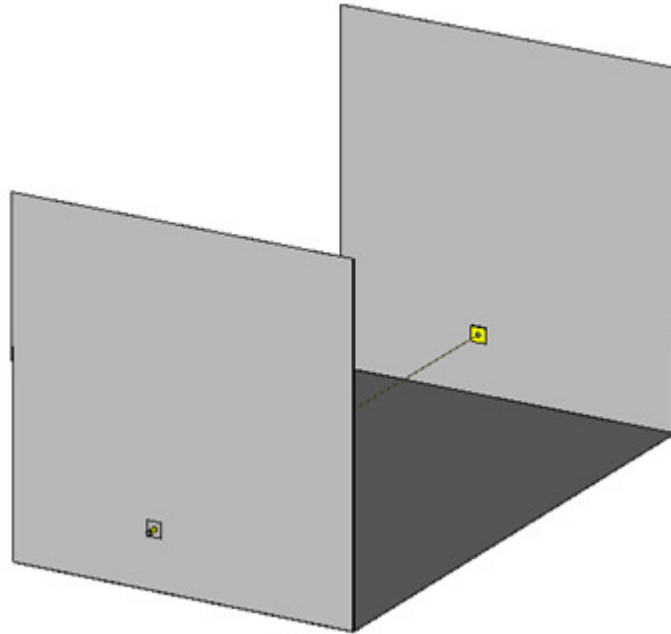


Figure 3-1: CST model of the EMCO probe enclosure

A calibration was carried out over 11 frequencies and 9 positions along the conductor. H-Field monitors were defined for each of the 11 frequencies. These monitors allowed the surface currents to be viewed on the model. These values are then used for later processing.

The model is best created parametrically, as seen in Table 4-7, which allows the model to be quickly reconfigured should a different sized EPE need to be simulated.

3.2.2. Model for the SMA material probe

The SMA material probe (Mprobe) investigated in Chapter 6 consisted of a female SMA panel mount connector, where the centre conductor was cut flush with the face of the connector. The connector was then connected to a highly phase stable cable. Figure 3-2 shows the Mprobe as modelled in CST.

From studies in the literature, e.g. [5] in Chapter 2, a CM current was observed on the outside of the feed cable. Very few studies have included investigations into

the characteristics of this current. It would be intuitive to place the EMCO current probe on the feeding coaxial cable to investigate the currents, but early investigations (described in Chapter 4) showed this to be too invasive a measurement and the necessary accuracy could not be obtained. Therefore the second approach, where a shield structure was added around the cable and Mprobe was implemented. Figure 3-3 shows the CST model for the Mprobe and shield structure. The shield structure was a cylinder, which is blocked off at the feed part. An E-field probe was placed along and inside the shield shown in Figure 3-4. The length of the centre conductor can be varied for simulation purposes and the choice of the final length is explained in Chapter 6.

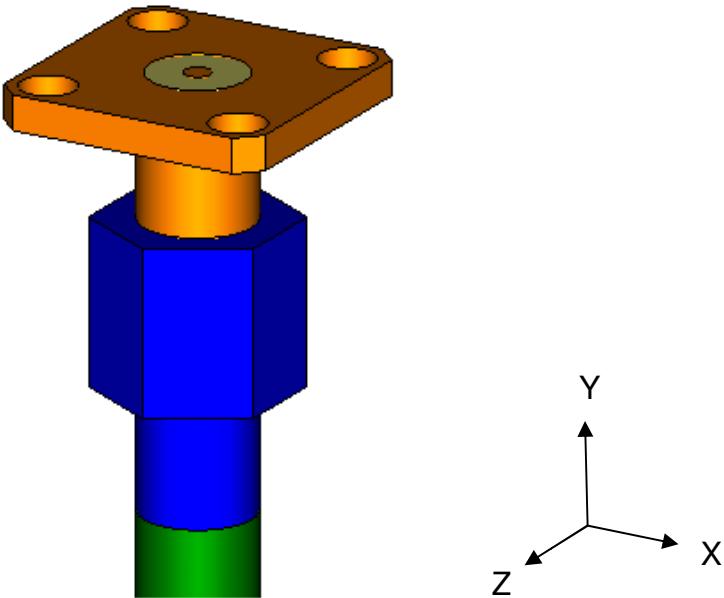


Figure 3-2: The model for the Mprobe and its connector

The variables, S, Ds, T and U (Figure 3-3), which define the dimensions of the shield (also see Table 6-1.), were included in the CST model of the Mprobe. In Chapter 6, the effect of the shield dimensions on the results is investigated in detail. This RF choke was added to observe the impact on the current, which may be induced on the outside of the shield. This current is caused by energy escaping from the open cavity created by the configuration of the Mprobe within the shield. This current is most apparent when the shield height is level to the face of the Mprobe ($S = 0$), resulting in fringing fields that terminate on the outside of the shield itself.

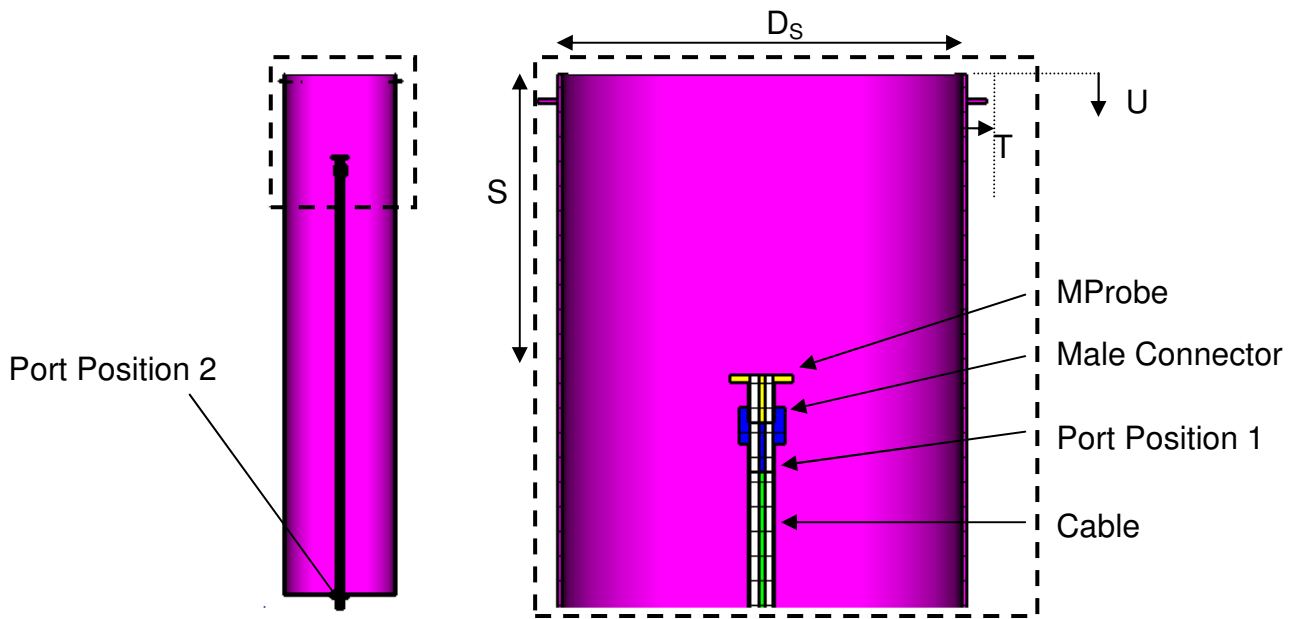


Figure 3-3: The MProbe with shield, showing the parameters that determine the dimensions of the shield

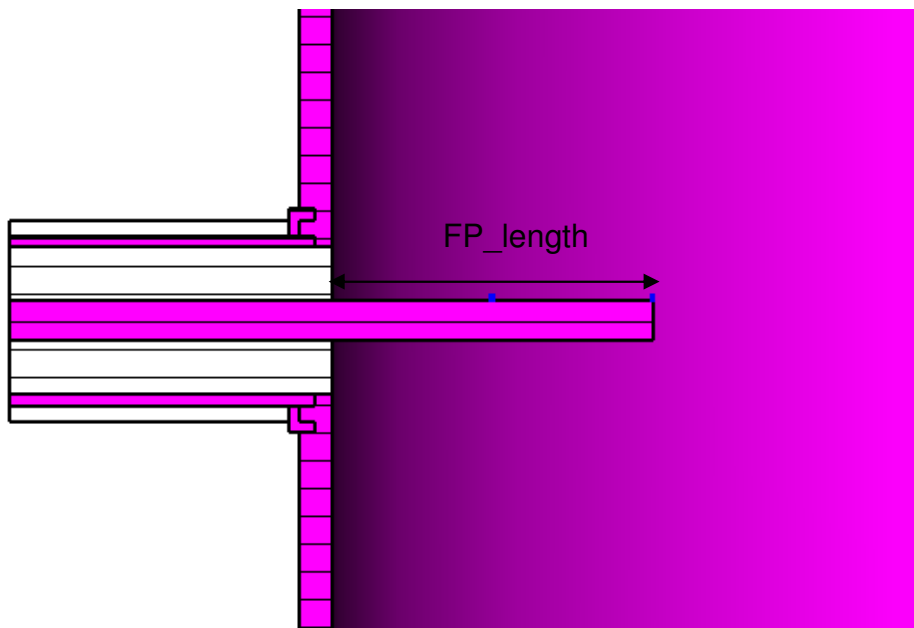


Figure 3-4: Cross-section of the E-field probe used to probe the electric field in the shield region

3.2.3. E-Field probe

The E-field probe is a coaxial cable, which is fed through the sidewall of the shield (Figure 3-4). The probe is an extension of the centre conductor, with the dielectric and outside sleeve cut away. In the simulation and design phase of the model, the length of the probe is variable. In the same way as the physically

constructed model, the probe could be moved along the side of the model to probe the field lines within.

In Figure 3-3 two port positions are shown, port position 1 allowed the simulation time to be reduced considerably for the parameter sweep. In position 1 the cable's dielectric was changed to PEC to form a solid rod structure.

For this model the S-parameters as well as the E-fields for specific frequencies, were monitored from 0 to 3 GHz. The H-field monitors were added for the observation of the magnetic fields and the surface currents. CST also has time-domain monitors, which allowed transients to be observed on the model. The S-parameters were important for the material property determination. The required two S_{11} parameters were an open (air) measurement, Figure 3-5 (a.) and a reflection measurement (S_{11}) of a material slab, seen in Figure 3-5 (b.).

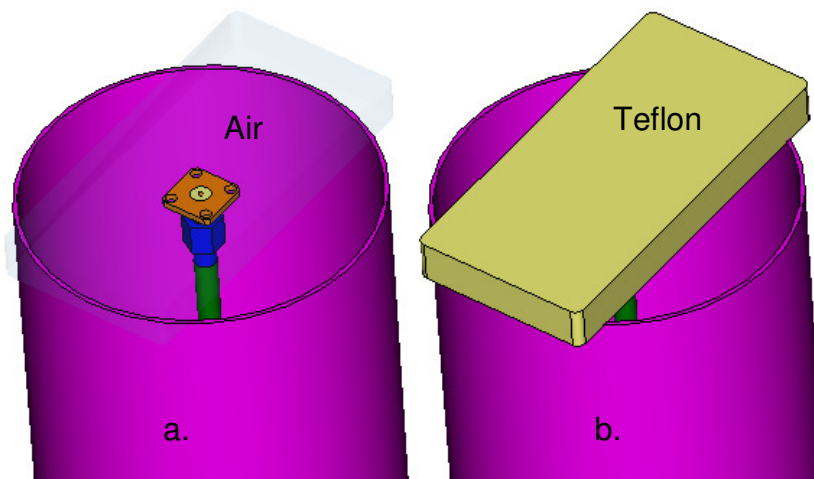


Figure 3-5: A model of the material block placed at the face of the Mprobe (a.) Shows the material block when air was used for an open measurement (b.) Shows a block of Teflon (lossy) used for a material measurement

3.3. CST data processing

3.3.1. Data processing for current probe

The details of the calibration will be covered in Chapter 4. For the current probe calibration, an accurate computation of current flowing on the conductor was required. Two methods to find a current form factor will be described. This was a key aspect of the calibration process. The H-field monitors give access to the magnetic

field and its components (X, Y and Z), seen in Figure 3-6, as well as to the surface current.

From this data, two methods were employed to derive the required information. In method 1, the H-field monitor's surface current data was exported into a data file which was processed with the help of Matlab. In method 2, the data required for the calibration was calculated using CST's built-in features.

3.3.1.1. Method 1 - Using data files and MATLAB

The surface-current data exported from an H-field monitor was contained in a data file (Figure 3-7). This data provided the surface current vector at a coordinate defined by the meshing of the model:

$$K = K_x \overline{u_x} + K_y \overline{u_y} + K_z \overline{u_z} \quad (3-1)$$

Each of the components (K_x , K_y and K_z) consisted of a real and an imaginary part. For the calibration only the magnitude of one specific component was necessary. The conductor was modelled in the z-direction and therefore the current will flow in the z-direction as seen in Figure 3-6.

From CST, the surface current data was exported into a data file that can be used for later post-processing. Figure 3-7 shows the structure in which CST exports the surface current data. The real part of the Z-component is in column 6 and the imaginary, in column 9. On closer inspection, the data file is structured into data blocks. Because a surface current can only be on the model itself, CST filled the data file based upon the defined meshing.

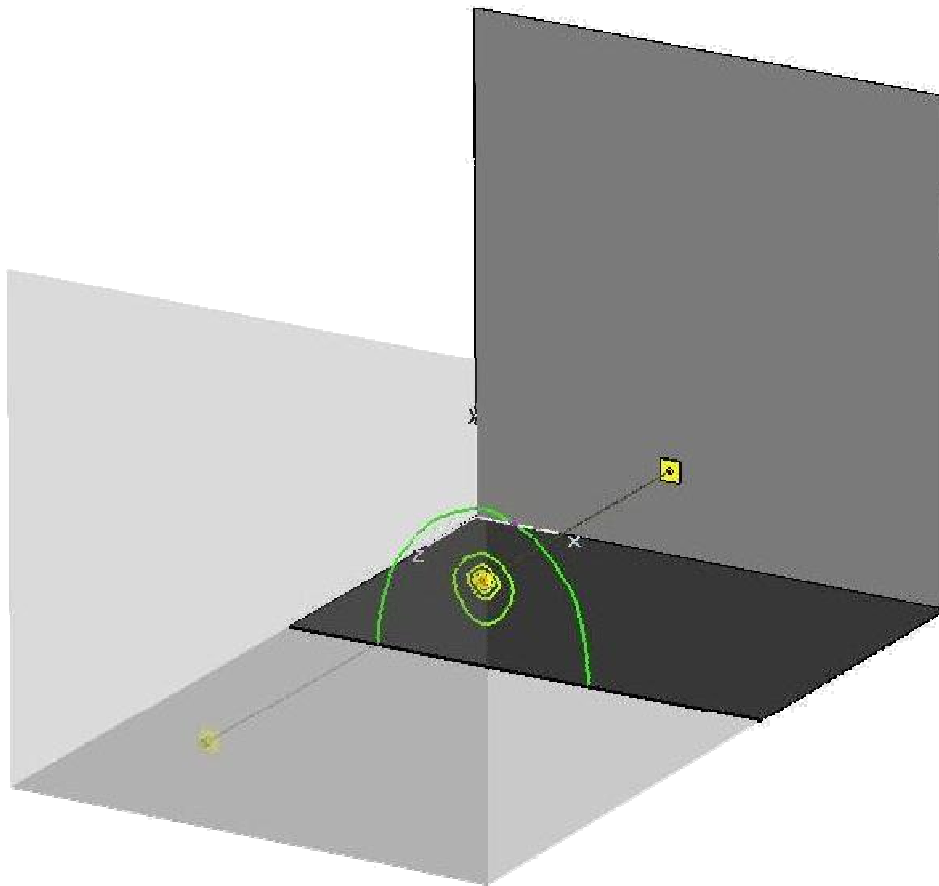


Figure 3-6: Results from CST's H-Field monitors. The the magnetic field lines are shown for the current flowing on the conductor at a specific position on the z-direction

Coordinate columns			Real columns			Imaginary columns			Area [mm ²]
x [mm]	y [mm]	z [mm]	KxRe [A/m]	KyRe [A/m]	KzRe [A/m]	KxIm [A/m]	KyIm [A/m]	KzIm [A/m]	
101.867	60.6833	64.4	-0.174998	0.478103	-8.67772	1.721e-005	-4.70186e-005	4.08022	4.93439
101.525	61.2751	61.3	-0.186524	0.223111	-7.28202	-0.00496202	0.00593333	4.31528	4.93438
101.275	61.5252	64.4	0.275442	-0.730274	-6.61552	-0.000433606	-0.0003625	5.47448	4.93438
100.683	61.8669	61.3	1.30542	-0.477818	-7.32685	-0.00418129	0.00153046	7.64136	4.93439
100.342	61.9585	64.4	0.83237	-0.145213	-9.13058	-0.0019164	0.00033433	7.76786	4.93439
99.3167	61.8669	64.4	-1.31136	-0.480063	-7.31472	-0.000844095	-0.00030896	3.60557	4.93439
98.4748	61.2751	64.4	0.185904	0.222369	-7.26773	-0.000751173	-0.000898517	5.44191	4.93438
98.0415	60.3417	64.4	0.0249452	0.142987	-9.53818	-0.000223922	-0.00128354	7.3693	4.93439
98.1331	59.3167	64.4	-0.173855	0.474979	-8.66982	-0.00077454	0.00211608	4.04638	4.93439
98.7249	58.4748	64.4	0.2769	-0.231492	-6.62139	-0.00134297	0.00112274	5.50852	4.93438
99.6583	58.0415	64.4	0.827837	-0.144422	-9.12479	-0.000204432	3.56647e-005	7.72512	4.93439
100.683	58.1331	64.4	-1.29765	-0.474974	-7.30745	-0.00334158	-0.0012231	3.5563	4.93439
101.525	58.7249	64.4	0.19919	0.238261	-7.27279	-0.00198221	-0.00237102	5.47512	4.93438
101.958	59.6583	64.4	0.0252875	0.144949	-9.54684	8.11311e-006	4.65048e-005	7.42376	4.93439
101.958	60.3417	61.3	-0.0228662	0.13107	-9.57032	-0.00280641	0.0160865	5.61537	4.93439
101.867	59.3167	61.3	-0.170183	0.464949	-8.7044	0.00542707	0.014827	7.17246	4.93438
101.275	58.4748	61.3	-0.274686	-0.229641	-6.64092	0.0106731	0.00892383	4.3085	4.93439
100.342	58.0415	61.3	-0.826504	-0.14419	-9.15624	0.00573372	0.00100029	5.26223	4.93439
99.3167	58.1331	61.3	1.2998	-0.475759	-7.33336	-0.0064209	0.00235021	7.64467	4.93439
98.4748	58.7249	61.3	-0.186754	0.223387	-7.29619	-0.00589715	0.00705389	4.35724	4.93438
98.0415	59.6583	61.3	-0.0226932	0.130079	-9.56331	-0.00254833	0.0146073	5.61663	4.93439
98.1331	60.6833	61.3	0.168323	0.459866	-8.68879	0.00621015	0.0169665	7.09793	4.93439
98.7249	61.5252	61.3	-0.290668	-0.243003	-6.63054	-0.0011742	0.00981649	4.29572	4.93438
99.6583	61.9585	61.3	-0.830073	-0.144813	-9.14663	0.00422294	0.000736725	5.2917	4.93439
102.231	59.1833	64.9333	9.03758e-009	2.46911e-008	-1.75952e-008	1.2517e-007	3.41972e-007	-2.13122e-007	4.88261
101.823	58.4761	62.3667	-0.354574	-0.424124	-0.436132	3.22523e-006	4.45656e-006	-0.245023	4.88264
101.524	58.1772	64.9333	-0.508861	-0.425432	1.6875	3.98346e-007	3.33023e-007	-1.84343	4.88264
100.817	57.7688	62.3667	9.7359e-007	3.56359e-007	2.83135e-007	6.74177e-007	2.46766e-007	5.17848e-006	4.88262
100.408	57.6594	64.9333	6.04706e-008	1.05496e-008	1.39132e-008	1.5461e-007	2.69728e-008	5.43219e-007	4.88262
99.1833	57.7688	64.9333	2.63179e-008	-9.63301e-009	2.32697e-009	-2.44695e-007	8.95644e-008	4.42988e-007	4.88262
98.1772	59.4761	64.9333	-0.356802	0.426789	-0.483112	-2.52553e-007	3.02092e-007	-1.78437	4.88262
97.6594	59.5917	64.9333	-1.47291e-009	8.44277e-009	2.20594e-008	-3.7838e-008	2.16889e-007	-9.47132e-008	4.88262
97.7688	60.8167	64.9333	7.46587e-009	2.03971e-008	2.10237e-008	1.27392e-007	3.4804e-007	2.13518e-007	4.88261
98.4761	61.8228	64.9333	-0.508996	-0.425528	1.68743	3.94221e-007	3.29575e-007	-1.84366	4.88264
99.5917	62.3406	64.9333	-4.13728e-008	-7.2178e-009	-1.91695e-008	1.72077e-007	3.00201e-008	-5.40544e-007	4.88262
100.987	62.3406	64.9333	-1.34679e-008	-4.92954e-009	-2.65995e-009	2.37866e-007	6.70431e-006	-4.36707e-007	4.88262
101.823	61.5239	64.9333	-0.354601	0.424157	0.484709	-2.50644e-007	2.99809e-007	-1.77604	4.88264
102.341	60.4083	64.9333	1.05666e-009	-6.05685e-009	-1.79591e-008	-3.64237e-008	2.08783e-007	9.54538e-008	4.88261
102.341	59.5917	62.3667	6.51799e-008	3.73615e-007	-1.28945e-007	-2.82563e-007	-1.61966e-006	-1.2462e-006	4.88261
97.7688	59.1833	62.3667	-1.42795e-007	3.90123e-007	1.91608e-007	1.4489e-007	-3.95846e-007	-4.57983e-006	4.88261
98.4761	58.1772	62.3667	0.308816	-0.423377	-1.69211	-3.67349e-006	3.07109e-006	-0.308422	4.88264

Figure 3-7: A sample from a surface current data file exported from CST

These data blocks were not predictable and depended on the model's meshing. Consequently, a Matlab function, seen in Appendix A, was created to extract the data from the exported CST surface current files. For this function, the position and length of the conductor needed to be specified as well as a tolerance, which was dependant on how finely the model is meshed.

This function then returns the surface current data along the conductor. From this data the CFF could be calculated, which was then used for the calibration of the CP as described in Chapter 4.

3.3.1.2. Method 2 - Using CST post-processing

In this method, the post-processing of CST was used, as the H-field monitors already provided the magnetic field at each of the frequencies. Ampere's law (3-2) was used to calculate the current. The curves (P1- P9 and the port curve) used for the integration are as shown in Figure 3-8.

$$i = \oint \overline{H}_\phi ds \quad (3-2)$$

$$i = 2\pi r_c H_\phi \quad (3-3)$$

From (3-3) the current was calculated for each of the points along the conductor. Using the port curve as the source current, the normalised current form factor was calculated. Examining the field lines of the magnetic field in Figure 3-6, it is clear that the field lines become less circular, and start to distort as the value of r_c increases. This made the integration of the fields unnecessarily complicated unless r_c was chosen as close as possible to the conductor as the mesh definition will allow.

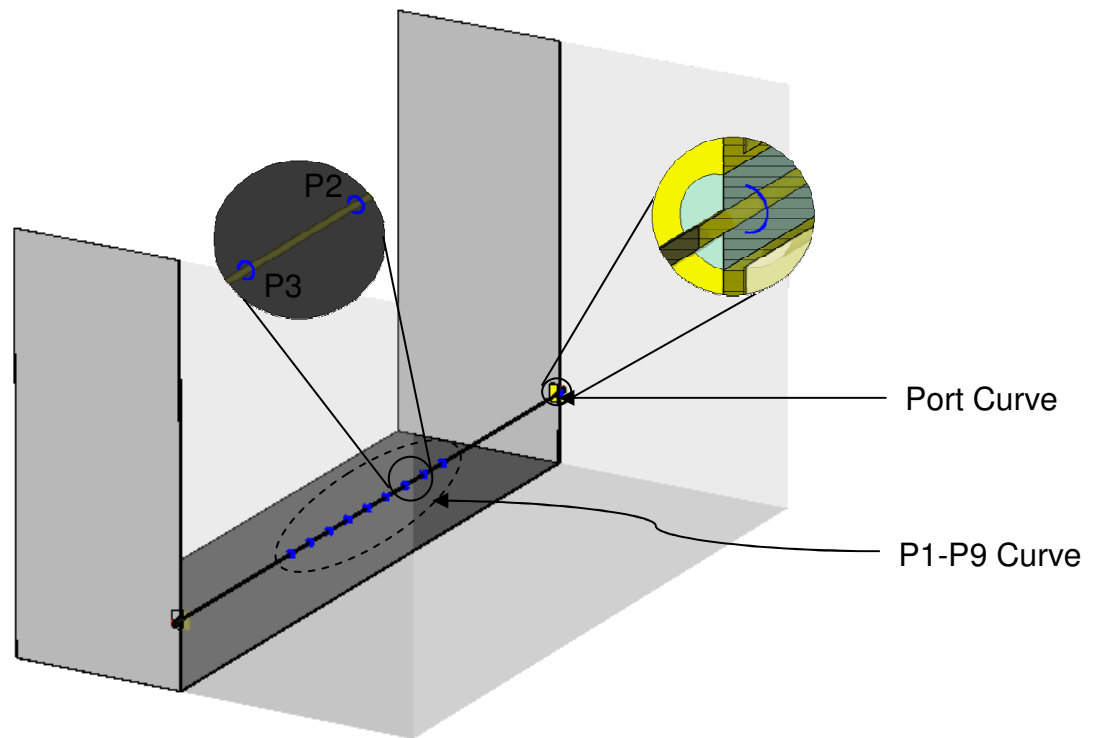


Figure 3-8: Diagram of the EPE showing the curves used for the integration of the H-field

3.3.1.3. Difference between Method 1 and 2

The differences between the two methods employed to obtain the form factor (used in Chapter 4), can be summarised in the following two points.

1. Input current

Method 1: The input current was only available if the meshing around the port was fine enough. CST calculated the surface current at the port. If the mesh was coarse, the input current had to be interpolated. Because the current formed a standing wave inside the EPE, a simple curve-fitting algorithm was used to calculate the input current.

Method 2: In this method, the input current was available at the port and no interpolation was required.

2. Current at different positions

Method 1: The conductor, in this case, was a straight wire and surface current was unidirectional. Should the model become more complicated, it would be possible to extract the surface current data using MATLAB. However, with just an educational licence available, only a limited number of mesh cells could be simulated, and the necessary resolution could not be achieved.

Method 2: Placing curves at the required positions made it easy for the current to be viewed on complicated models. Care should be taken with the path of integration. CST does allow complicated paths of integration to be defined.

The transfer impedance (Z_T) was calculated using equation (2.1) (from section 2.2), but corrected the current with the form factor:

$$Z_T = \frac{V_{probe}}{CFF \times I_{conductor}} \quad (3.4)$$

The methods described above, give two possible methods to calculate this form factor from the simulated data. Figure 3-9 shows the difference between the calculated Z_T , using the form factor from method 1 and 2, and the Z_T provided by the manufacturer. For this argument, the manufacturer's data was taken as the reference Z_T .

Looking at Figure 3-9 it is clear that both methods deliver similar results with almost the same level of accuracy. The large deviation (frequencies 1,2 and 3) between the calculated results and the provided transfer impedance is described in detail in Chapter 4

3.3.2. Data processing for SMA material probe with field probe

For the material probe, both time-(TD) and frequency-domain (FD) measurements were performed. Therefore, the input and output signals from the CST simulations needed to be exported for TD comparison, and the S-parameter S_{21} , exported for the FD. Field monitor results were also exported as the data from these results ultimately led to the final position of the Fprobe.

The TD solver in CST was used with a Gaussian input pulse (Figure 3-10), as the default input signal. This signal was defined by the frequency range over which the simulation was run. For the TD measurements, an impulse generator was used

for excitation of the experiment. Although the generator did not approximate a perfect Gaussian pulse, the simulation results for the output at the Fprobe, seen in Figure 3-11, allowed for the output of the generator to be predicted.

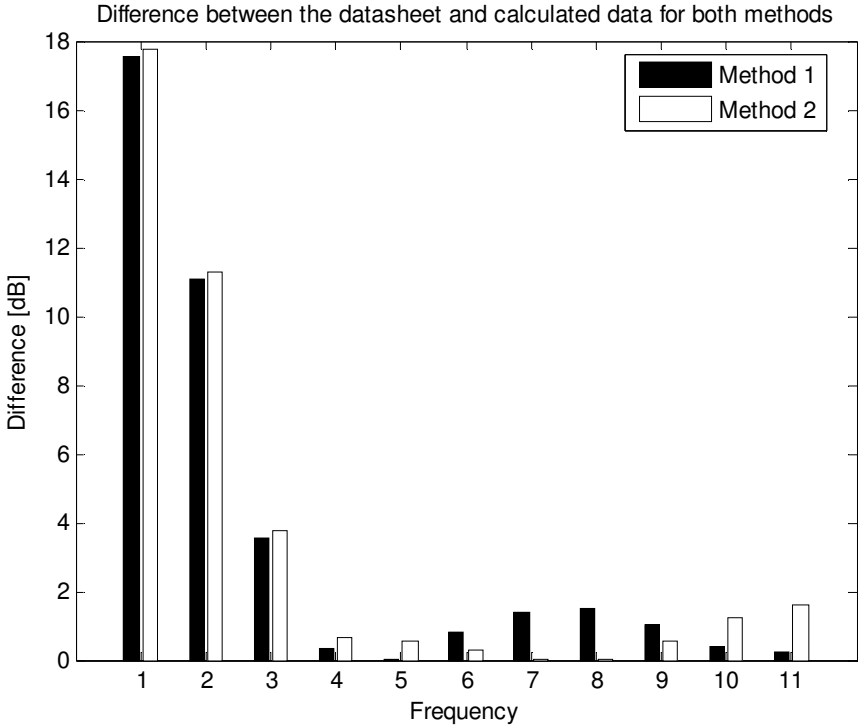


Figure 3-9: A graph showing the difference between the calculated data from both methods and the data provided by the manufacturer. Here the manufacturer’s data is the reference value for the transfer impedance of the current probe, the frequency values reported in Table 4-8

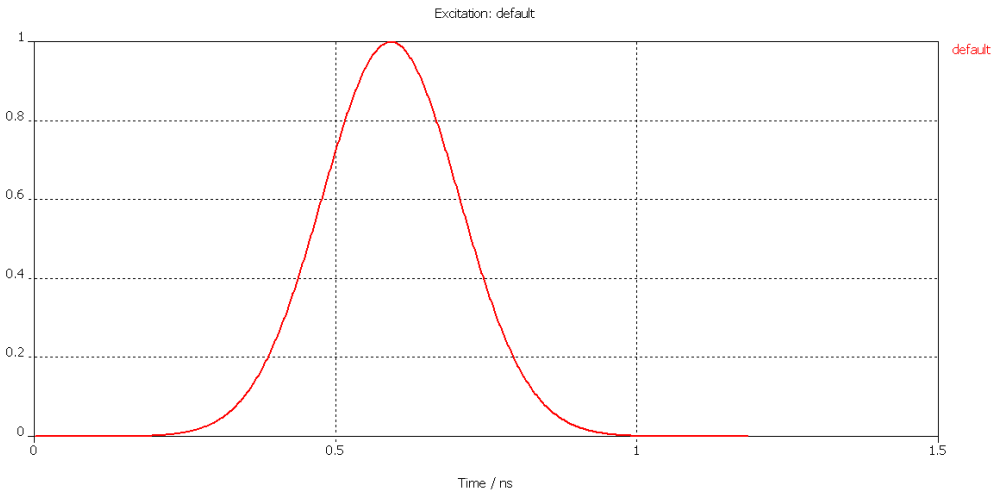


Figure 3-10: The default Gaussian impulse for CST. This pulse has a bandwidth of 3 GHz

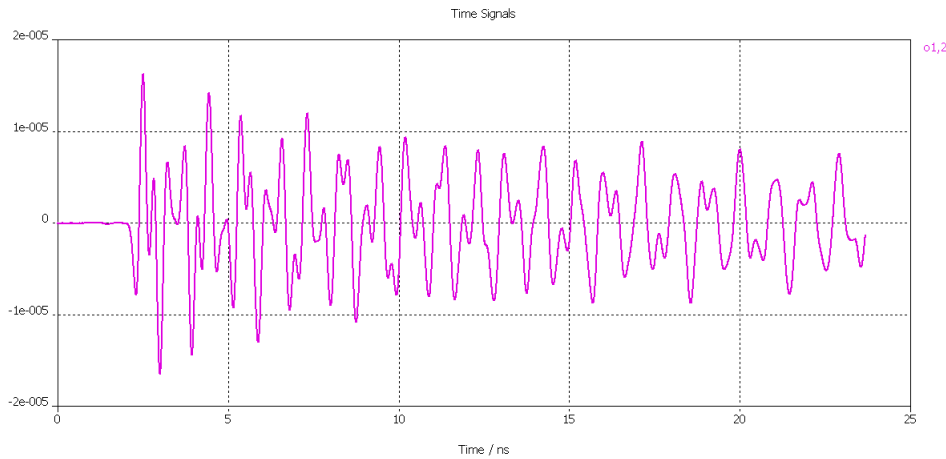


Figure 3-11: The output seen at the port of the field probe

All the results from the TD were Fourier transformed and compared with the FD results. From the TD results, an “ S_{21} ” measurement was created to see how well the TD setup compared against the fully calibrated VNA system of the FD setup. An advantage of the TD measurements was the favourable signal to noise ratio resulting from the large injected pulse. In addition, a single TD measurement contained all the data for the entire frequency range, as well as physical information such as origin resonances. In comparison, the VNA always measure the results to a normalised input.

For the FD results, the two-port S-parameters were exported for each of the measuring positions of the Fprobe, seen in Figure 3-12 (a.). Using the E-field monitors from CST, the final probe positions were chosen at a frequency of 1 GHz, Figure 3-12 (b.). One position was at the maximum (P4) while another was placed at a minimum/null point in the field (P2).

3.4. Conclusion

The results from the EPE simulation were used in CP calibration. The final calibration will show that correcting for the CFF is a useful tool and is necessary when the probe is to be used for observation purposes. The SMA material probe simulation proved results that allowed both TD and FD measurements to be compared to the simulation.

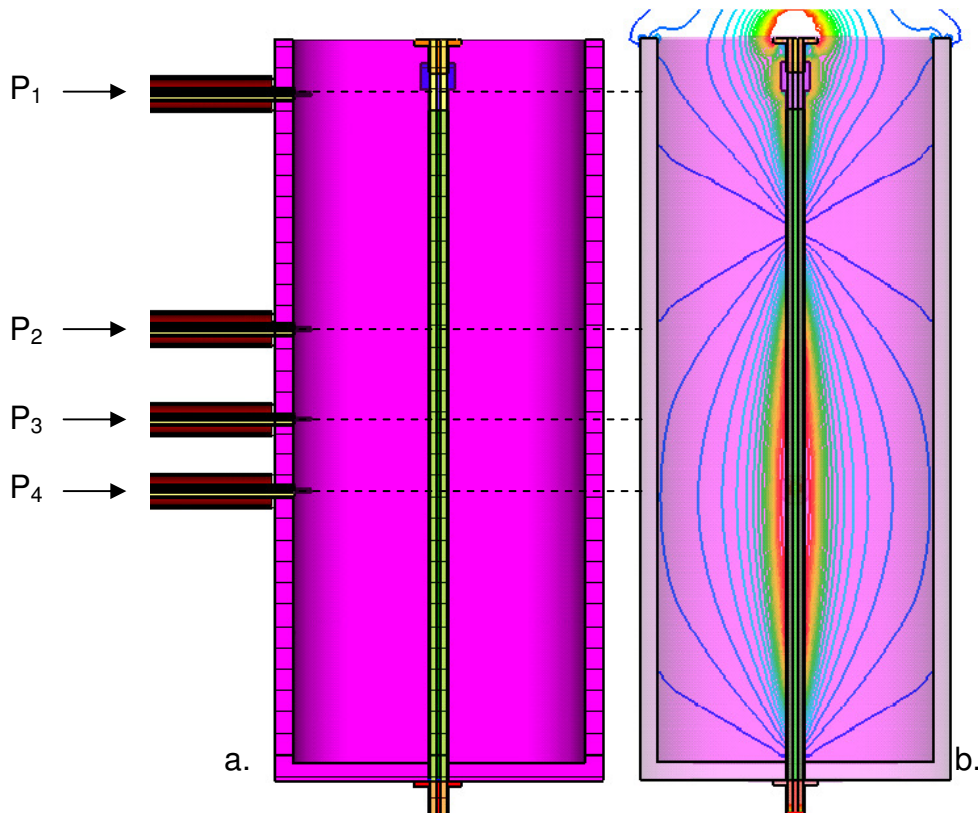


Figure 3-12: The positions of the field probe (a.) and the corresponding field strengths (b.) for the E-Field monitor at 1 GHz. The results at this frequency were used to pick the location of these measuring points

This chapter demonstrated that CST is a valuable tool in the prediction of results. The experimentally measured results that will be discussed in Chapter 4 and Chapter 6, correspond well the simulated results.

3.5. References for Chapter 3

- [1] Catalogue Edition 2001, *Suhner Coaxial Connectors General Catalogue*, Huber+Suhner Inc, Essex, USA

Chapter 4 : Current probe calibration for common mode current investigation

4.1. Introduction

In all fields of engineering, calibrated measurements are important. In the specific field of electromagnetic compatibility (EMC), the reliable measurement of currents is invaluable in the quantification of system tolerances. In general, a common mode (CM) current of the order of microamperes (μA), flowing on an external system cable or along the outside of a device, will lead to system failure in most emission regulations.

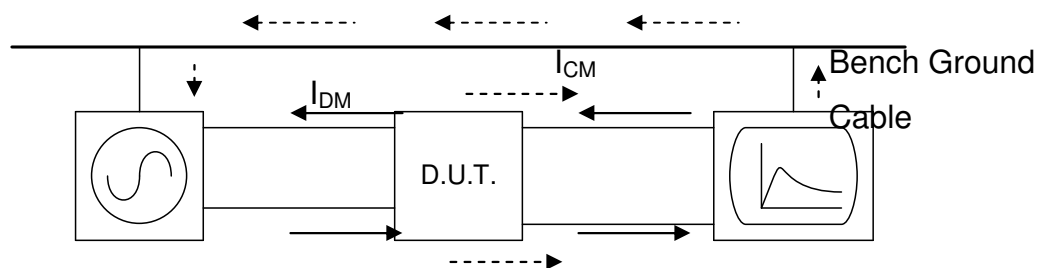


Figure 4-1: A common experimental setup illustrating differential mode and common mode currents occurring in the laboratory

The difference between differential mode (DM) and CM current can be explored using the following example. Figure 4-1 illustrates a simple experimental setup, where a device under test (D.U.T.) is connected between a signal generator and a spectrum analyser (SA). I_{DM} represents the DM current that flows between the generator, the D.U.T. and the SA. At any point in the cross-section of the connecting cables, the DM current sums to zero. This current path is represented in Figure 4-1 by the solid arrows. CM current (I_{CM}), is any current that flows along an unintended path. The dashed arrows in Figure 4-1 show a possible path that the CM current might follow. It must be noted, however, that there may be more than one path available to the CM current. These paths are influenced by the experimental setup and the quality of the connectors and cables used.

In coaxial cables, under normal DM operation, the inside of the sleeve acts as the ground return path for the current flowing on the centre conductor. The CM

current, could be caused by current leaking from the inside of the coaxial cable through the braiding of the shield or could be excited from an external interference. Using the same argument of current passing through the outside shield, this will introduce an additional current that will be measured by the device in Figure 4-1.

The CM current can be measured using a clamp-on current probe. In this study, the current flowing on the cable was measured with a 94111-1L current probe (CP) from EMCO, attached to a reliable detector. The current is directly related to the voltage induced at the terminals of the probe by a relation called the transfer impedance (Z_T). The transfer impedance relates the output voltage of the probe (V_P) to the CM current flowing on the cable using Ohm's law:

$$I_{CM} = \frac{V_P}{Z_T} \tag{4-1}$$

It is standard procedure for the manufacturer to supply calibration curves for the probe over a range of frequencies. The frequency range for the probe discussed in this chapter is 20 Hz-1 GHz. This calibration is always performed within an intended 50 Ω coaxial environment as specified in [1]. This is not, however, the practical environment in which these probes normally operate. The goal of this chapter is the calibration of these probes within realistic non-50 Ω conditions and the comparison of these findings with the manufacturer's data.

4.2. Current probe calibration

4.2.1. Background

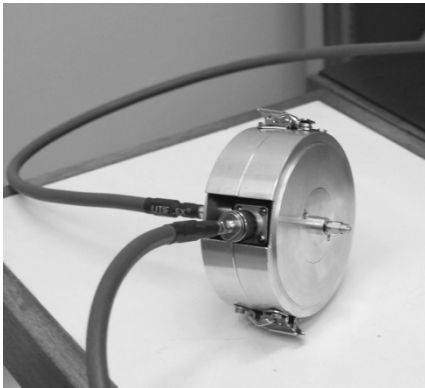


Figure 4-2: A version of the CISPR 16 [1] calibration enclosure, designed by Christo Nicholls (MScEng, 2007)

CM current probes are calibrated during their manufacture according to standard methods, such as those set out in [1]. In this method, an approximation of which can be seen in Figure 4-2, the probe is placed within a 50 Ω enclosure. A known current is injected and the resulting voltage across the probe terminals is measured. From this information, the Z_T of the probe is calculated. The accuracy of this calibration method is brought into question when the probe is placed in a non-50 Ω environment, such as a wire over a ground plane. In this chapter, alternative options are investigated to demonstrate the deviation between the supplied calibration material and the measured calibration values.

The most common problem in calibration procedures is the availability of a reliable standard. For a vector network analyser (VNA), calibration kits are available. This standard allows measurements to be repeated reliably and is traceable back to international standards. However, for the calibration of a current probe, no such standards exist.

One way to overcome this is to simulate the current flowing on a wire in a carefully configured environment. Moglie, Pastore and Primiani [2] made use of a FDTD (Finite Difference Time Domain) code, implementing a Yee algorithm, to simulate a plane wave on a piece of wire. Physical measurements were obtained in a reverberation chamber, which isolated the measurement from ambient interference. Inside the chamber, the wire was placed inside a predefined working volume and a stirrer was added to ensure the EM waves were distributed as evenly as possible over the volume. A tri-axial field sensor was used to measure the E-fields in all three orientations. The current probe was measured at three points along the wire, while the entire system was irradiated with a wideband LPDA (Log-Periodic Dipole Array). The LPDA and CP are connected to port one and two, respectively, of the VNA.

Moglie et al. measured two CP from different manufacturers: an F-61 from FCC (Fischer Customs Communications) and a CT-1 from Tektronix. Table 4-1 lists the calculated and supplied transfer impedances, which, at lower frequencies, differ by up to 8.2 dB.

For the purpose of EMC measurements an accuracy of at least 2 dB is allowed, however for most EMC regulations a variation of 6 dB is still acceptable. The CP calibrated in this chapter, will be used in measurements that are more accurate in which a precision of less than 1 dB is required.

Table 4-1: Supplied and calculated transfer impedance. A tolerance of ± 2 dB and ± 0.7 dB for the F-61 and CT-1, respectively, are specified by the manufacturer

Freq [MHz]	F-61 [dB Ω]			CT-1 [dB Ω]		
	Calculated	Supplied	Difference	Calculated	Supplied	Difference
250	32.02	26	6	21.89	13.7	8.19
500	27.47	26	1.4	16.09	12.6	3.49
750	24.84	25	0.16	13.51	12.1	1.41
1000	24.71	24	0.71	12.24	11.5	0.70

4.2.2. Theoretical modelling

To calibrate a current probe, a known current is required. To accomplish this, the current was calculated and simulated on a well-defined transmission line. Figure 4-3 shows the EMCO probe enclosure (EPE) used for the calibration. For these calibrations, two EPE's were created. The larger one used in the discussion which follows, as well as a smaller one. The EPE simulates a wire/cable over a ground plane with a characteristic impedance of $Z_{EPE} = 276 \Omega$. The conductor inside the EPE was a 2mm brass rod, kept a constant height above the ground plane, with each end of the rod connected through the side wall of the EPE by SMA female connectors, Table 4-7 shows the dimensions for the EPE.

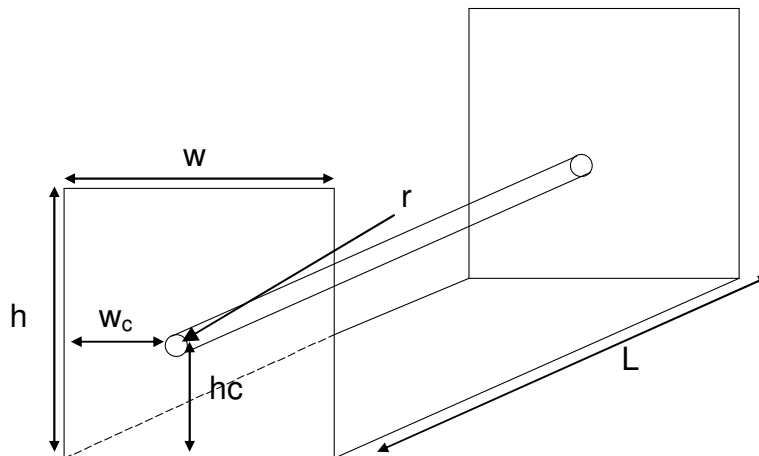


Figure 4-3: EMCO Probe Enclosure (EPE)

Table 4-2: Dimensions for the EPE seen in Figure 4-3

Length	L	505	mm
Height	H	300	mm
Width	W	300	mm
Wire height	hc	50	mm
Wire spacing for the side	wc	125	mm
Wire radius	r	1	mm

Table 4-3: Distances for different points along the wire. P1 – P9 are measuring positions and PL is the total distance towards the load

PS	P1	P2	P3	P4	P5	P6	P7	P8	P9	PL
0	155	180	205	230	255	280	305	330	355	505

Because of the length (L) of the EPE, standing wave effects occurred at higher frequencies as L approached $\lambda/4$. For this reason, measurements were made at different positions along the wire to compensate for this effect. Table 4-3 lists these measurement points, as along with other important distances.

Due to the large bandwidth of the 94111-1L, measurements were divided into three frequency ranges: low band (20 Hz to 100 MHz), medium band (100 MHz to 500 MHz) and high band (500 MHz to 1 GHz). A further measurement was also carried out at a frequency that is out of band. Table 4-4 lists the frequencies as well as their wavelengths in free space.

Table 4-4: The frequencies used for the investigation into the calibration of the 94111-1L current probe

Band	Frequency (MHz)	Wavelength (m)
Low	50	5.996 \approx 6
Medium	400	0.7495 \approx 0.75
Upper	900	0.333

For the investigation into the calibration, the standing wave effect had to be taken into account. Therefore, a CFF, based on the standing wave pattern was created. The basic transmission line equations were used in an analytical approach to calculate the input impedance and characteristic impedance of the EPE. The standing wave pattern for the voltage (SWP_V) and current (SWP_I) were approximated using the graphical aid of the Smith Chart [3]. The Smith Chart was however, only

used for the illustration of the principle. The final form factor was calculated using the CST model described in Chapter 3.

4.2.3. Calculations and Smith Chart

For the large EPE, the calculated characteristic impedance was:

$$Z_{EPE} = 276\Omega$$

With Z_{EPE} known, the EPE could be treated as a normal lossless transmission line with a known load at a distance of 505 mm. The input impedance seen by the source at each frequency, was calculated using (4-2). The value of Z_L was 50 Ω for the termination at the end of the transmission line. Table 4-5 lists the values calculated for each frequency.

$$Z_{in} = Z_{0E} \frac{Z_L + jZ_{0E} \tan \beta l}{Z_{0E} + jZ_L \tan \beta l} \quad (4-2)$$

$$\beta = \frac{2\pi}{\lambda} \quad (4.3)$$

Table 4-5: Values for the input impedance seen by the source at the input of the EPE with a 50 Ω termination at the end

f [MHz]	50	400	900
Z_{in} [Ω]	65.69 + j126.67	177.27 + j340.56	50.00 + j1.46

From the known value of Z_{in} , the input voltage (V_{in}) was calculated. V_{in} is calculated by assuming that the signal generator is delivering a known amount of power into a 50 Ω load. Figure 4-4 (a.) shows the circuit configuration.

From this the Thévenin voltage (V_{th}) can be calculated. Using V_{th} and connecting a known impedance, shown in Figure 4-4 (b.), the input V_{in} and I_{in} can be recalculated for each Z_{in} .

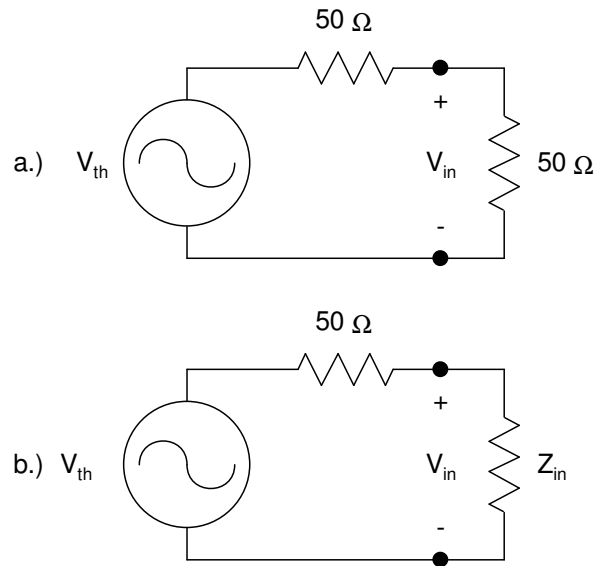


Figure 4-4: A circuit diagram of a signal generator with a known load.

- a.) The circuit when a matched load is connected
- b.) The circuit with a known impedance connected

$$I_{in} = \frac{V_{in}}{Z_{in}} \quad (4-4)$$

With I_{in} , as well as the correct theoretical form of the current obtained from the standing wave pattern on the transmission line, the theoretical current can be accurately predicted at different positions on the line. The SWP_1 was determined with the aid of the Smith Chart. In Appendix B the Smith Chart method is illustrated.

Table 4-6 shows the predicted SWP_1 for each frequency using the Smith Chart. The CST model of the EPE speeds up the computation of the form factor as described in section 3.3.1.

Table 4-6: The SWP_1 determined using the Smith Chart method

f [MHz]	PS	P1	P2	P3	P4	P5	P6	P7	P8	P9	PL
50	1.445	1.545	1.565	1.575	1.585	1.6	1.605	1.615	1.625	1.635	1.655
400	0.875	1.62	1.538	1.385	1.2	0.93	0.655	0.412	0.36	0.56	1.642
900	1.638	1.498	1.64	1.455	0.945	0.385	0.695	1.25	1.59	1.6	1.638

4.3. CST Final modelling for the large EPE

The CST model created for the EPE could be easily reconfigured to investigate its properties. The model was constructed from the relationship between the 16 variables seen in Table 4-7. The model developed in this way can be seen in Figure 4-5.

Table 4-7: Variables for the construction of the large EPE's CST Model

Variable	Description	Value [mm]
H	Height of the EPE	300
L	Length of the EPE	505
W	Width of the EPE	300
R1	Radius of the hole in the plate for the connector	2.65
Rc	Radius of the Conductor in the EPE	1
Wc	Width-Position of the conductor	125
Hc	Height-Position of the conductor	50
D	Thickness of the plates	0.2
SL	SMA: connector's length	9.3
SR1	SMA: Outer connector radius	2.45
SR2	SMA: Inner connector radius	2.05
SR3	SMA: Conductor radius	0.475
SW	SMA: Width	12.7
Sd	SMA: Thickness of the mounting	1.6

Section 3.2.1 details the exact method by which the EPE was modelled in CST. This chapter also gives a detailed account of how the data from the simulation was collected from CST and processed.

The second smaller EPE was developed to investigate the effect of the electrical length on the correction for the current variation. The dimensions of this EPE can be found in Appendix C, Table A 3. The smaller EPE was modelled using the same method described in section 3.2.1.

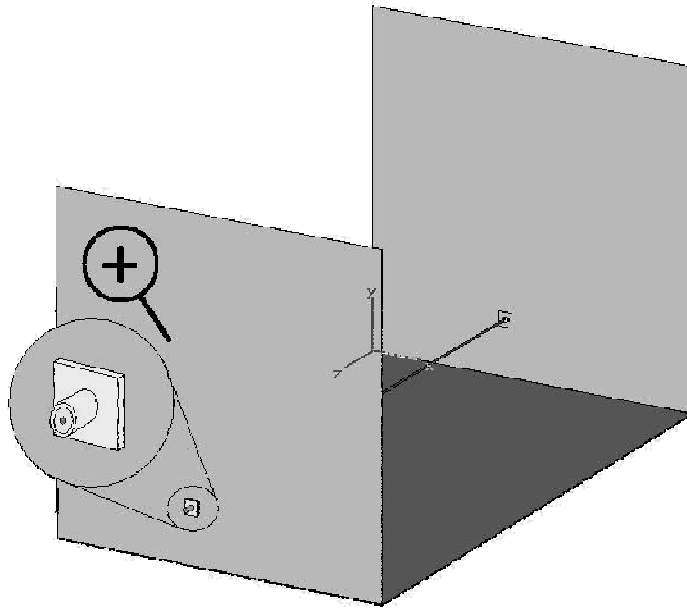


Figure 4-5: CST model created for the large EPE

4.4. Experimental setup and measurement procedure

Two experiments were performed for the investigation of the CP calibration. The first used a spectrum analyser (SA) and signal generator (SG), while the second used a calibrated VNA. In the SA experiments, the CP was placed at specified points along the wire (see Table 4-3) and a known power at a specified frequency was injected into the system. The power was measured using the SA connected to the CP. This method is labour intensive and requires a power level calibration of the system for each frequency.

After a few preliminary experiments, an EPE resonance at around 120 MHz was noticed. From subsequent measurements, it was concluded that the both methods produced reliable results up to around 100 MHz. In order to allow for comparison of the two methods, the experiments were conducted at the following frequencies:

Table 4-8: The frequencies (MHz) used for the final calibration experiment of the larger EPE

f1	f2	f3	f4	f5	f6	f7	f8	f9	f10	f11
0.3	0.5	1	10	20	30	40	50	60	70	80

As the smaller EPE was almost 10 times shorter than the larger EPE, a frequency extension of ten times was achieved. The frequency range could then be increased to 500 MHz, adding six additional frequency points to the 11 listed above (see Appendix C). The measurement setup was identical for both jigs. All the results for the smaller EPE are tabulated in Appendix C while those obtained using the larger EPE are referred to throughout this discussion.

4.4.1. Spectrum Analyser measurement setup and procedure for the large EPE without using a VNA

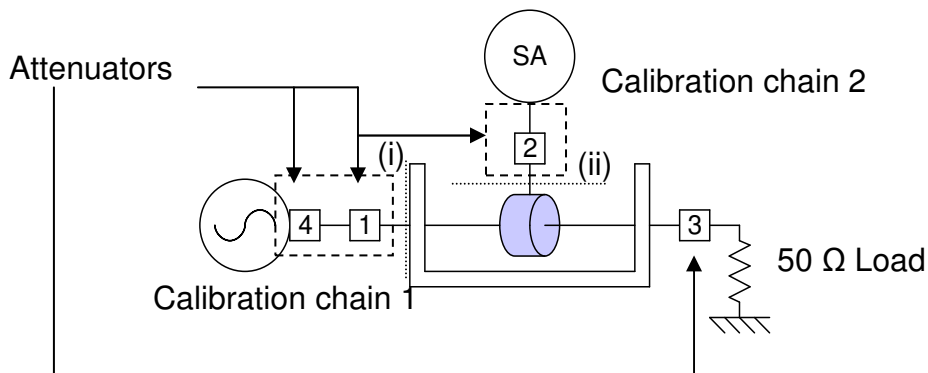


Figure 4-6: Experimental setup for the spectrum analyser measurements

Figure 4-6 illustrates the configuration for the SA measurement. The SA measurement was conducted on the assumption that no VNA was available. Therefore, four attenuators were used to buffer the mismatch from the EPE. Attenuators 1 and 2 were used to form two calibration planes (i) and (ii). The calibration removed the effect of cables and attenuators from the measurements.

Two calibration chains are defined (Figure 4-6): one for the source path and the second for the SA path. Chain 2 was connected directly to the output of the signal generator, with the output power set to 0 dB_m. This result, measured on the SA, gave

a relative value of attenuation in the chain 2 path. This procedure was repeated for all the frequencies listed in Table 4-8.

For chain 1, the Rohde&Schwartz (R&S) SML 03 signal generator was set to its maximum reliable output power, before compression, of 13 dB_m. The power, at (i) was measured at each frequency with these measured input powers then used for the analytical calculation of the input current. Table 4-9 lists the values measured in the final calibration.

Table 4-9: Values (dB_m) for the spectrum analyser method calibration of the large EPE. Chain 1 gives the input power at each frequency and chain 2, the attenuation in the probe path

	f1	f2	f3	f4	f5	f6	f7	f8	f9	f10	f11
1	9.34	9.46	9.54	9.51	9.49	9.46	9.41	9.44	9.41	9.42	9.39
2	10.41	10.40	10.41	10.42	10.42	10.45	10.49	10.52	10.57	10.55	10.56

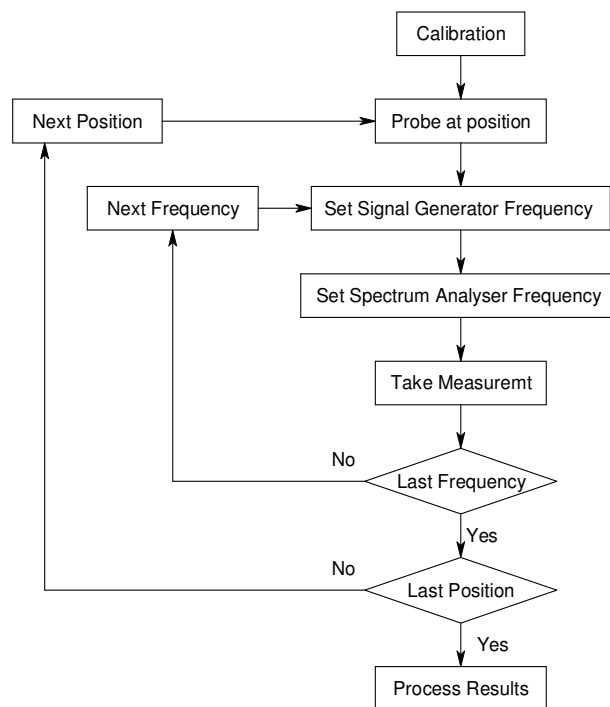


Figure 4-7: A flow diagram showing the method used for the spectrum analyser

Figure 4-7 shows a simple flow diagram describing this procedure. For the CP calibration, this method was time consuming. The measurement time was decreased by automating the “button pushing”. This was accomplished by connecting the SG and the SA through a General Purpose Information bus (GPIB) to a computer

controlled in the MATLAB environment. This new method can be represented by the flow diagram in Figure 4-8. Now the only input required from the operator is to change the position of the probe, thereby reducing the possible errors that could occur as a result of manual operation.

A calibration is only as reliable as the standard against which it is compared. In the case of the SA, only a relative calibration is performed as the SA is assumed to provide an accurate measurement. A more accurate device that could be used instead of the SA for the calibration is a power meter when a VNA is not available.

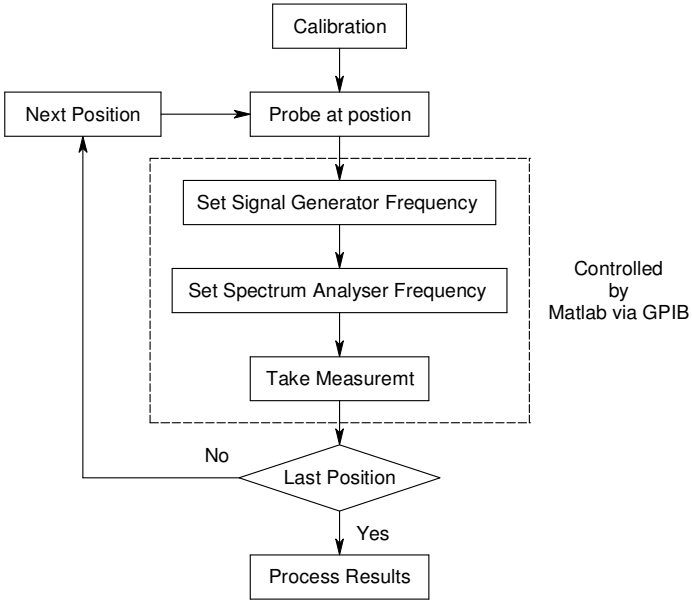


Figure 4-8: A flow diagram of the SA method when the measurement was automated through the GPIB interface.

4.4.2. Vector Network Analyser setup and measurement procedure for the large EPE

Vector Network Analysers (VNA's) are considered to be the most accurate, high frequency S-parameter measuring devices due to the standards used in the calibration process. These standards are machined very accurately [4], defined carefully [5] and are traceable to national standards laboratories. The VNA is able to mathematically remove the systematic errors of the measurement setup and cabling, creating a reference plane at the cable interface.

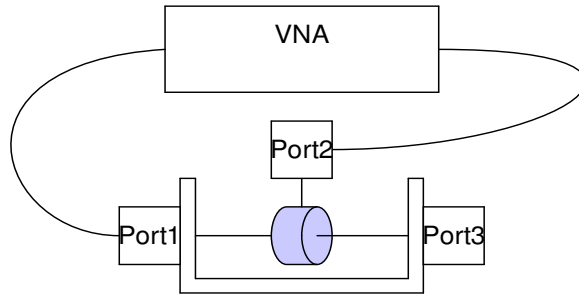


Figure 4-9: Setup for the network analyser, port three is terminated in a matched load

Figure 4-9 shows the setup used in the measurement of the transfer impedance. Once the data was retrieved from the VNA, these two-port parameters were converted into Z-parameters using (4-5):

$$Z = (I + S)(I - S)^{-1} \quad (4-5)$$

where $I = \begin{bmatrix} 1 & 0 \\ 0 & 1 \end{bmatrix}$

From the definition of Z_{21} , the value obtained was the transfer impedance of a system with an open-circuit at port 2. When a measurement was made using the SA, the value obtained was measured over 50Ω . To correct the open circuit from the Z_{21} definition for the 50Ω load, voltage division was necessary. At the same time, it was possible to correct for the current distribution with the current form factor (CFF). (4-6) gives the equation for these corrections:

$$Z_{TFF} = \left| \frac{Z_{21}}{CFF \left(1 + \frac{Z_{22}}{Z_0} \right)} \right| \quad (4-6)$$

The final phase of Z_{TFF} was not considered in this calibration as the CP was generally used in the frequency domain, with a peak detector. If this probe were to be used for time domain measurements, a calibrated phase value would also be needed to ensure accurate measurements.

4.5. Results and experiment refinement

Each experiment described was tested for repeatability. Thereafter, certain deficiencies were identified and refinements were introduced.

4.5.1. Final Spectrum Analyser based measurement

For the first measurements, the CP was placed on the EPE's ground plane and clamped around the wire under test. Initially, the conductor was kept as centred as possible, although it was later found that this had little effect on the final results.

A foam cradle was created to hold the CP centrally around the wire. This also allowed the CP to be accurately aligned with the measuring points. The final measurement setup is seen in Figure 4-10.

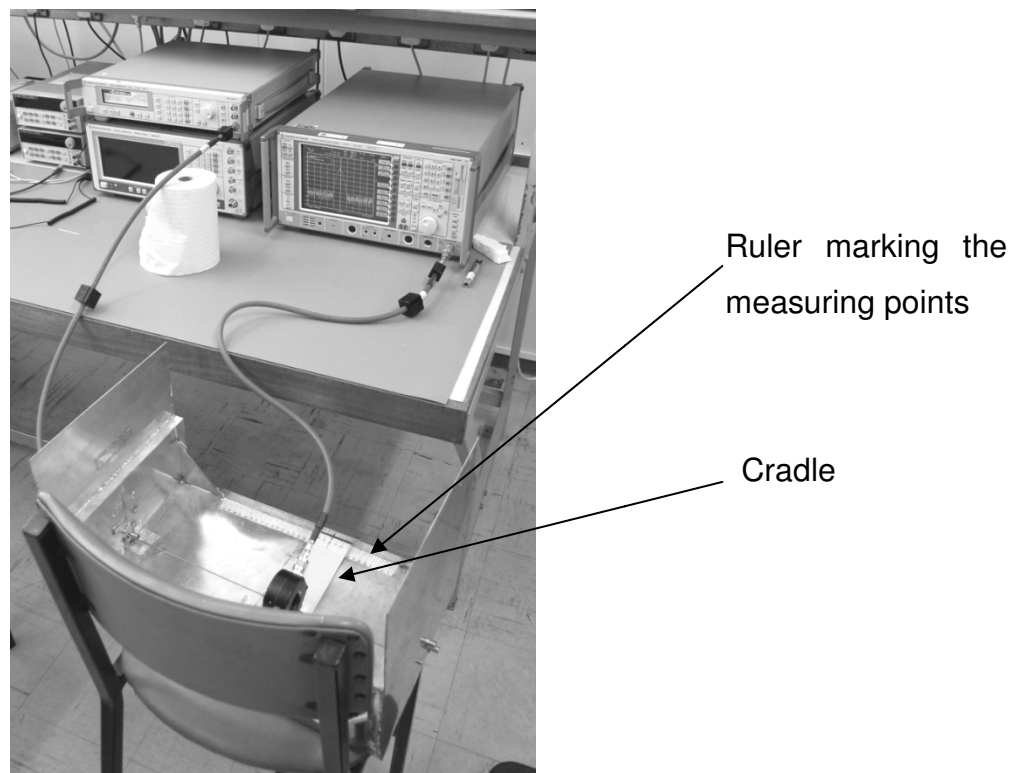


Figure 4-10: A final setup for the large EPE used for the spectrum analyser method

Figure 4-11 and Figure 4-12 compare the calculated and supplied transfer impedance for the SA method for both the larger and smaller EPE. From these results, it is clear that this method produced values for the transfer impedance which were similar to the manufacturer's published data and within 1.0 to 2.0 dB for the frequencies above and excluding 1 MHz. For the lower frequencies (300, 500 kHz and 1 MHz), the differences between the published and the calculated Z_T were more pronounced.

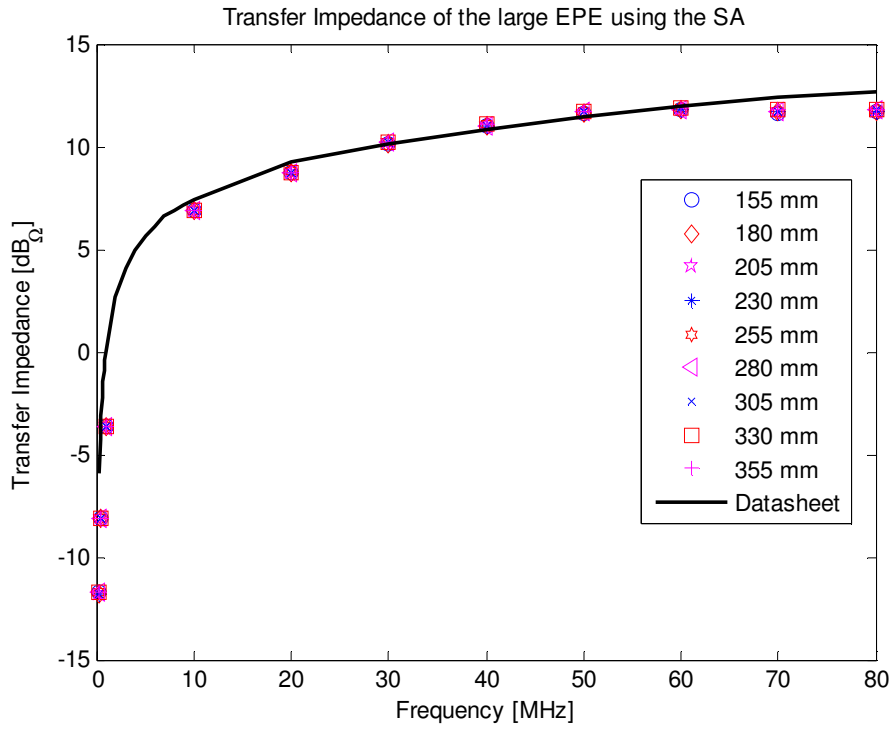


Figure 4-11: Transfer impedance of the large EPE determined using the spectrum analyser method

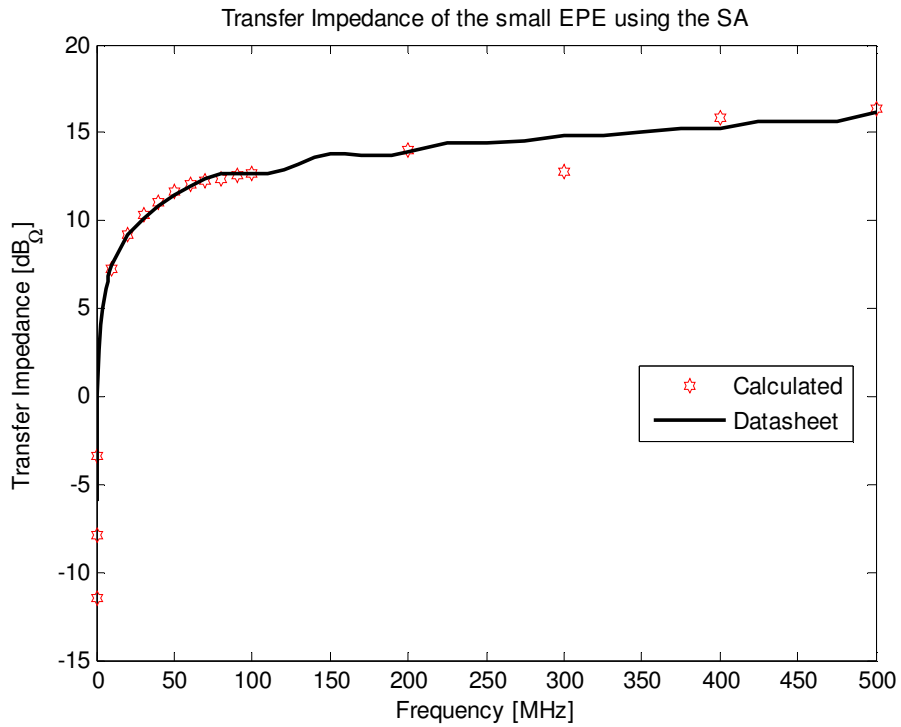


Figure 4-12: Transfer impedance of the small EPE determined using the spectrum analyser method

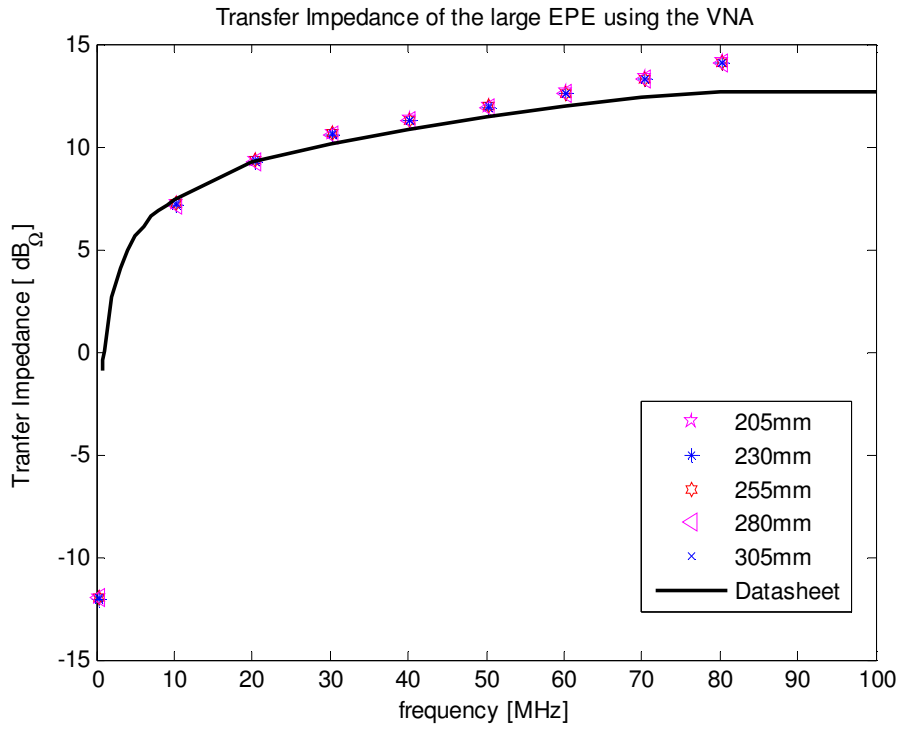


Figure 4-13: Transfer impedance of the large EPE calculated using the network analyser method

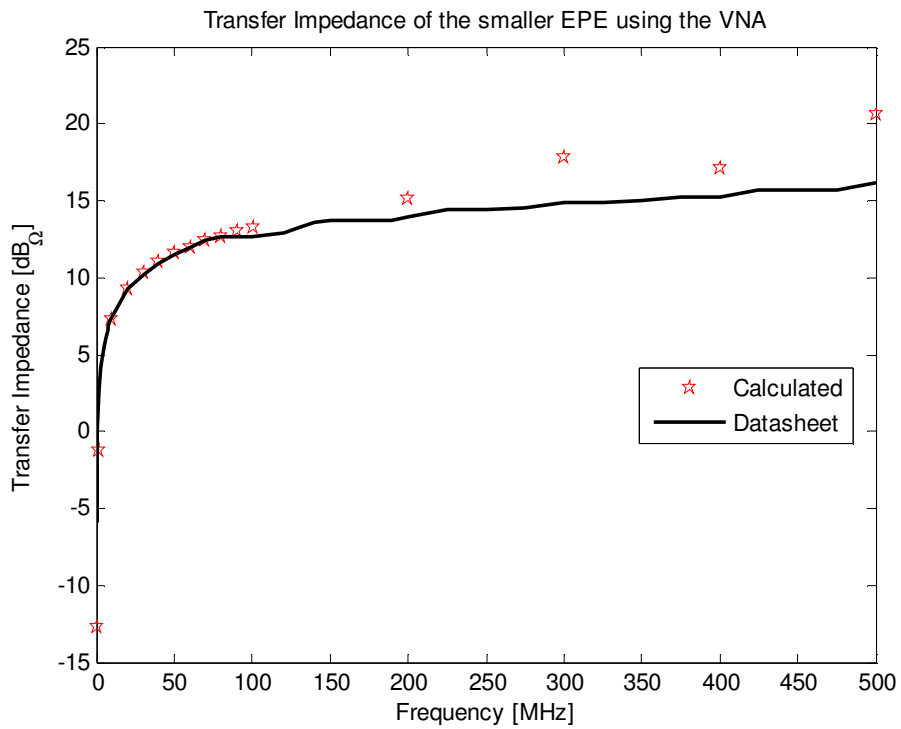


Figure 4-14: Transfer impedance of the small EPE calculated using the network analyser method

4.5.2. Final Vector Network Analyser measurement

When the first experiments were conducted with the VNA, the attenuators, used in the SA method, were left out of the measurement setup. It was assumed that the VNA's calibration process would compensate for the mismatches of the EPE. Because of high reflection coefficients, buffering was advantageous. To compensate for the attenuators, the output power of the VNA was increased

From the VNA results, in Figure 4-13 and Figure 4-14, it was clear that the calculated Z_T values are higher than the published data. Additionally, it appears that this difference increases with increasing frequency for the large EPE (Figure 4-13).

4.6. Conclusion for the probe calibration

The two methods, as well as the two EPEs, can be directly compared as can be seen from the data in Figure 4-15. The larger EPE was only measured up to 80 MHz while the smaller one was taken up to 500 MHz

The concept of using the form factor of the current to correct for wavelength effects has proven to be a useful tool, as the relation between the calculated and published data remains within 1 to 2 dB.

In conclusion, the following points can be summarised. When working with clamp-on current probes, it is advisable to avoid measuring cables or systems where the physical length of the system approaches a given frequency.

From the calibration discussed in the chapter, a statement can be made: that the data provided by the manufacturer was accurate, but the environment in which the probe operated affected the data measured by the probe. Any discrepancy of 1 to 2 dB between the measured and the expected data could be attributed to environmental effects.

The results for the smaller EPE corresponded more closely to published data and with less error than the results for the larger EPE. This was because the smaller EPE more closely resembled the CISPR 16 coaxial method. For both the smaller and larger EPE, the SA results agreed more closely with the published data than those measured by the VNA.

In the SA measurements, a higher signal to noise ratio could be achieved by directly applying more power at each frequency, while in the VNA all power levels were normalised by the calibration of the VNA.

The calibration of the CP demonstrated that, if the current was corrected for the effects of the standing waves, reliable measurements could be achieved. Unfortunately, because the CP was invasive and disturbed the field that forms around the D.U.T., the CP would not reach the required accuracy for measuring the small signals observed in Chapter 6. Therefore, the second method discussed in section 2.4.1 was used for the investigation into the CM current on the material property probe.

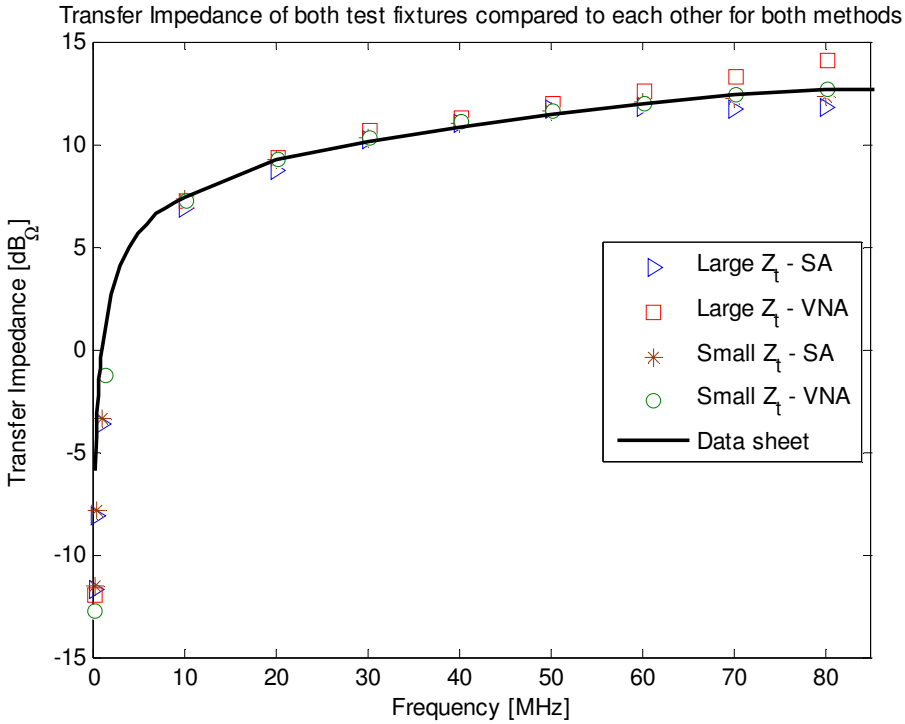


Figure 4-15: The final results for the transfer impedance. This graph compares the results for both EPEs, measured on the SA and VNA

4.7. References for Chapter 4

- [1] CISPR 16-1-2 edition 1.1 2004-06, pp. 77-93 odd pages only
- [2] F. Mogle, A.P. Pastore and V.M. Primiani, "*Current probe characterization in a reverberation chamber*", 2005 International Symposium on electromagnetic compatibility, Volume 2, Issue , Aug. 2005 pp 545-549
- [3] R. A. Chipman, "Graphical aids to transmission line calculations" in Theory and problems of transmission lines, first edition, Schaum's outline series. New York: McGraw-Hill, pp. 184-207
- [4] Agilent, Application Note 1287-3
- [5] Agilent, Product Note 8510-5B, Specifying Calibration standards for the Agilent 8510 Network Analyzer, pp. 9-16

Chapter 5 : Sampling oscilloscope setup and time-base correction

5.1. Introduction

In this chapter, the sampling oscilloscope used for the time-domain measurements will be described. A sampling oscilloscope is not a standard piece of equipment in most high frequency laboratories. The working of a sampling-scope differs from that of an analogue oscilloscope or newer digital counterparts.

For this work, a specific setup was required, so the NIST (National Institute of Standards and Technology) time-base correction (TBC) algorithm [2] could be applied to reduce errors in the sampling scope's time-base. The TBC method will be discussed in this chapter.

5.2. Sampling oscilloscope

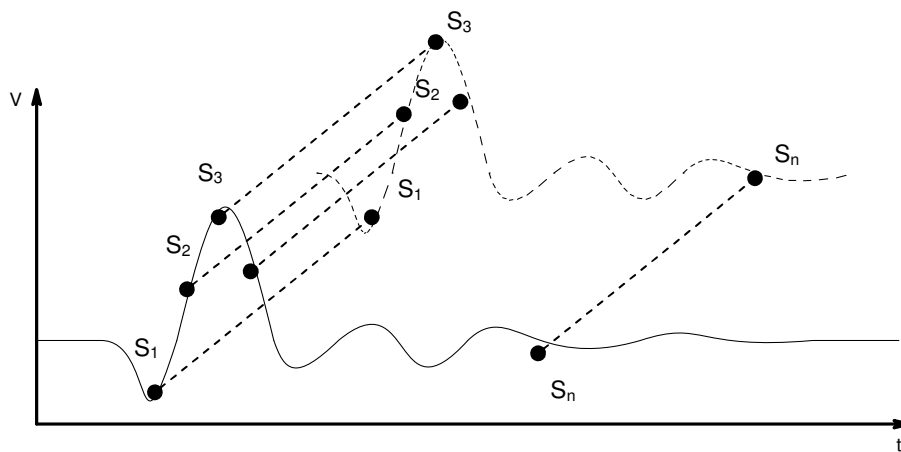


Figure 5-1: Real-time sampling with the reconstructed signal

In a real-time scope, the incoming signal is sampled for display on the screen or for data processing. The signal is made up from 1:1 sampling, as seen in Figure 5-1. The bandwidth of this class of scope is limited by the Nyquist criterion.

For a GHz sampling-scope, the high frequency signals being measured are too fast for the sampling electronics to allow 1:1 sampling. Therefore the signal is sampled over an extended period, Figure 5-2 shows this procedure. Each time the scope is triggered, one sample is taken from the signal. After the n^{th} sample, the signal is reconstructed onto a new equivalent time-scale. This procedure takes a certain amount of time (t_{con}).

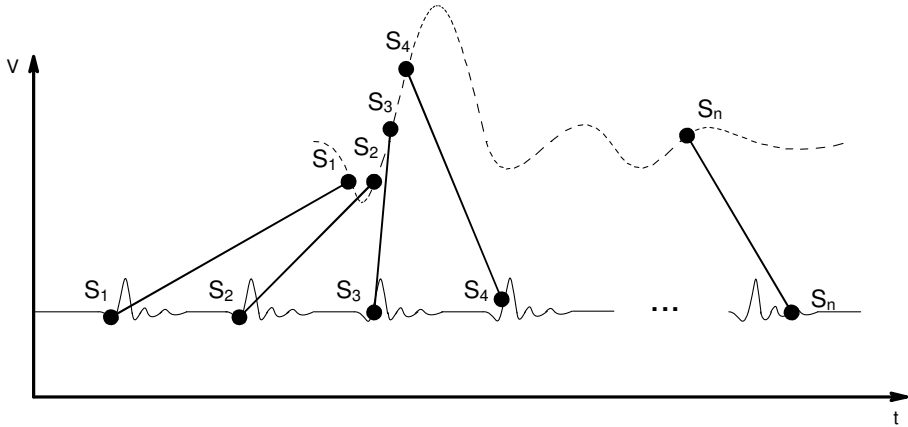


Figure 5-2: Sequential equivalent-time sampling showing the reconstructed signal

5.2.1. How sampling oscilloscopes work

5.2.1.1. Classic sequential equivalent-time sampling method

The sampling heads used inside a sampling-scope are standard RF sampling technology, which have been consistently undergoing development over the last 50 plus years. The method used rests on three key components: a trigger signal, a rising ramp generator and an incremental step generator [1].

In the classical sequential method, a ramp generator was started each time the trigger was sensed. Running synchronously with the ramp generator, was the step generator, which was incremented with each trigger. A sample was taken when the values of the step and ramp generator were equal. Figure 5-3 illustrates the principle, where the top signal is a waveform being measured. When the step generator reached the top of the ramp, the whole procedure was reset. This is known as the reset time (t_r) of the scope, and is normally much shorter than t_{con} .

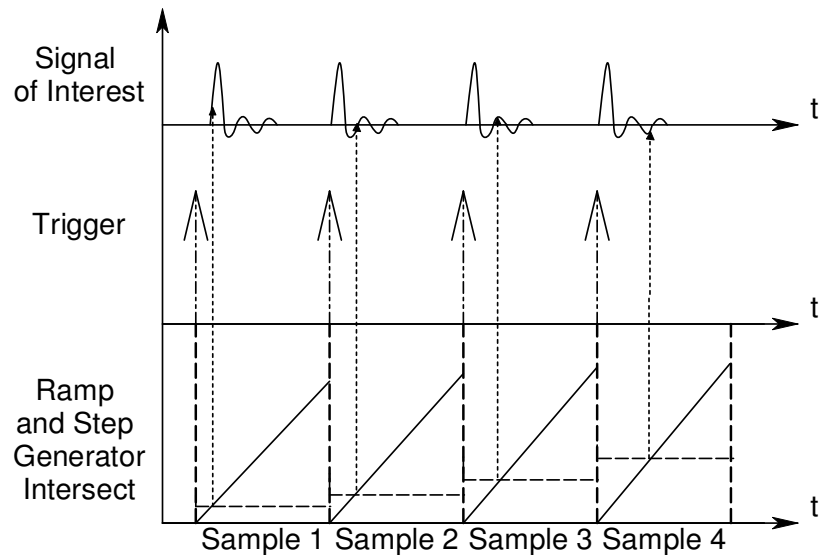


Figure 5-3: Diagram illustrating the basic principle behind a sampling oscilloscope in the classical sequential method

5.2.1.2. Modern method used in scopes such as the Agilent 54750A

In modern scopes, the trigger circuit is replaced with a phase-locked loop (PLL), which reduces errors in the time-base. This also simplifies the trigger and sampling circuits inside the scope. In the older scopes (pre-1970s) an impulse generator – normally an avalanche transistor circuit connected to a non-linear transmission line – was used to fire the sampling heads [1].

With the PLL, fast CMOS comparators can be used for sample triggering. This system does not have the drawback of cool down time of the impulse generators. This leads to increased sampling speed and reduced t_{con} and t_r .

For the Agilent 54750A:

$$t_{con} = 22ns$$

$$t_r = 4ns$$

5.3. Time-base correction from NIST

5.3.1. The TBC method

The TBC algorithm corrected for both the errors in the time-base and the jitter [2]. The software also corrected for errors that were created by t_r in the measured data. These small jumps in the time-base were seen as high frequency components when the data was Fourier transformed.

Using two quadrature reference sinusoids, at a frequency f_r , the TBC software fitted the measured signals to a mathematical model also at f_s . Quadrature signals were chosen because one signal is at a maximum while the other is at a minimum.

When the measured quadrature data was fitted to the mathematical model, the software located where the data time positions differed from the model. These errors were corrected and the positions logged. While the reference signals were being measured, the data signal of interest was also recorded. Knowing the error positions in the reference signals, the software could correct for the same time-base errors in the data signal.

TBC could also offer averaging of the signals. Here, N data sets were recorded with each data set consisting of the two reference signals and the data signal. When the sets were fed into the software, the algorithm took each set individually and corrected for the errors. Afterwards it interpolated all the sets onto one uniform time-scale and average to produce an N -times averaged, time-base corrected waveform.

The advantage of using this averaging above the scope's built-in method was that the scope could "smear" the signal if the jitter was significant. To illustrate the principle behind TBC and the possible advantages, the impulse generator built for this study was measured on the sampling scope, and the results processed using TBC.

5.4. Measurement setup and components

For the measurements with the material properties probe (see Chapter 6), the following experiment, incorporating TBC, was implemented for the time-domain (TD) measurements.

To enable the comparison of this TD data with the frequency-domain (FD) data and CST simulation, a broadband impulse was required. This pulse must deliver a reasonable amount of energy within a 3 GHz bandwidth.

5.4.1. Impulse generator

The impulse generator (IGen) consisted of a single avalanche transistor. An avalanche transistor works outside the normal operation region of standard transistors. The principle of these transistors is described in [3] using the circuit seen in Figure 5-4. In these circuits, it is common for the supply voltage (V_{cc}) to be in the region of 200V.

When the supply was connected, capacitor C_{out} charged through R_C and R_L until the collector voltage reached a value of between 70 and 190 V, as listed in [3] for the NS1110 used in this example ($V_{cc} = 200$ V). This collector voltage was affected by the biasing of the transistor.

When a positive rectangular pulse trigger was applied to the base, the transistor started to conduct. R_L and C_{out} created a dynamic load, which pushed the transistor outside of the stable region. This caused the collector voltage to collapse, causing the avalanche effect, until a stable operation point was reached. These switching times can be a nanosecond or less. When C_{out} was discharged, the current was insufficient to maintain the avalanche effect and the transistor switched off, allowing C_{out} to recharge until the next trigger was applied.

The IGen built for this study is seen in Figure 5-5, while Figure 5-6 shows the circuit diagram. The values of the components in the circuit are contained in Table 5-1. This configuration was considered a “*good rectangular pulse*” generator in [3]. By replacing C_{out} with an open-ended 50 Ω coaxial cable that acts like a capacitor, the impulse travelled down the cable when the generator was triggered. The impulse reflected off the open cable and returned as a negative impulse. This reflected pulse reverse biased the transistor and stopped the avalanching effect. By manipulating the cable length, the pulse width could be controlled. This pulse width is defined in the following equation:

$$Pulse_{width} = \frac{2 \times length}{v_p} \quad (5-1)$$

where v_p is the relative velocity of the dielectric material inside the cable.

The built IGen has two output paths. The one incorporated a step recovery diode (SRD). The SRD sharpened the rising edge of the impulse, seen in Figure 5-7, which resulted in a much higher frequency bandwidth. Figure 5-8 shows the power spectra for both output pulses.

Table 5-1: Component values for the impulse generator seen in Figure 5-6

Component	Value	
C_{in}	130	pF
C_{Out}	10	nF
C_{Delay}	100	pF/m
R_B	68	Ω
R_C	120	k Ω
R_E	47	Ω

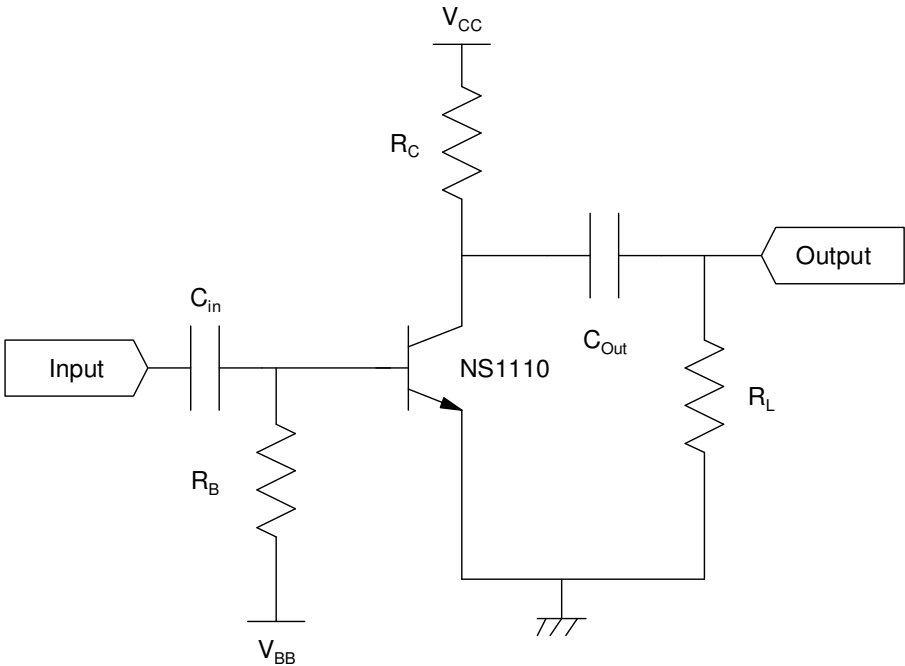


Figure 5-4: A typical circuit for high-power impulses (after Fig 1c in [3])

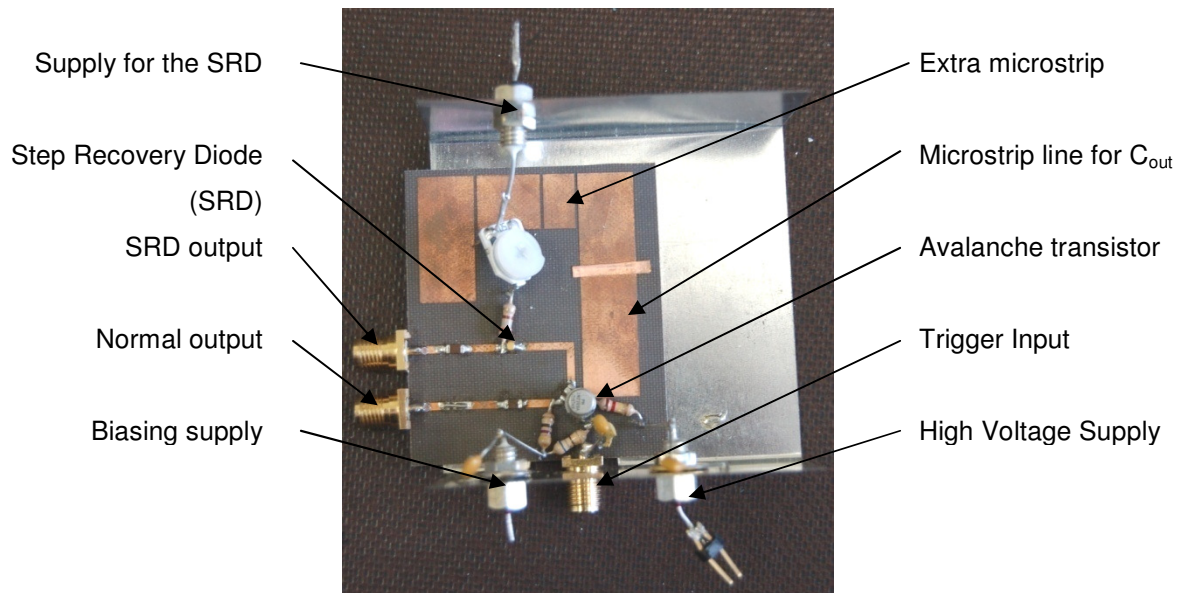


Figure 5-5: The built IGen used in this study. Here the coaxial cable is replaced by a 50 Ω microstrip line with connecting strips for extra length

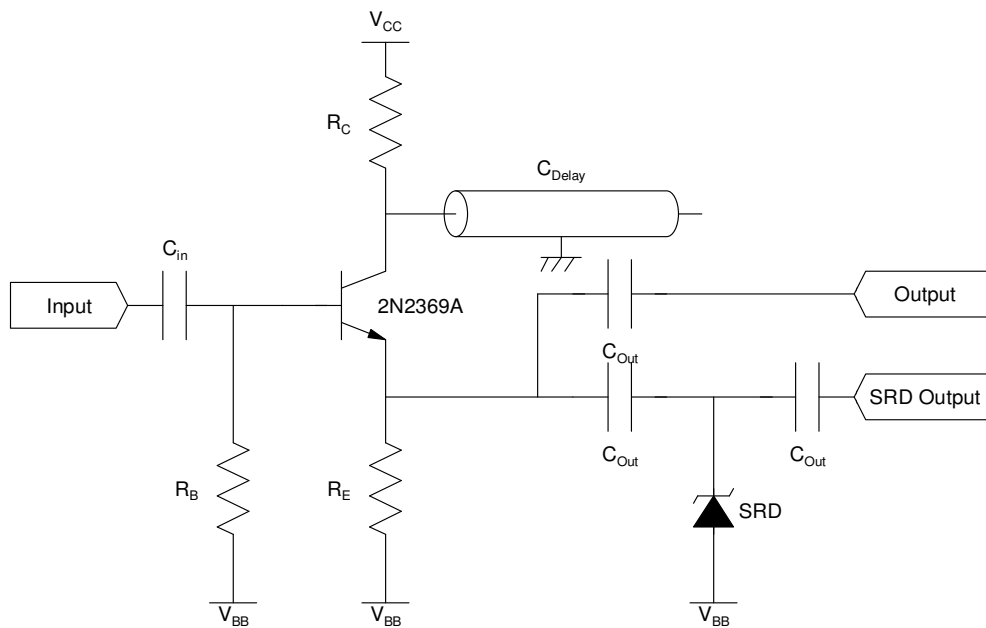


Figure 5-6: Circuit diagram of impulse generator with a SRD output and a normal output

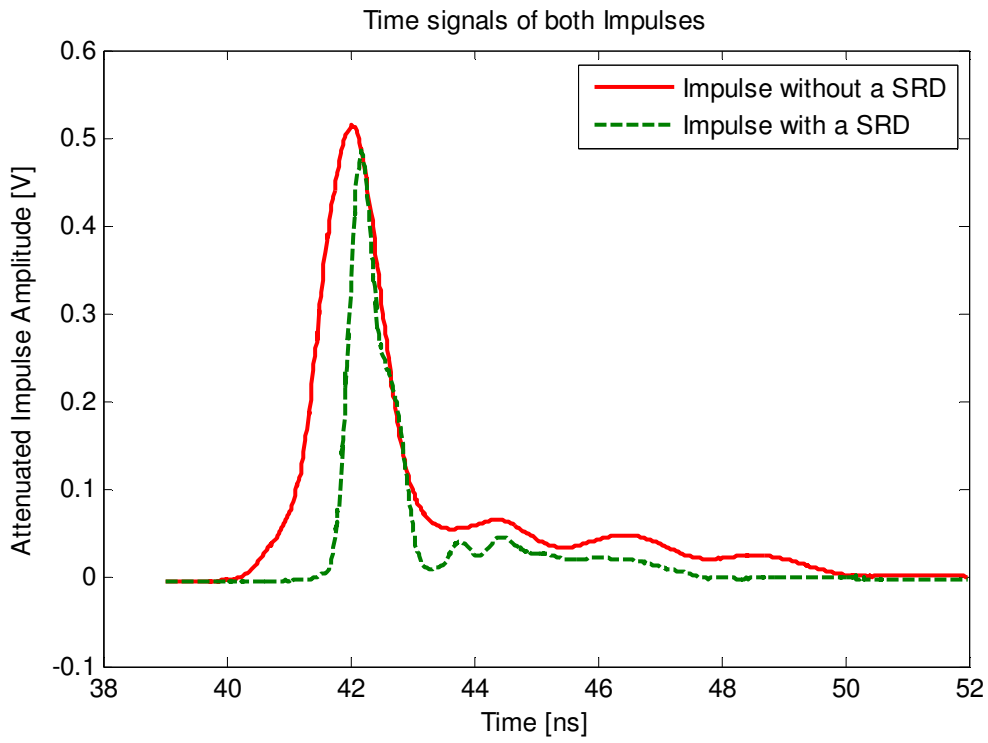


Figure 5-7: A time-domain representation of both impulses that the IGen can produce

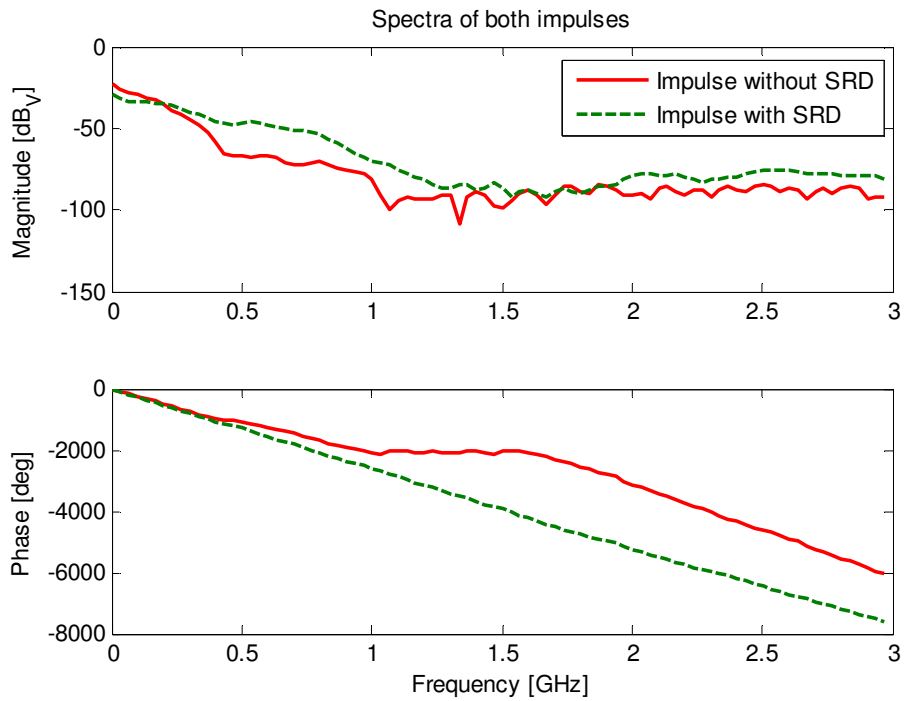


Figure 5-8: The spectra of the two impulses generated by the IGen

5.4.2. Signal sources

For the IGen, a very stable square-wave generator was required for triggering as a signal with enough jitter can lead to a misfiring of the avalanche transistor. The same step generator was also needed for the triggering of the sampling scope. The TBC software required two quadrature sinusoids.

Because the scope used a PLL for the triggering, the sampling was directly connected to the phase of the trigger signal. Therefore, it was important that all the generators were in phase. Even a small difference in phase could have led to one or more of the signals being mis-sampled.

Earlier experiments showed that when the same signal was used for triggering both the IGen and the sampling scope, the impulse leaked into the triggering path causing difficulty in the triggering of the scope. It was also possible that the avalanche transistor could misfire due to biasing or temperature effects. This made the impulse unreliable for triggering of the sampling scope.

A stable triggering configuration was formed using the Rohde & Schwarz AM 300 function generator, with two output channels, and the Agilent 8647A 250 kHz-1000 MHz signal generator. These generators were synchronised by connecting the 10 MHz reference output of the AM 300 to the reference input of the 8647A. This synchronised the internal oscillators of the generators and ensured that there was little to no phase drift between the trigger and measured signals.

5.4.3. Final Setup

Figure 5-9 shows the final setup used for the TBC measurement. When the IGen was measured using a more common high-impedance oscilloscope, the output was 17 V across 50 Ω load. This exceeded the input levels of the sampling scope as the sampling heads have a maximum allowed level of $\pm 2V$. Therefore 30 dB of attenuation was added to protect the measurement equipment. This added attenuation also provided a load impedance closer 50 Ω for the IGen.

All the scope functions and data collection was controlled by a MATLAB function via the GPIB interface. The Agilent 8647A was set to a power output of 0 dB_m and a frequency of 300 MHz. Both channels of the AM 300 were set to a frequency of 50 MHz and an amplitude of 1.4 V_{p-p}.

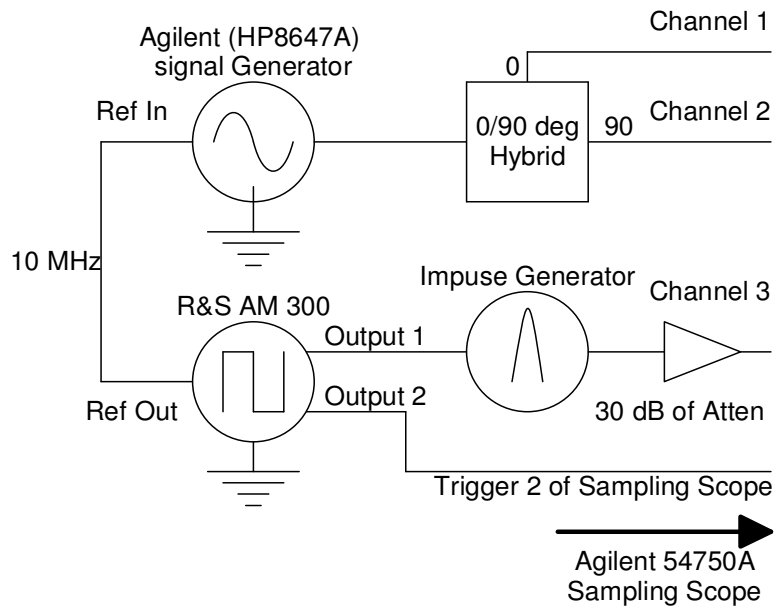


Figure 5-9: The final setup for the TBC measurement and the template for the final measurement with the material-probe

5.4.4. Example using the impulse generator

To explain how TBC works, only the impulse without the SRD will be used in this section. The TBC results for the impulse with the SRD can be seen in Appendix E. The impulse and the two reference sinusoids formed one data set. For the TBC averaging, 100 of these datasets were collected. Each set was saved in a separate file, which was used by the TBC for post-processing.

A “scope-averaged” waveform, created manually using the individual data sets, was used for comparison. Creating this waveform manually retained the time-base errors in each separate waveform. Allowing the scope to average will create 100 new time-base errors. Figure 5-10 shows this averaged waveform (solid) while the dashed line shows the original waveform.

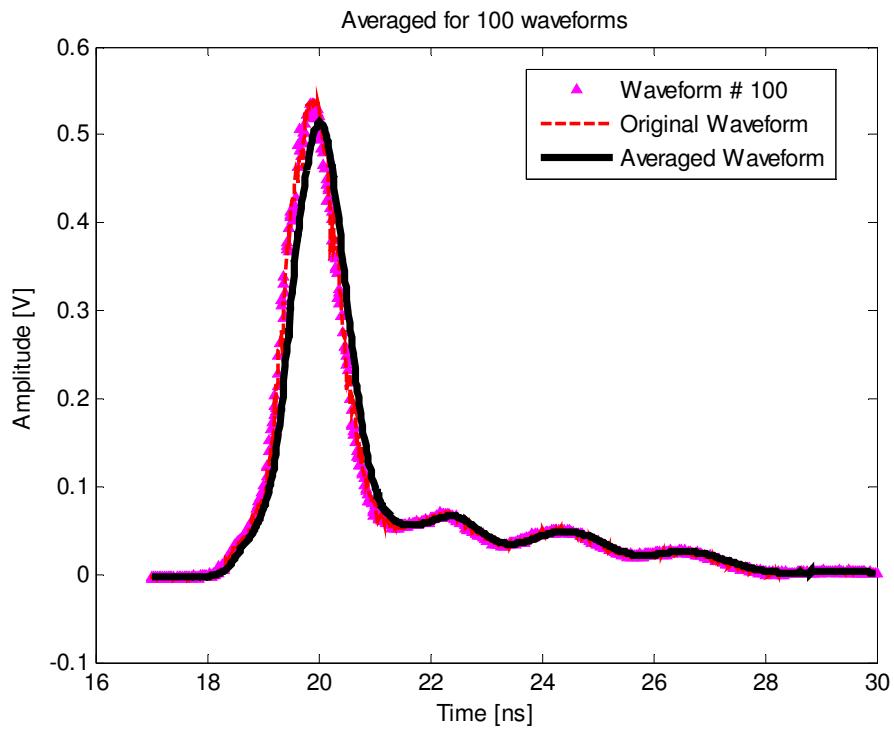


Figure 5-10: A graph showing the original waveform (dashed), the 100th waveform and the averaged waveform (solid line)

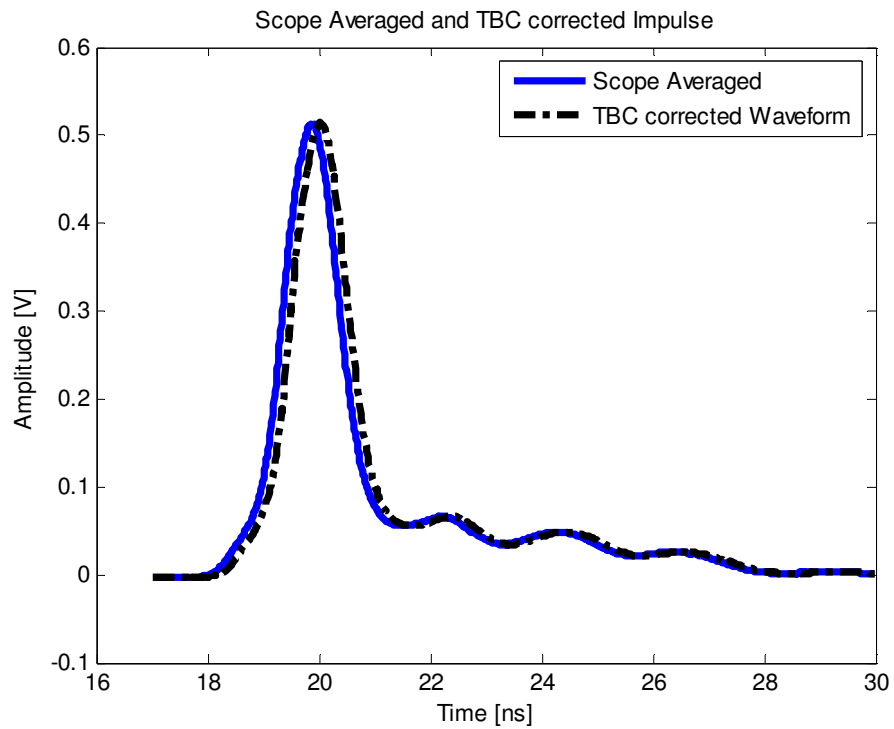


Figure 5-11: The solid line represents the scope-averaged waveform, while the dot-dash line represents the TBC corrected and averaged waveform.

5.4.5. Results from TBC (To TBC or Not to TBC !?)

Figure 5-11 shows the time-domain results for the two methods for the output without the SRD. Figure 5-12 and Figure 5-13 display the spectra of both impulses. Examining the time-domain signals, a clear phase difference was seen. This was confirmed by looking at the linearised phase. The phase was linearised by subtracting a constant phase over the frequency range and the slope, determined by taking the first and middle values of the phase. This gave a better resolution than when comparing the phases.

Looking at Figure 5-13, TBC does indeed make a difference to the impulse with the SRD. Although it seemed that TBC was decreasing the magnitude over 2.2 – 3.5 GHz, it was in fact removing the effects of the sampling process. This provided a more accurate representation of the impulse, which was important for the time-domain measurements on the material property probe (Chapter 6), where the impulse was used as the input.

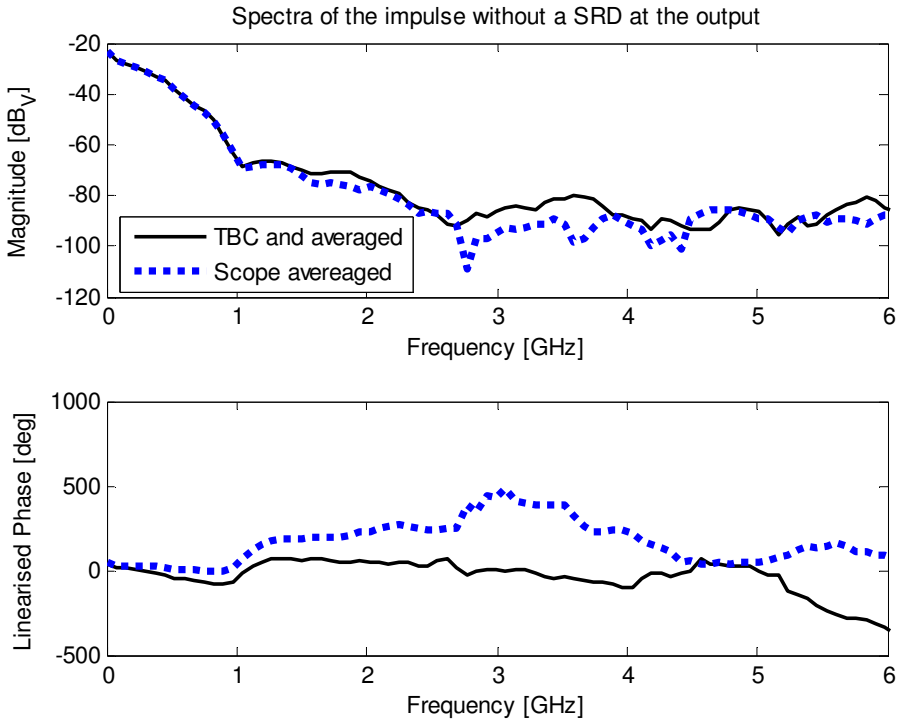


Figure 5-12: Spectrum of the TBC and oscilloscope averaged impulse with no SRD at the output

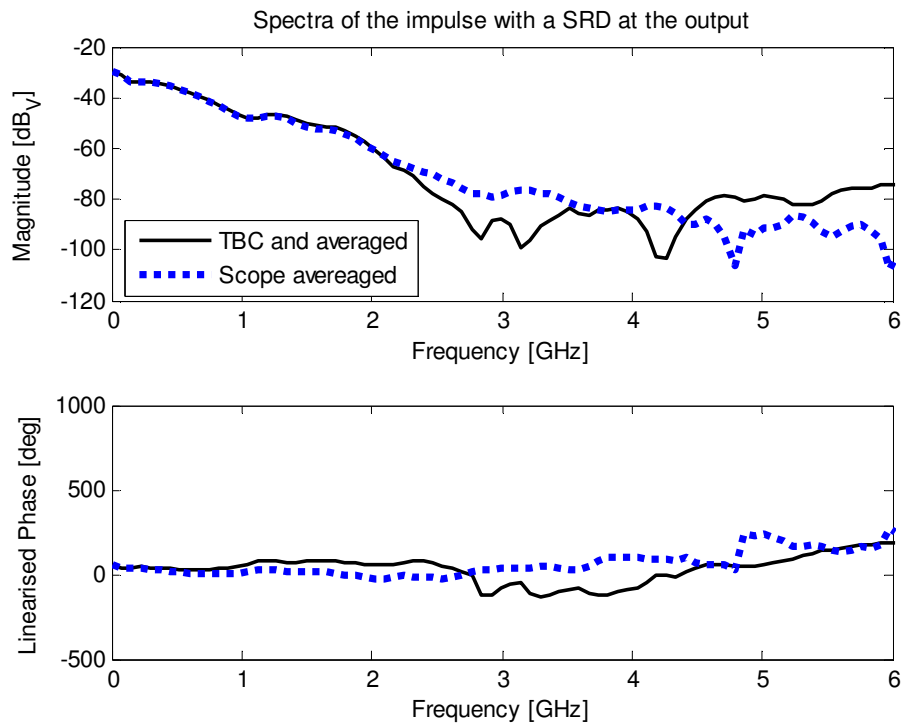


Figure 5-13: Spectrum of the TBC and oscilloscope averaged impulse with a SRD at the output

5.5. Conclusion

In this chapter, the basic principle of a sampling scope was described. A sampling scope operates differently to its real-time counterparts. Signals measured on the sampling scope were reconstructed on an equivalent time-base that introduced systematic errors in the data. These errors affected the accuracy of measurements conducted on these instruments.

The experiments performed here, demonstrated the factors which must be taken into consideration when working with a sampling scope, as well as a method of generating high frequency impulses using an avalanche transistor circuit. The algorithm developed by NIST illustrated how errors from the sampling process were removed to provide a more accurate representation of the measured data.

For the measurements discussed in Chapter 6, the impulse with the SRD at the output will be used. This impulse was the best representation of the magnitude and phase of the impulse defined in CST for the time-domain solver.

5.6. References for Chapter 5

- [1] M. Kahrs, "*50 Years of RF and Microwave Sampling*", IEEE Trans. On Microwave Theory and Techniques, Vol 51, No 6, June 2003, pp 1787 – 1805
- [2] P.D. Hale, C.M. Wangm. D.F. Williams, K.A. Remley and J. Wepman, "*Compensation of Random and Systematic Timing Errors in Sampling Oscilloscopes*", IEEE Trans. Instrum. Meas., Vol 55, pp 2146 – 2154, Dec 2006
- [3] W.B. Mitchell, "*Avalanche transistors give fast pulse of high current and high voltage*", Electronic design, Vol 6, pp 202 – 209, March 1968

Chapter 6 : Material and Field Probes: modelling and measurements

6.1. Introduction

In this chapter, the final modelling of material and field probes (Mprobe and Fprobe respectively) will be discussed in detail. The open-ended SMA Mprobe was used for the characterisation of materials as discussed in Chapter 2. The Fprobe was a means to indirectly observe the common mode (CM) current mentioned in the study by Reader et al.([5] in Chapter 2).

The original intention of this project was to use the current probe (CP) (Chapter 4) to measure the current on the outside of the Mprobe and connecting cable. However, due to the intrusive effect of the CP on the fields formed around the cable, the required measurement sensitivity could not be met.

The method proposed, which still allows the CM effect to be characterised, involved the observation of the E-fields formed around the Mprobe. If the measured results and CST simulations agreed, the current predictions from CST could be directly used in lieu of measurements, as measurements could potentially disrupt the fields around the Mprobe.

The Fprobe was a semi-rigid cable with the centre conductor exposed for a certain length. The choice of this length will be discussed in greater detail in this chapter. In the final measurements, the Fprobe was used for both the frequency-(FD) and time-domain (TD) measurements.

6.2. Modelling

The modelling was done using the model method described in section 3.2.2. In the following section, the individual components of the final model will be discussed. The model consisted of the Mprobe, a shield like structure around the Mprobe and the Fprobe, which was fed through the shield.

6.2.1. Mprobe

The Mprobe consisted of a SMA panel mount with the centre conductor cut flush with the connector, a male connector and the feeding cable. All the dimensions used for the cables and connectors were from the Suhner catalogue. The dimensions of the cable were kept the same as that of the connectors. This simplified the model, as the physical transition from the cable to the connector did not need to be modelled.

Figure 6-1 shows the CST model created for the Mprobe. Because the whole model was created parametrically, the length for the cable in both the model and the physical structure, was chosen such that the length of the cavity was exactly 200 mm.

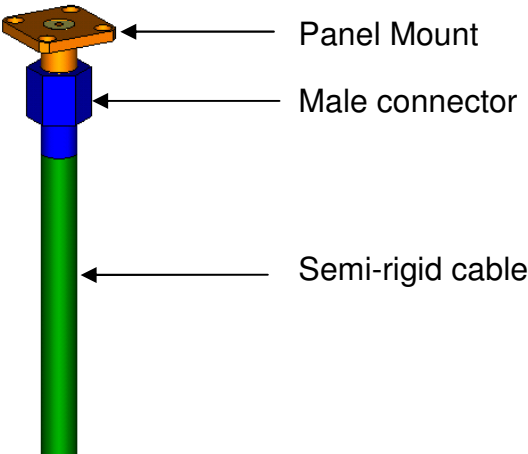


Figure 6-1: The Mprobe with connector and cable as modelled in CST

Figure 6-2 shows how the Mprobe model was created from the lists of variables seen in Table 6-1 (section 6.2.3). The hood of the male connector was

modelled as a hexagon. This was created by using a block (MxN size) and rotating it by $\pm 60^\circ$.

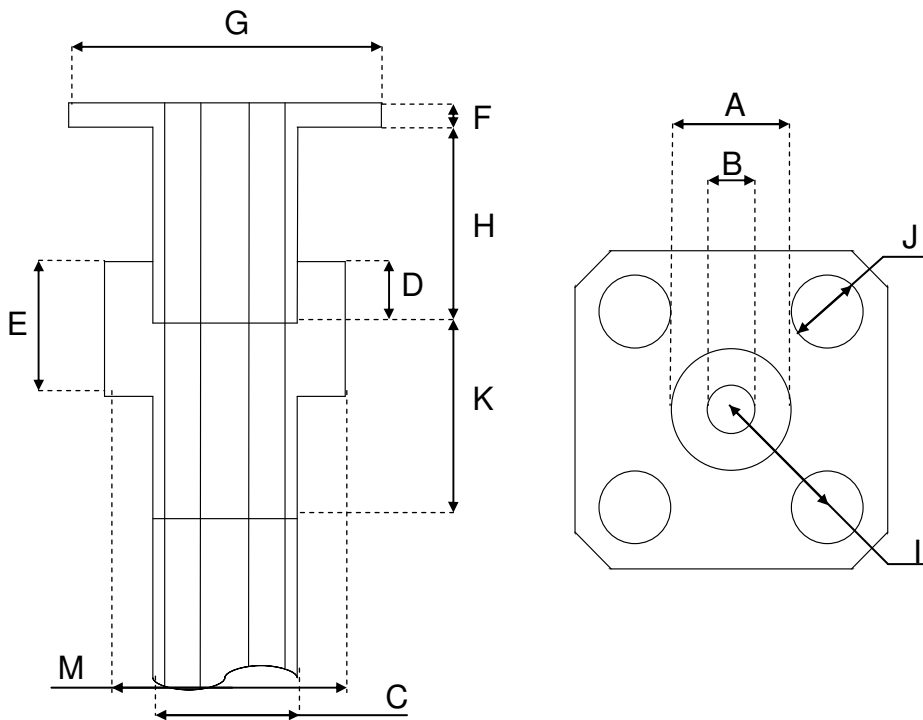


Figure 6-2: A schematic diagram of the relation of the components and the variables listed in Table 6-1

6.2.2. Shield and the Field Probe

The shield structure formed a cavity when placed around the Mprobe. For a shield around a material probe to be a viable option, it must have as little impact on the phase of S_{11} as possible. The phase was a critical parameter in the extraction of the real part of the permittivity of the material under test's (M.U.T.). Referring back to Figure 3-3, and sweeping the variables D_s , S , U and T , the effects of these dimensions could be observed. This investigation can be divided into three subdivisions:

- Width Sweep (D_s)
- Height Sweep ($S + \text{ShieldHeight}$)
- RF Choke (size $\{T\}$ and position $\{U\}$)

In this investigation, the MProbe was simulated without the shield and S_{11} was stored as the reference (S_R) data. Sweeping individual parameters (S, D_s , T and U), the S_{11} from the simulations could then be compared to S_R . The difference between the magnitude and phase for each parameter could then be determined.

Appendix F contains the results for the height and width sweep. Examining the results for the phase, it is seen that the phase differs by a maximum of a -0.88 of a degree around 2.7 GHz. The linear magnitude has a worst-case scenario difference of 0.0045 (or -47 dB). Considering the results from the sweeps, a diameter of 80 mm was chosen for the shield and the height, such that it was flush with the Mprobe.

6.2.3. Final model

For the model (Figure 6-3) to be complete, the position of the Fprobe still needs to be calculated. Figure 6-4 shows the Fprobe as it is simulated in CST. The positions of the holes in the shield through which the FProbe was inserted, were picked using the E-field plots from CST at 1 GHz. Figure 6-5 shows the plot of the E-field, with the positions chosen such that one was at a field maximum (P4), one was at minimum (P2) and another (P1) was close to the Mprobe itself.

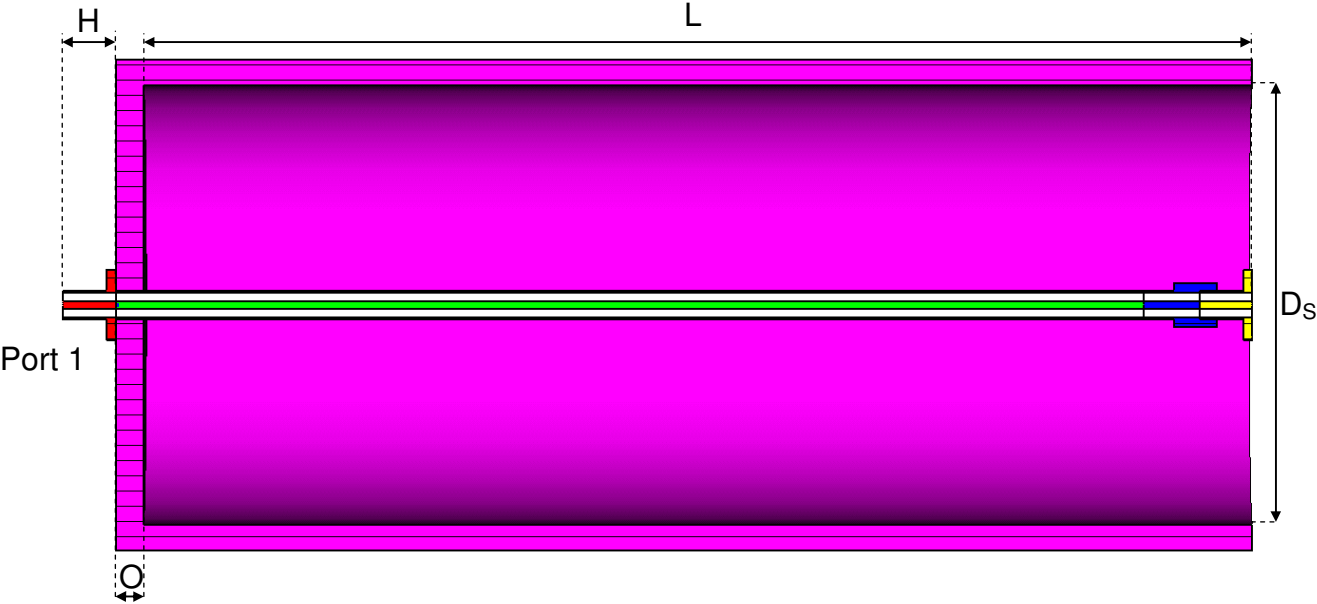


Figure 6-3: The shield structure with the variable relations needed for the CST model

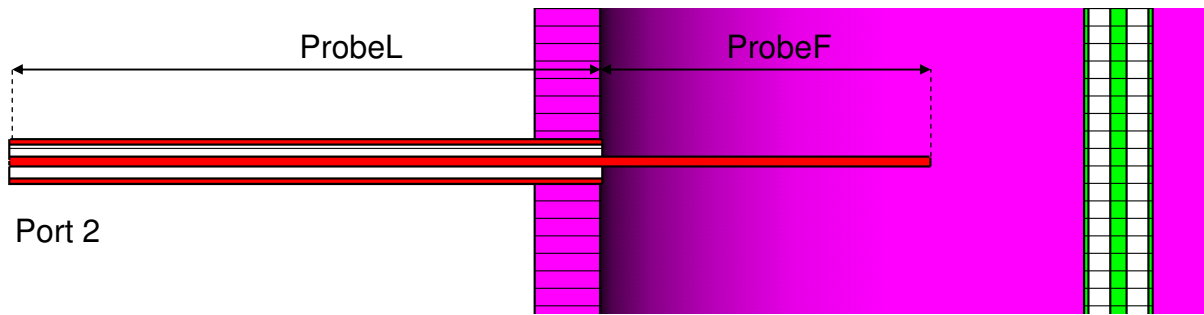


Figure 6-4: The CST model for the Fprobe as well as the variables used for this model

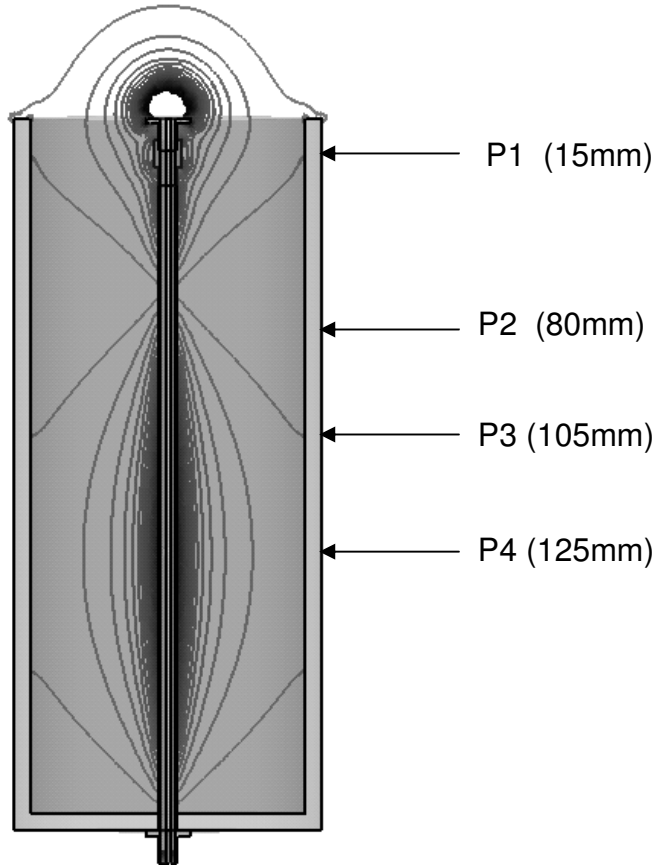


Figure 6-5: The E-Field lines inside the shield at 1 GHz

Figure 6-6 shows a perspective view of the final model simulated in CST, where ProbeH is the height of the Fprobe for each of the positions. Table 6-1 lists all the variables and their values. The CST model was simulated over a bandwidth of 3 GHz using the time-domain solver. For this simulation, a full licence was used which removes the mesh cell restriction of the educational licence. The model had around 2.3 million mesh cells and took around 20 minutes to simulate to an accuracy of -40 dB. Figure 6-7 shows a photograph of the final physically constructed Mprobe with shield structure and Fprobe.

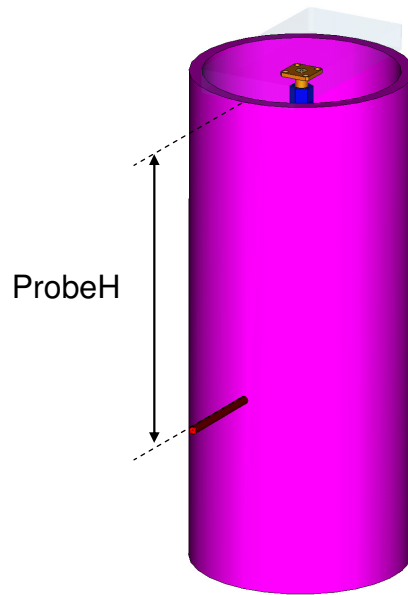


Figure 6-6: The final CST model for the Mprobe, shield and Fprobe. In this figure the Fprobe is at position 4 (P4) where ProbeH = 125 mm

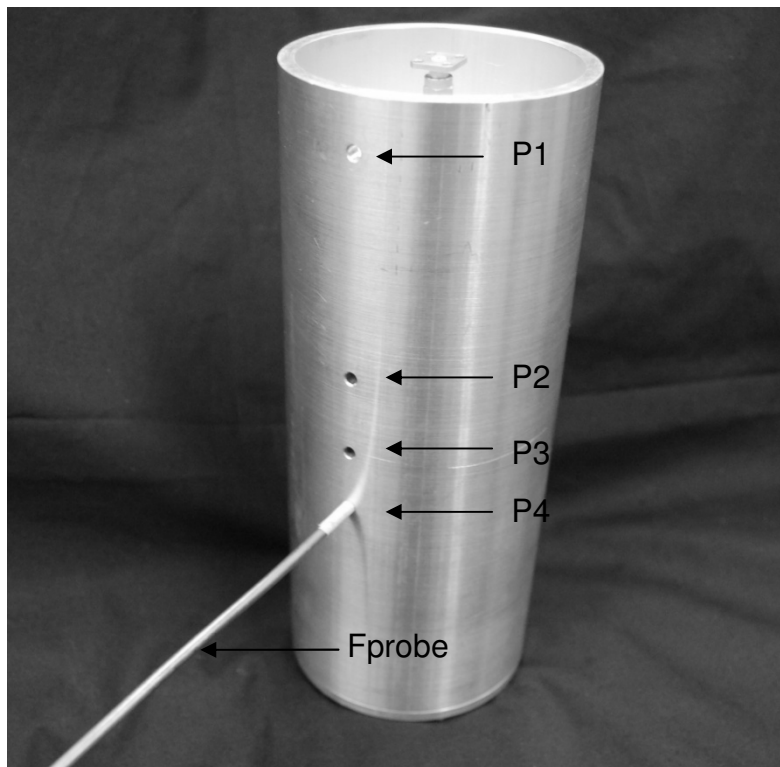


Figure 6-7: The physical constructed Mprobe with shield structure. The four measuring positions are clearly visible. The Fprobe is at position P4

Table 6-1: Dimentions for the final model of the Mprobe, shield enclosure and Fprobe

Variable	Value (mm)	Description
A	4.6	Outer diameter of the dielectric
B	1.2	Diameter of the centre conductor
C	5.3	Outer diameter of the conductor
D	3.0	Depth of the male connectors dielectric face
E	7.6	Male connector hood
F	1.6	Thickness of the panel mount flange
G	12.7	Size of the panel mount face
H	9.5	Length of the panel mount without the flange
I	6.5	Position of the screw holes
J	2.6	Diameter of the screw holes
K	10.1	Length of the male connector
L	200	Electrical path length from the bottom of the shield cavity to the face plane of the panel mount
M	8.0	Width of the male connector hood
N	4.6	Length of the hexagonal section
ShieldHeight	L	Height of the shield structure around the Mprobe
ShieldThickness	5	Thickness of the cylinder
Ds	80	Cavity diameter (inside of the shield)
ProbeA	2.6	Outer diameter of the dielectric for the probe
ProbeB	0.7	Radius of the centre conductor for the probe
ProbeC	3.4	Outer radius of the conductor for the probe
ProbeF	25	Length of the centre conductor inside the shield structure
ProbeH	15, 80, 105 and 125	Position of the Fprobe along the shield side (P1, P2, P3 and P4)
ProbeL	40	Length of the Fprobe outside the shield

6.3. Experimental setup and measurements

For the FD measurements, the S_{21} from the VNA was directly compared to the simulated results. For the TD evaluations, the input and output were recorded at the same time. The conclusion in section 6.5 will discuss the comparison between the FD measured and TD computed S_{21} results in greater detail.

6.3.1. Frequency-domain measurements using the VNA

For the FD measurements, the experiments were set up as illustrated in Figure 6-9. Two VNAs were used for the measurements, an Agilent 8753 and an Agilent 8510. Each of these VNAs had their own distinct advantages. The 8753 allowed greater noise floor (NF) reduction as the IF of the VNA could be changed.

Figure 6-8 illustrates the difference in the noise floor for a standard calibration and a low NF calibration.

In contrast, the 8510 allowed a calibrated low-pass TD measurement to be performed. TD measurements performed on a VNA are still regarded as a FD measurement, because the TD data is computed using the FD results. The VNA selects those frequencies within the frequency range with a harmonic dependency and then the data is transformed from the FD results where real data can be displayed in the TD.

For the FD measurements, reducing the NF is important in order to increase the dynamic range of the measurement. Table 6-2 shows some of the techniques used to reduce the NF for both VNAs. These were applied both before and during the calibration process.

Increasing the dynamic range allowed a shorter Fprobe to be used in the FD. This reduced the field area sampled inside the shield and increased measurement sensitivity. The TD measurements done on the 8510 used a 5 mm probe, but the results indicated that a longer (25 mm) probe was needed for the TD measurements on the sampling scope (the results are shown in Appendix G). The results from the TD on the VNA only influenced the choice of length for the Fprobe.

Table 6-2: Calibration improvements to decrease the noise floor

Technique	Implementation	Improvement
Isolation	Using two matched loads in the calibration for the isolation correction, the improvement depends on the quality of loads.	20 – 30 dB
Averaging	A higher averaging factor averages the amount of noise measured by the system N times	\sqrt{N}
IF Bandwidth (8753 Only)	Reducing the IF bandwidth increases measurement time but reduces the bandwidth over which the VNA works when measuring the a specific frequency	Reducing IF by a factor of 10 Decreases the noise floor by 10 dB
Power	Adding more power increases the signal to noise ratio on the VNA	1:1

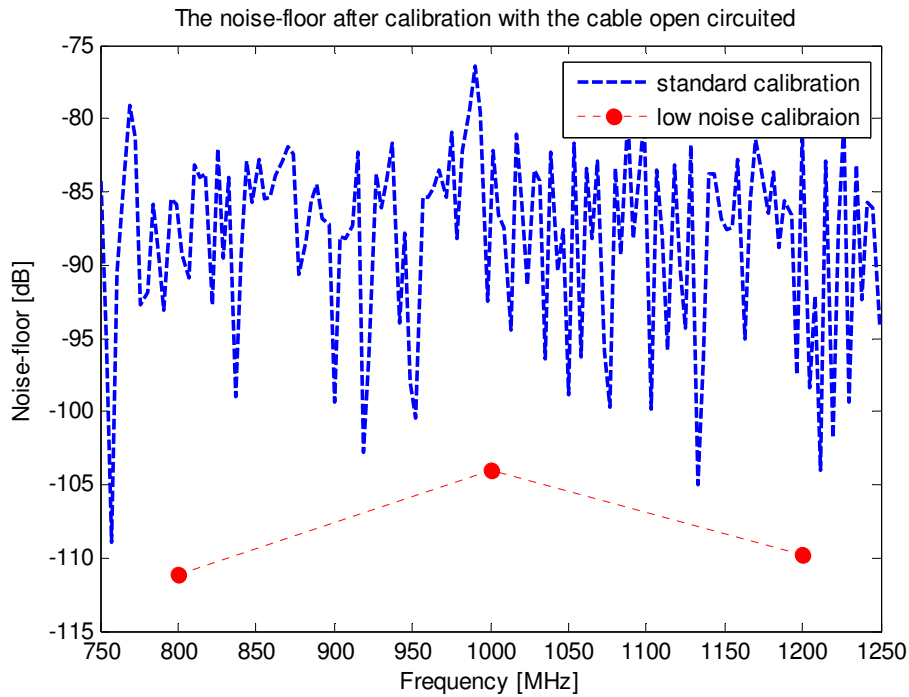


Figure 6-8: The noise floor for a standard and a low noise calibration. This measurement was carried out on the Agilent 8753 VNA using the VNA setup in Table 6-4 measurement # 1

6.3.1.1. Frequency-domain setup for the VNA

All three measurements used the same basic connection (Figure 6-9) with one port of the VNA connected to the Mprobe and the other port connected to the Fprobe.

Figure 6-10 (a. and b.) shows the connection to the 8510 and 8753, respectively. Both connections used two highly phase-stable cables. This ensured that the calibration plane was not affected by handling the cables when moving the Fprobe between the four positions.

6.3.1.2. Frequency-domain measurements

Table 6-3 show the three measurements and the objective of each, while Table 6-4 outlines the setup for each measurement. The results of the first two measurements are shown in Appendix G. These measurements only demonstrated that a longer Fprobe was required for TD measurements in section 6.3.2. The third measurement used the final Fprobe of 25mm.

All the measurements were conducted on the same method, with the NF recorded after calibration. After the NF measurement, the Fprobe was placed at each of the four measuring positions and the data for each position was recorded.

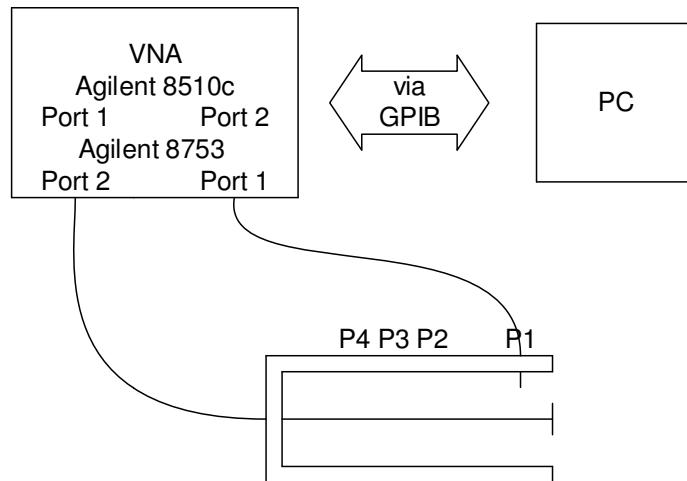


Figure 6-9: Setup for the experiment using the VNA



Figure 6-10: The physical setup for the two VNAs used a. Agilent 8510 and b. Agilent 8753. In both setups the same highly phase stable cables from Suhner were used

Table 6-3: The three individual measurements performed on the VNAs and the objective for each experiment

Measurement	VNA	Objective
1	8753	To calibrate for as low a noise floor as possible. Reduce the length of the Fprobe for the TD measurement on the VNA, the measurement was centred around 1 GHz and was only performed at P4 which has the strongest field strength
2	8510	Set the VNA into TD low pass mode and calibrate over the whole frequency range (3 GHz) The calibrated VNA will produce reliable signal levels
3	8753	Final Fprobe measurements which can be compared to the TD results measured on the sampling scope

Table 6-4: The setup of VNA for each measurement

Measurement	Frequency range [MHz]	Number of Points	Averaging	IF [Hz]	Power [dB _m]
1	800 – 1200	3	100	10	10
2	45 – 3000	51	2046	NA	15
3	0.300 - 3000	201	16	1000	0

6.3.1.3. Results for the VNA measurements for the final field probe

Figure 6-11 shows an overlay of the results from the CST simulation and the results measured on the VNA for the Fprobe at P4. (The results for the remaining three positions can be found in Appendix G.) The “ringing” observed on the CST data was related to the simulation time.

Four peaks are visible in the results in Figure 6-11., The approximated frequencies of each peak are listed in Table 6-5. These peaks were affected by the length of the Mprobe. The length of the Mprobe was 200mm, from the face of the Mprobe to the bottom of the cavity. This represents a $\frac{\lambda}{4}$ monopole at 375 MHz. The first peak, at 330 MHz, was close to the frequency of the monopole. The frequencies of the remaining peaks (2, 3 and 4) were close to the odd (3,5 and 7) harmonics of 330 MHz.

Table 6-5: The four peaks seen in the measured results with their approximated frequencies

Peak	1	2	3	4
f [MHz] (approximated)	330	980	1670	2380

The phase in Figure 6-11 was linearised by subtracting a constant phase over the frequency band. This result from the VNA could now be compared to the TD measurements on the sampling scope. For the sampling scope, the S_{21} could not be directly measured and therefore had to be mathematically created from the reference input impulse and outputs.

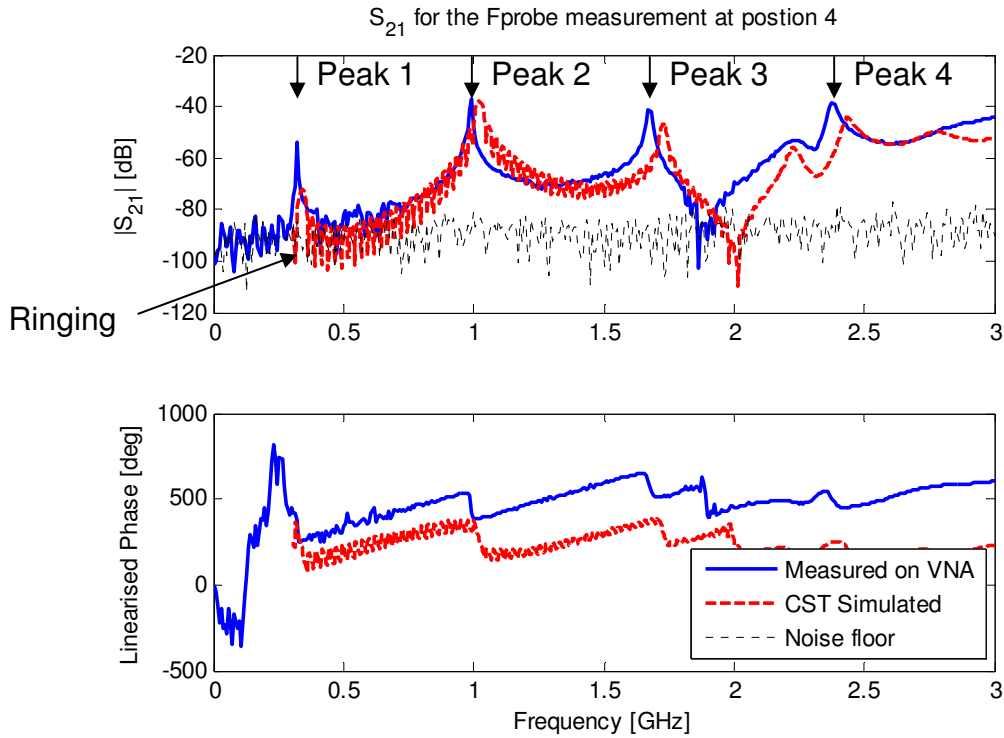


Figure 6-11: Measured S_{21} for the Fprobe using the VNA when the Fprobe is placed at P4. The measurement also illustrates the noise floor when the measurement was made

6.3.2. Time-domain measurements on the Agilent Sampling oscilloscope

The setup in Figure 6-12 illustrates the same basic setup used for the TBC experiment in Chapter 5. Both the input pulse and the output from the Fprobe was measured. From the TD data, the complex Fourier coefficients were calculated. Using the frequency data an S_{21} [1] could be calculated using:

$$S_{21} = \frac{V_{-}(f)}{V_{+}(f)} \quad (6.1)$$

Where $V_{-}(f)$ and $V_{+}(f)$ are the complex frequency spectrum of the output and the input signals, respectively. This calculated S_{21} was compared to the calibrated measurement from the VNA.

6.3.2.1. Time-domain setup on the Agilent sampling oscilloscope

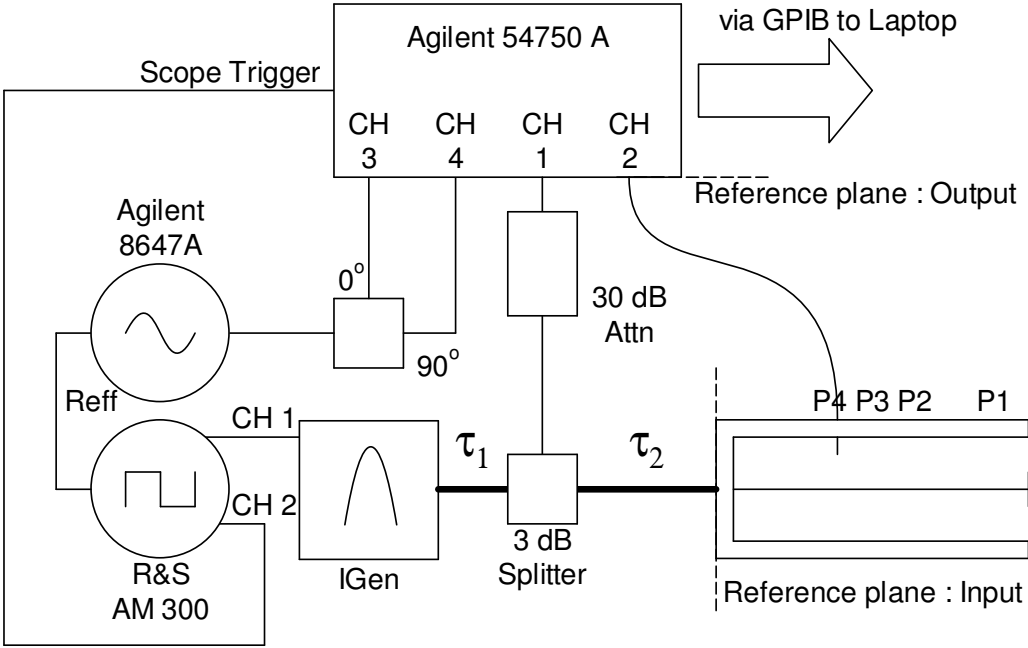


Figure 6-12: Setup used for the experiment using the sampling oscilloscope

This setup used the TBC setup, from Figure 5-9, as a template. Figure 6-13 shows a photograph of the physical setup. Here the output of the impulse generator (IGen) was connected to a 3 dB splitter. The splitter from Mini-Circuits (model number ZFSC-2-2500+) split the impulse between the input of the sampling scope and the Mprobe.

Because of the open circuit of the Mprobe, the impulse was reflected. Therefore, the cables τ_1 and τ_2 had to be of sufficient length to provide the necessary time delays to ensure that the reflections did not contaminate the measurements. Table 6-6 shows the cable lengths used in this measurements as well as the time delay associated with each cable, Figure 6-14 b. shows the physical cables.

Table 6-6: The length and time delays of the cables used in the final time-domain measurements

Cable	Length (m)	Time delay (ns)
τ_1	7	30
τ_2	4	17

An Agilent 8647A signal generator was set to a frequency 100 MHz and output amplitude of 0 dB_m, to provide the two reference signals. The two generators were synchronised using the same procedure as previously discussed in section 5.4.2. The R&S AM 300 was set to a low jitter square wave at a frequency of 50 MHz and both channels were set to output amplitude of 1.4 V_{p-p}. For the IGen, the output with the SRD was used. The results in Chapter 5 demonstrated that the SRD output gave the best frequency spectrum over the 3 GHz band.

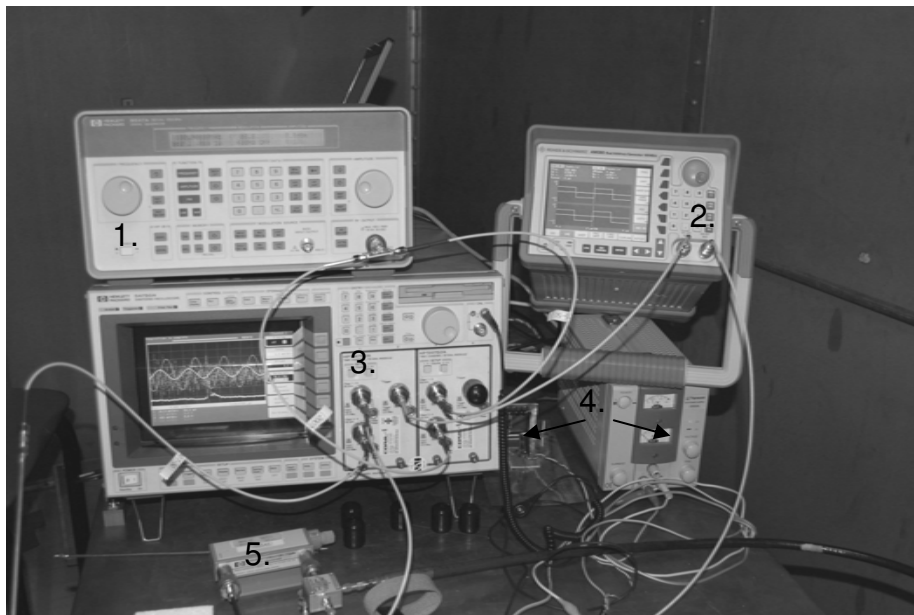


Figure 6-13: The physical setup of the TD measurement, this shows all the components used.

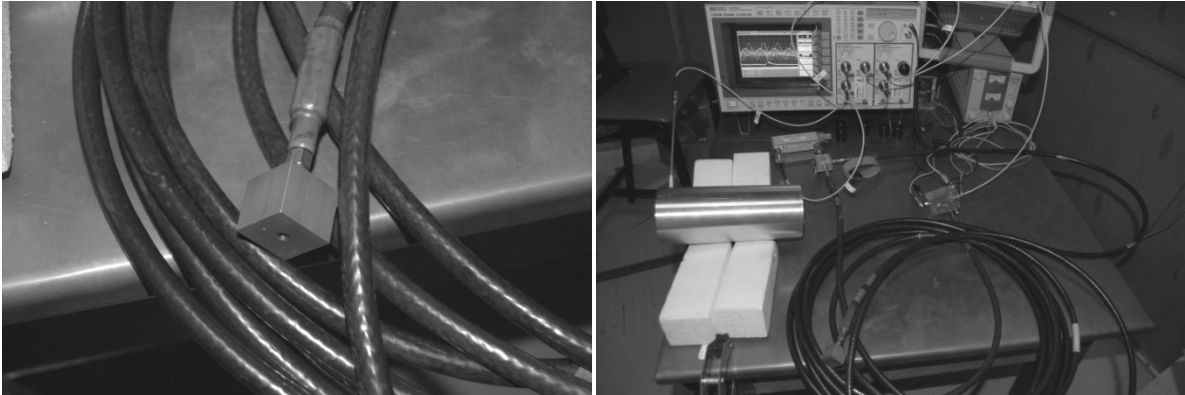
1. Agilent 8647A generator
2. R&S AM 300
3. Agilent 54750 Sampling Scope
4. Power sources for the Impulse generator
5. Splitter and Attenuator

6.3.2.2. Measurements

As before, the sampling scope was controlled over the GPIB interface using a laptop computer within a MATLAB environment. All four channels were measured simultaneously. The scope was stopped while the data from all four channels was collected by a MATLAB function on the computer.

The collected data was stored in files for later post processing. For the calculation of S_{21} a reliable input reference pulse was required. This impulse was measured using a short circuit at the end of cable τ_2 (“reference plane: input” in Figure 6-12) and inverted for the data processing. Figure 6-14 a. illustrates the setup for the measurement of the two standards (the open standard is shown, but only the

short was used for the final processing). The open standard had too many losses from the radiation at the open circuit, while the short-circuited impulse retained all the pulse magnitude information.



a.

b.

Figure 6-14: The setup configuration where the standards for the reference impulse were measured, a. shows the connected open standard and b. shows the delay cables used to prevent the measurement of unwanted reflected pulses.

6.3.2.3. Results

For this section, only the measurements for the Fprobe at P4 will be discussed. The measurements for the other positions follow the same procedure and those results are in Appendix H. Figure 6-15 shows the measurement when the Fprobe was placed at P4.

Figure 6-16 shows the normalised output of the Fprobe compared to the output signal from the CST simulation. The average amplitude of the CST output pulse was on the scale of μV whereas the measured output level was in mV . Therefore, the results were normalised to enable comparison of the TD form of the simulated and measured output pulses.

Figure 6-17 compares the spectra of the CST and the Fprobe signals when the signals have not been normalised. The results show that the spectra of the measured signals have a similar shape to the simulated results, but differ in magnitude.

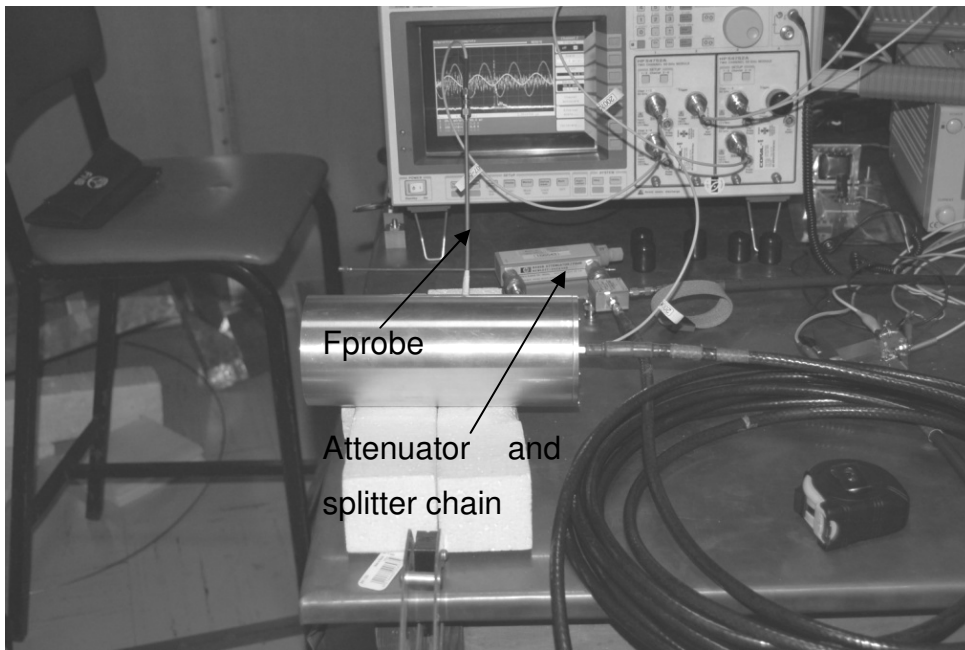


Figure 6-15: The Fprobe was placed at P4 for the measurement discussed in this section

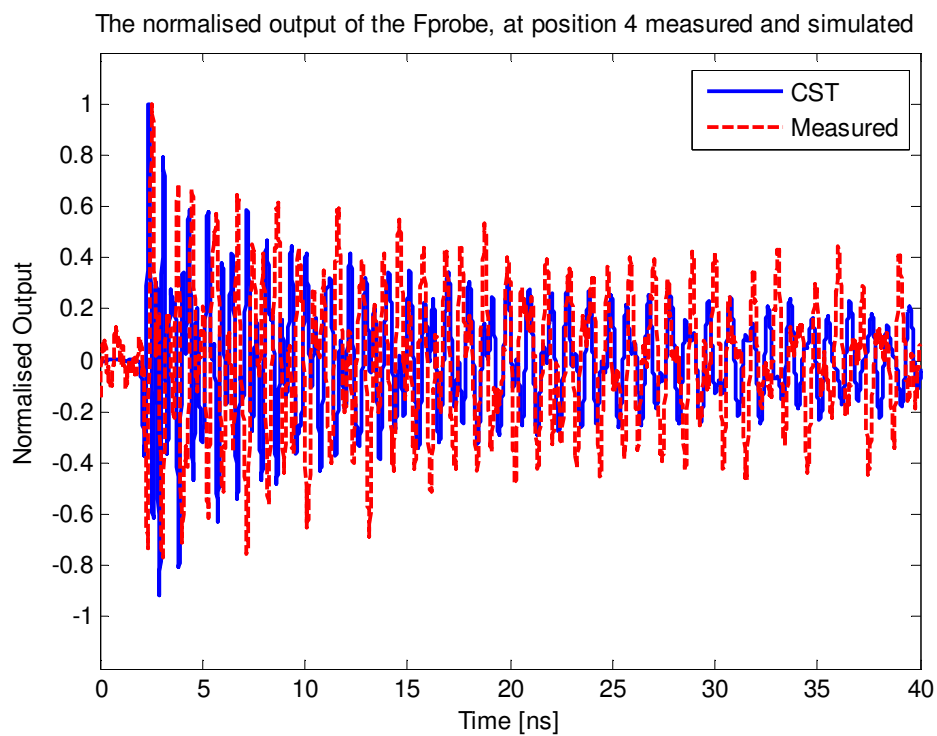


Figure 6-16: The normalised output for both the measured and simulated results when the Fprobe is placed at P4

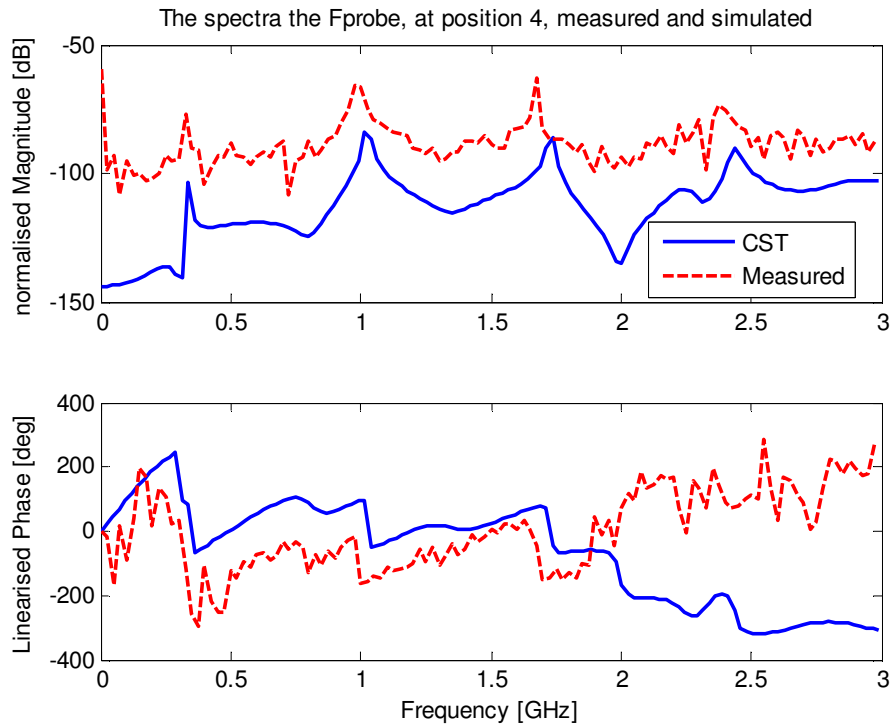


Figure 6-17: The spectra of the Fprobe output and the output of the CST simulation. The time signal was not normalised in this case. From the magnitude plots, the difference in amplitude between the time signals can be seen

For the calculation of the S_{21} the reflected reference impulse must be mathematically corrected to represent the impulse at the input reference plane in Figure 6-12:

$$V_{in}(f) = \frac{V_r(f)}{T_{1-att}T_{2-cable}} \quad (6.2)$$

Where $V_r(f)$ is the complex Fourier coefficients of the reference impulse measured when the short standard is connected. T_{1-att} and $T_{2-cable}$ are computed from the VNA measured transmission coefficient of the attenuator-splitter chain and cable, respectively. From T_{1-att} and $T_{2-cable}$ the loss and phase of the cable and attenuator can be removed. $V_{in}(f)$ provides the complex Fourier coefficients for the input impulse.

The output of the Fprobe, for a single measurement, was used for output and transformed $\{V_{out}(f)\}$ at the output reference plane shown in Figure 6-12. The final S_{21} was calculated using (6.3) and the results were then compared to the S_{21} measured by the VNA for each of the positions.

$$S_{21} = T_{1-ant} T_{2-cable} \frac{V_{out}(f)}{V_r(f)} \quad (6.3)$$

Figure 6-18 shows the two S_{21} results plotted against the VNA measured results. From the magnitude of the calculated waveform, it was noticed that the shape of the waveform followed that of the VNA results. The phase results from Figure 6-18 appeared to differ but followed the same rate of phase change for P4.

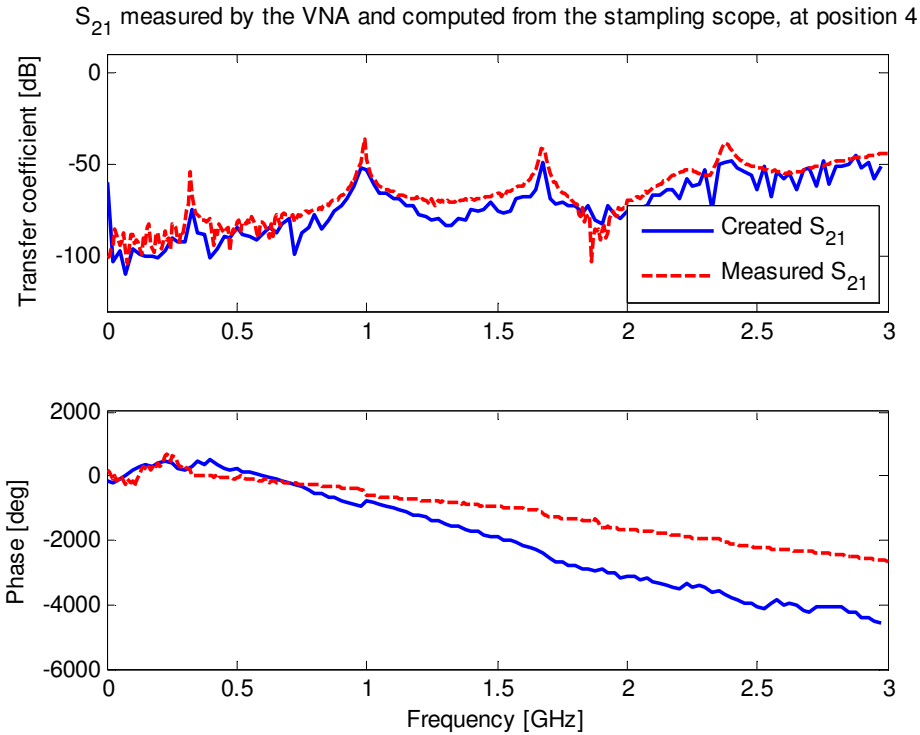


Figure 6-18: The computed S_{21} compared to the measured S_{21} from the VNA when the Fprobe was placed at P4

6.4. Conclusion

Figure 6-19 shows the magnitude results for the calculated, measured and simulated S_{21} for the Fprobe at P4. Appendix I contains the final results for the remaining three positions.

Overall, the experiment was successful. The TD results followed the same trend as the FD results. However, this measurement was never considered as a method to measure the phase accurately, the magnitude results were still considered to be within acceptable limits. The magnitude differences of the TD could be

attributed to either cable losses or the calculation procedure used for S_{21} . These differences may also be attributable to systematic errors in the measurement setup.

The calibration with a VNA corrected for all 12 systematic errors in a 2-port measurement [2]. For the TD measurement, the reference input pulse was a shorted impulse at the end of cable τ_2 . Figure 6-20 shows the three errors associated with the connection of a measurement device to a device under test (D.U.T.), in this case the Mprobe.

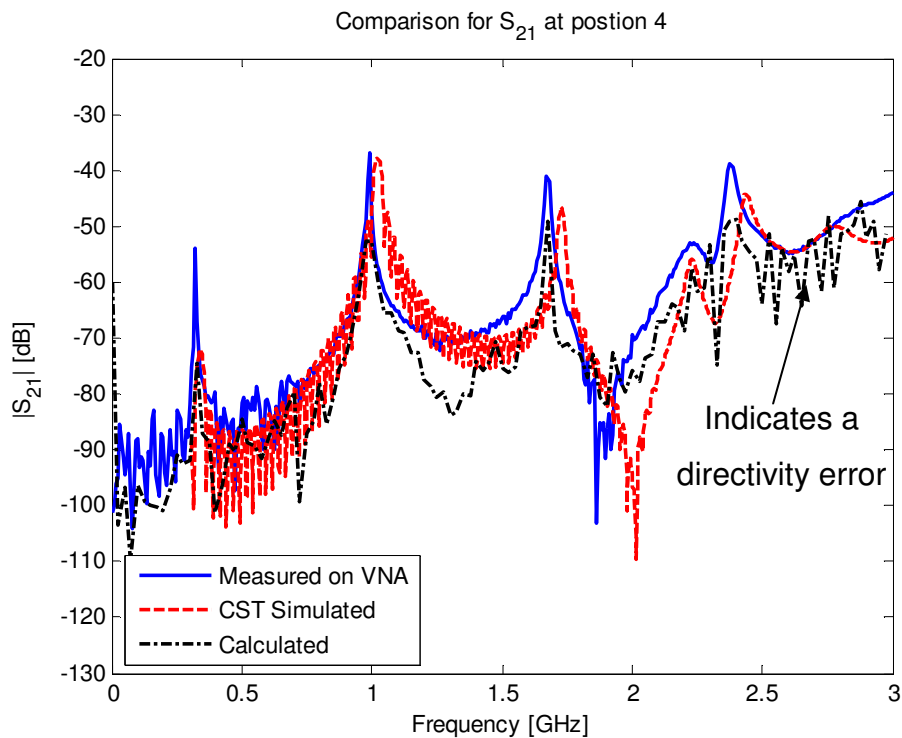


Figure 6-19: The comparison of the measured and calculated S_{21} against the CST simulated results

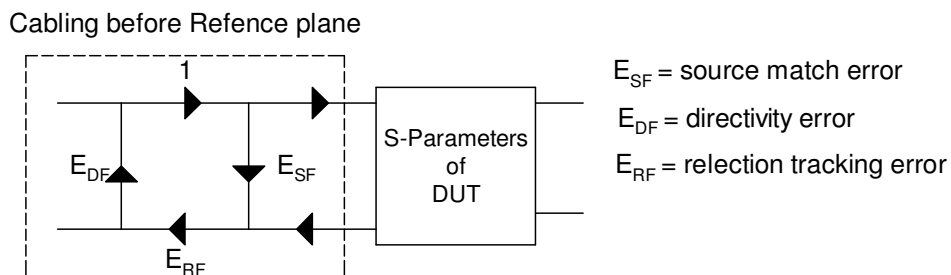


Figure 6-20: Systematic errors in measurements associated with the cabling of a device under test

The relative calibration performed for the TD measurement corrected for the reflection tracking error (E_{RF}) and to a lesser extent, the source match error (E_{SF}).

The directivity error (E_{DF}) is visible from the calculated in Figure 6-19. Correcting for a greater number of these errors will improve the measurements.

Another source of error in the measurements was the use of the scope-averaged signal for the output of the Fprobe. The TBC algorithm struggled to correct the data measured at the output of the Fprobe. As a result of this, a unique S_{21} was provided for each output pulse used.

The time length of the output pulse also contributed to the measurement inaccuracies. Practical restrictions in the measurement setup made it difficult to measure the entire ringing effect of the output pulse.

6.5. References for Chapter 6

- [1] D.M. Pozar, "*Microwave Engineering*", third edition, John Wiley & Sons, 2005, pp. 174-179
- [2] P.G. Wiid, "*Investigating cost-effective EMC methods*", MScEng. Thesis, University of Stellenbosch, Stellenbosch, South Africa, 2005, pp 6-8

Chapter 7 : Final conclusion and future recommendations

7.1. Summary of the study

The original intention of the study was to investigate the common mode (CM) current on the outside of the material property probe using the clamp-on current probe (CP). This was done using both computation (CST) and good metrology. From the calibration of the CP, it was seen that the CP was an invasive device and was not sufficiently accurate for the job at hand.

In light of this, an alternative method was implemented. A cylindrical shield structure, placed around the material probe, allowed an electric field probe to observe the fields surrounding the material probe. This investigation allowed both time- and frequency-domain (FD) measurements to be conducted.

The time-domain (TD) measurements required an understanding of sampling oscilloscopes and the systematic errors associated with these devices. Systematic errors, such as time-base errors, were corrected using software such as NIST's time-base correction algorithm. Correcting for these errors ensure that when this data is Fourier transformed these errors does not contaminate the data.

For the final measurement of the material probe, the S_{21} results for the TD, FD and CST simulations were compared. The TD S_{21} was created using a reference input and the output measured at the field probe. These results showed that the TD and FD were within an acceptable range of each other.

The TD had the advantage of a higher signal to noise ratio, but systematic errors such as source mismatch and directivity can result in a loss of accuracy in the measurements.

The confidence in the CST results was confirmed by comparing the simulated results with the FD results, which were considered the most accurate. All CST results were validated through careful experimental measurements for both the material probe and the CP calibration. This allowed the CST simulations to be used in the

case of CM current investigations where an accurate measurement could not be guaranteed.

This study contributed to the understanding of the CM current on the outside of SMA material property probes. This will allow NIST to incorporate the new information regarding the shield structure in their analysis of material properties.

7.2.Future recommendations

The advantage of TD measurements, is that all frequencies can be measured simultaneously. These results also contain valuable physics information such as the resonances and identification of specific features. Due to these advantages, it would be beneficial to improve the TD setup in order to increase the accuracy of the TD results.

One improvement would be to reduce the directivity error contained in the reflected pulse by appropriately selecting cable delays and reference positions.

The CM current flowing on the surface of the material probe can be reduced by decreasing the length of the shield extending down from the face of the material probe, which consequently decreases the length of the cavity between the shield and the probe. This will push the resonances seen in the S_{21} data out of band. Though the CM current is still present, it will not be detected within the 3 GHz bandwidth of interest used for material property measurements. Because the FD results were closely similar to those simulated in CST, it is possible to obtain all the necessary data from the simulation.

Appendix A: Matlab functions for Current probe Calibration

CST Surface Current Import Function

```
function [data] = cst_import(filename,X1,X2,tol,config)
% CST-FUNCTION
% [data] = cst_import(filename,X1,X2,tol,config);
% This function imports cst output files into matlab. CST output files
% are 3D maps of the fields. This function can extract these fields using
% the 3D Cartesian coordinates. This extracts one row out of the 3D map.
%
% tol is the tolerance which the function will look around the given
% coordinates (X1-tol:X1+tol,X2-tol:X2+tol)
%
% config tells the function which coordinate is connected to data,
% 'Z' connects X to X1 and Y to X2 and this will collect all data along
% the Z axis
% 'Y' connects X to X1 and Z to X2 and this will collect all data along
% the Y axis
% 'X' connects Y to X1 and Z to X2 and this will collect all data along
% the X axis
%
% Example:
% A data file contains the H-field data for a conductor at X = 50 mm and
% Z = 40 mm and the conductor is 500 mm long in Y direction. If the
% H-Field 30 mm above the conductor wants to be extracted the command will
% look the following:
% [data] = cst_import(filename,50,40,1,'Y')
% where X1 = the X coordinate and X2 = the Z coordinate
% and the data collected will be all along the Y axis
%
% ver 1.4

%-----
% Jaco Badenhorst
% jbdnhrst@sun.ac.za
%-----
%
%-----

if (nargin < 5 ) , config = 'Z'; end;
if (nargin < 4 ) , tol = 1; end;

j = sqrt(-1);

if strcmp(upper(config) , 'X'),
    a = 1;
    b = 3;
elseif strcmp(upper(config) , 'Y'),
    a = 1;
    b = 3;
elseif strcmp(upper(config) , 'Z'),
    a = 1;
    b = 2;
end;
```

```

fileid = fopen(filename);

deblank(fgetl(fileid));
fgetl(fileid);

cnt = 0;
line = fgetl(fileid);

while 1
    [vector] = sscanf(line, '%f');

    if ((vector(a) < X1+tol)&&(vector(a) > X1-tol))&&((vector(b) <
X2+tol)&&(vector(b) > X2-tol)),
        cnt = cnt + 1;
        data(cnt,1) = vector(1);
        data(cnt,2) = vector(2);
        data(cnt,3) = vector(3);
        data(cnt,4) = vector(4) + j*vector(7);
        data(cnt,5) = vector(5) + j*vector(8);
        data(cnt,6) = vector(6) + j*vector(9);

    end;
    line = fgetl(fileid);
    if ~ischar(line), break, end
end;

```

Main transfer impedance function

```

function [ZtCal, f, T, ProbeVolts, CFdata CFfact ,date] =
emcprobe(Datafile,tol)
% PROBE CALIBRATION FUNCTION
% [ZtCal, f, T, ProbeVolts, CFdata, CFfact] = emcprobe(Datafile,tol)
% Emcprobe imports data from a special excel file that contains all the
% needed constants and data for the calibration of the emco probe using
% the spectrum analyser method
%
% tol = 1 by default if not specified
%
% Outputs :
% ZtCal      - The calibrated transfer impedance.
% f          - frequencies
% T          - Input impedance at each frequency
%            Input voltage
%            Input Current
%            Manufacture specified transfer impedance
% ProbeVolts - Probe output voltage at each measurement point
% CFdata     - raw cst data
% CFfact     - Current form facture
%
%
%
%-----
% Jaco Badenhorst
% jbdnhrst@sun.ac.za
%-----
clc;
if nargin < 2,
    tol = 1 ;
end;

%-----

```

ver 3.0

```

%% Setup
%-----

% Measured data
mdata = xlsread(Datafile,1);
% Setups for the calibration
constants = xlsread(Datafile,2);
% size of the constants matrix
[n m] = size(constants);
% Frequencies used for the calibrations
f = constants(1,1:m);
% Attenuation if any
atten = constants(2,1:m);
% Input power at the terminals of the EPE
Pin = constants(3,1:m);
% Transfer impedance from the datasheets
Ztds = constants(4,1:m);
% System Char Impedance
Z0s = constants(5,1);
% Load Impedance
ZL = constants(6,1);
% Calibration environment's Char Impedance
Z0 = constants(7,1);
% First position of the measuring
StartP = constants(8,1);
% Last measuring position
EndP = constants(9,1);
% Space between positions
SpaceP = constants(10,1);
% X1 for the current form data
X1 = constants(11,1);
% X2 for the current form data
X2 = constants(12,1);
% Direction in which the current is flowing
Dir = constants(13,1);
% Length of the wire/Cable on which the current is flowing
L = constants(14,1);
% Speed of light
C = 299.792e6;
% Measuring points in the bakkie
Pt = (StartP:SpaceP:EndP);

% Date on which the measurements where made
if (m >= 3)&&(n == 15),
    DateM = constants(15,[1 2 3]);
    date = DateM;
end;

disp( ' ');
disp( ' Excel Reading completed')

clear pi constants i;

%-----
%% Theoretical Current calculation
%-----
% Calculates the Input impedance seen by the signal gen
for g = 1:m,
    beta = 2*pi/(C/(f(g)));

```

```

        Zin(g) = Z0*((ZL + i*Z0*tan(beta*L/1000))/(Z0 +
i*ZL*tan(beta*L/1000)));
end;

% Converts the input power from dBm to dB
Pin = Pin - 30 ;

for g = 1:m,
    Vin(g) = sqrt((10^(Pin(g)/10))*Z0s);
end;

% Vth
Vth = Vin*2;

% Calculates the input current for each of the frequencies using the
% information above
for g = 1:m,
    It(g) = Vth(g)/(Z0s +Zin(g));
end;

% the output matrix with the all the theoretical values
T = [ Zin;
      Vin;
      It;
      Ztds];

clear C beta g ;
disp(' Calculations completed')

%-----
%% Theoretical Current calculation
%-----

% Uses the information provided in the excel file
if Dir == 1,
    dircst = 'Z';
    PCST = 3;
elseif Dir == 2
    dircst = 'Y';
    PCST = 2;
elseif Dir == 3
    dircst = 'X';
    PCST = 1;
else
    dircst = 'Y';
    PCST = 2;
end;

% This section of code imports the surface current data from the data file
% saved from CST

clear j;
for A1 = 1:1:m,
    if (f(A1)/1e6 < 1)
        [data] = cst_import(['Hprobe', num2str(1000*f(A1)/1e6), 'k.dsc'], ...
            X1,X2,tol,dircst);
    elseif (f(A1)/1e6 >= 1000)
        [data] = cst_import(['Hprobe', num2str(f(A1)/1e9), 'G.dsc'], ...
            X1,X2,tol,dircst);
    end;
end;

```

```

else
    [data] = cst_import(['Hprobe', num2str(f(A1)/1e6), '.dsc'], ...
        X1, X2, tol, dirbst);
end;
[datapos, Index] = sort(data(find((data(:, PCST)>0)&...
    (data(:, PCST)<L)), PCST));
ky = abs(data(find((data(:, PCST)>0)&...
    (data(:, PCST)<L)), PCST+3));
ky = ky(Index);

for c = 1:1:length(datapos)/12,
    if (c*12+11) <= length(datapos)
        CF = (min(ky((c*12):1:(c*12+11))) ...
            + max(ky((c*12):1:(c*12+11))))/2;
    else
        CF = (min(ky((c*12):1:length(ky))) ...
            + max(ky((c*12):1:length(ky))))/2;
    end;
    gdata(c, 1) = datapos(c*12);
    gdata(c, 2) = CF;
end;
if A1 == 1,
    CFdata = [gdata(3:length(gdata(:, 1)), 1) ...
        gdata(3:length(gdata(:, 1)), 2)];
else
    CFdata = [CFdata gdata(3:length(gdata(:, 1)), 2)];
end;

end;

clear c A1 data ky datapos Index dirbst gdata PCST;
disp(' CST Import completed');
%-----
%% Projects the input current for the form factor
%-----

CFfact(:, 1) = Pt';
for A2 = 1 : m,
    % y = ax + c
    % a = Y2-Y1
    % -----
    % X2-X1
    % c = - aX2 + Y2

    X2 = CFdata(3, 1);
    X1 = CFdata(2, 1);
    Y2 = CFdata(3, A2+1);
    Y1 = CFdata(2, A2+1);
    a = (Y2-Y1)/(X2-X1);
    CFBegin(A2) = Y2 - a*X2;

end;

% This section of code calculates the current using the form factor and the
% theoretical calculated input current

for A3 = 1 : m,
    CFfact(:, A3+1) = interp1(CFdata(1:length(CFdata(:, 1))-3, 1), ...
        CFdata(1:length(CFdata(:, 1))-3, A3+1), Pt')/CFBegin(A3);
    if A3 == 1,

```



```

        ICST = CFfact(:,A3+1)*abs(It(A3));
    else
        ICST = [ICST CFfact(:,A3+1)*abs(It(A3))];
    end;
end;

clear k1 t1 q u pnt A2 A3 tol c cnt CF;
disp(' Form Factor completed')
%-----
%% Transfer Impedance Calculation
%-----

for A1 = 1 : m,
    mdata(:,A1) = mdata(:,A1) + atten(A1) - 30;
    [ZtCall PrVolt1] = CurrentprobeCal(mdata(:,A1),ICST(:,A1),Z0s);
    ZtCal(:,A1) = ZtCall';
    ProbeVolts(:,A1) = PrVolt1';
end;

disp(' Transfer Impedance calculated');
disp(' ');

clear ZtCall PrVolt1 A1
clear atten Pin Ztds Z0s ZL Z0 StartP EndP SpaceP
clear X1 X2 Dir L DateM C Pt n m mdata It Zin Vth Vin points;

```

Appendix B: Smith Chart method

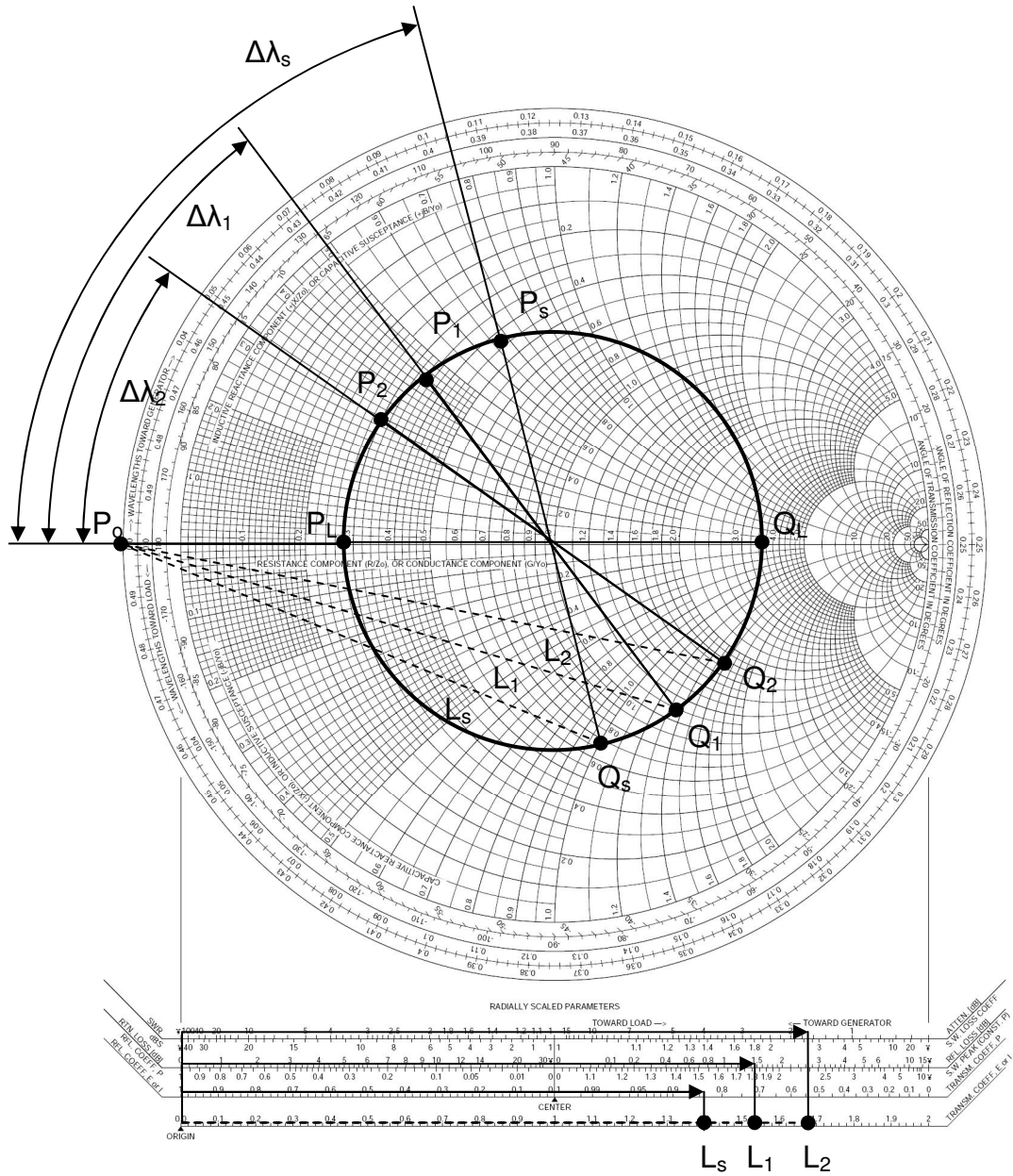


Figure A 1: A smith chart showing the procedure for calculating the standing wave pattern of the voltage and current

1. Plot position of the 50 Ω load (P_L) on the Smith Chart

$$P_L = \frac{50}{Z_{0E}} \quad (\text{A.1})$$

2. Work out the wavelength of the frequency

$$\lambda = \frac{c}{f} \quad (\text{A.2})$$

3. Plot the input (P_s) of the system using the length of the EPE

$$\Delta \lambda_s = \frac{\text{length}}{\lambda} \quad (\text{A.3})$$

4. Plot measuring positions (for example P_1 and P_2) using (A.3) for each position seen from the load.

5. Transpose points through the centre of the Smith Chart (Q_s Q_1 Q_2)

6. Measure physical distances from P_0 to Q_s , Q_1 and Q_2 (L_s L_1 L_2)

7. Normalising L_1 and L_2 to L_s gives the current form factor at position 1 and 2

Appendix C: Probe calibration from Chapter 4

Table A 1: Form factor from the Large EPE over the measured frequencies

Position	f1	f2	f3	f4	F5	6	7	8	9	10	11
155	1.000	1.000	1.000	1.002	1.012	1.012	1.050	1.081	1.122	1.176	1.248
180	1.000	1.000	1.000	1.003	1.013	1.013	1.056	1.091	1.137	1.198	1.280
205	1.000	1.000	1.000	1.004	1.015	1.015	1.062	1.100	1.151	1.219	1.309
230	1.000	1.000	1.000	1.004	1.016	1.016	1.067	1.109	1.164	1.238	1.335
255	1.000	1.000	1.000	1.004	1.017	1.017	1.072	1.116	1.176	1.255	1.360
280	1.000	1.000	1.000	1.004	1.018	1.018	1.076	1.123	1.187	1.270	1.382
305	1.000	1.000	1.000	1.005	1.019	1.019	1.080	1.129	1.196	1.284	1.402
330	1.000	1.000	1.000	1.005	1.020	1.020	1.083	1.135	1.204	1.296	1.419
355	1.000	1.000	1.000	1.005	1.020	1.021	1.086	1.139	1.211	1.307	1.434

Table A 2: Input impedance of the large EPE at each frequency

Frequency [MHz]	Zin [Ω]	
	Real	Imaginary
0.300	50.000	-0.788
0.500	50.001	-1.314
1	50.005	-2.628
10	50.543	-26.369
20	52.219	-53.269
30	55.176	-81.275
40	59.697	-111.044
50	66.251	-143.381
60	75.607	-179.314
70	89.037	-220.211
80	108.718	-267.930

Table A 3: Dimensions of the smaller EPE used in the calibration experiments.

Variable	Description	Value [mm]
H	Height of the EPE	200
L	Length of the EPE	60
W	Width of the EPE	200
R1	Radius of the hole in the plate for the connector	2.65
Rc	Radius of the Conductor in used in the EPE	1
Wc	Width-Position of the conductor	125
Hc	Height-Position of the conductor	50
d	Thickness of the plates	0.2
SL	SMA: connector's length	9.3
SR1	SMA: Outer connector radius	2.45
SR2	SMA: Inner connector radius	2.05
SR3	SMA: Conductor radius	0.475
SW	SMA: Width	12.7
Sd	SMA: Thickness of the mounting	1.6

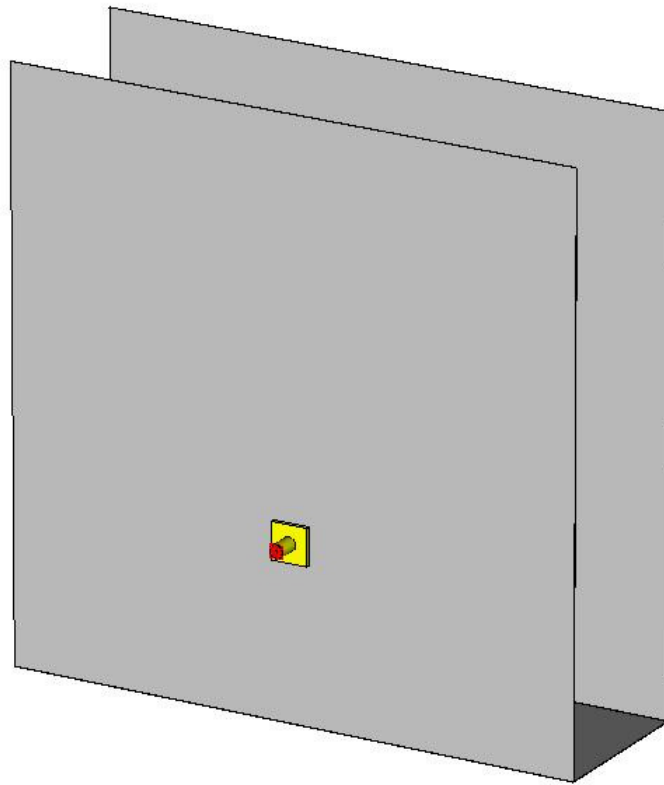


Figure A 2: CST model of the smaller EPE

Table A 4: The Calibration data for the smaller EPE used in the SA measurements, Chain 1 is the input power and Chain 2 the attenuation in the probe path

Frequency [MHz]	Chain1[dB _m]	Chain2[dB]	Frequency [MHz]	Chain1[dB _m]	Chain2[dB]
0.30	9.280	-10.574	70.00	9.363	-10.700
0.50	9.399	-10.563	80.00	9.320	-10.712
1.00	9.477	-10.569	90.00	9.275	-10.760
10.00	9.442	-10.588	100.00	9.278	-10.750
20.00	9.426	-10.583	200.00	9.174	-10.869
30.00	9.390	-10.612	300.00	9.107	-10.952
40.00	9.339	-10.648	400.00	9.031	-11.061
50.00	9.376	-10.673	500.00	8.916	-11.080
60.00	9.353	-10.725			

Table A 5: Input impedance of the small EPE at each frequency

Frequency [MHz]	Zin [Ω]		Frequency [MHz]	Zin [Ω]	
	Real	Imaginary		Real	Imaginary
0.30	50.000	0.088	70.00	50.373	20.669
0.50	50.000	0.147	80.00	50.488	23.638
1.00	50.000	0.295	90.00	50.619	26.614
10.00	50.008	2.946	100.00	50.765	29.597
20.00	50.030	5.893	200.00	53.154	60.029
30.00	50.068	8.842	300.00	57.473	92.221
40.00	50.121	11.793	400.00	64.322	127.289
50.00	50.190	14.747	500.00	74.788	166.681
60.00	50.274	17.706			

Table A 6: Form factor for the smaller EPE

Frequency [MHz]	Form factor	Frequency [MHz]	Form factor
0.30	0.995	70.00	0.997
0.50	0.995	80.00	0.998
1.00	0.995	90.00	0.999
10.00	0.995	100.00	1.000
20.00	0.995	200.00	1.015
30.00	0.995	300.00	1.041
40.00	0.996	400.00	1.080
50.00	0.996	500.00	1.136
60.00	0.997		

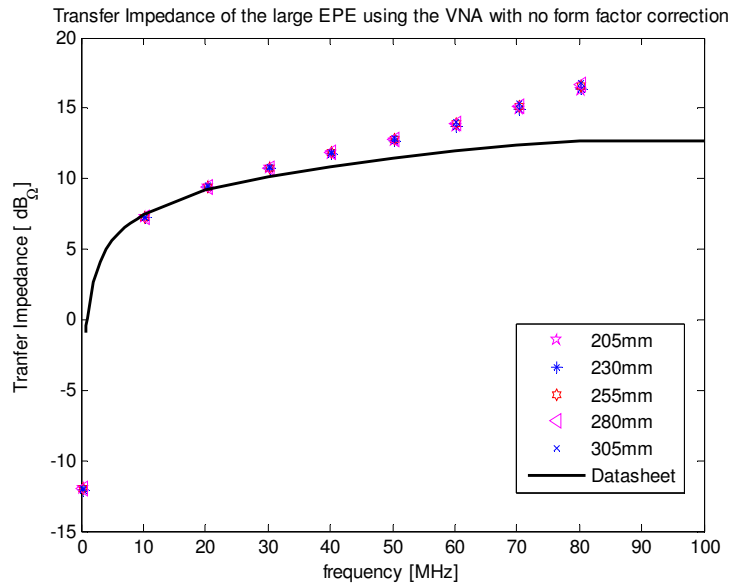


Figure A 3: The transfer impedance of the large EPE when the form factor correction is left out, compared against Figure A 4 the difference is visible

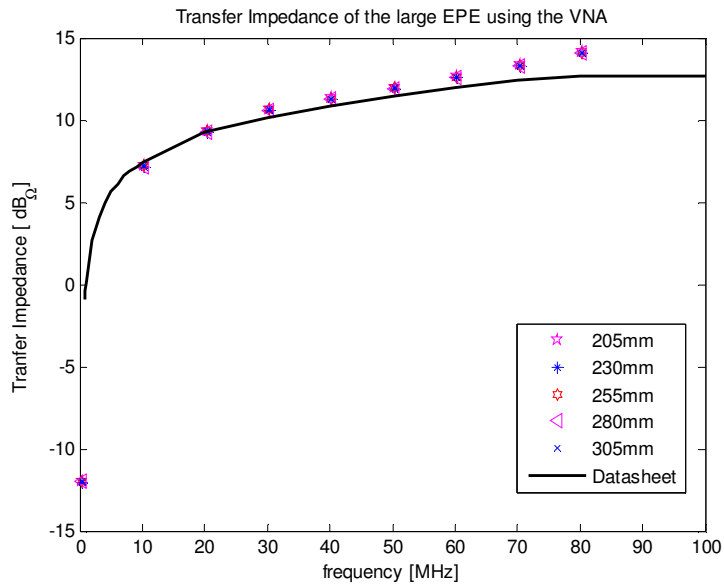


Figure A 4: The same results shown in Figure 4-13 compared against Figure A 3 the effect of form factor correction is noticeable

Appendix D: Matlab code for the TBC data from Chapter 5

This code creates the files required for TBC post processing

```
% TBC File creation
% Jaco Badenhorst
% 28th June 2007

%% Startup
clear all; % Clear workspace
close all; % Close all graphs
clc; % Clears command window
filePick = 2; % Picks the correct data file
% Pick Datafile

if filePick == 1,
% Impulse without SRD
    datafile = '100_single_Pulses.mat'; % 27th June 2007 ns/V =
20.654
    date = '27-06-07'; % date of the measurement
    comment = ''; % Optional
elseif filePick == 2,
% Impulse with SRD
    datafile = '100_single_Pulses_SRD.mat'; % 27th June 2007 ns/V = 27
    date = '27-06-07'; % date of the measurement
    comment = 'SRD'; % Optional
end;

%% Load the workspace data file from the current active directory
load(datafile);

% Generates the time scale from the information recovered from the
% scope while the measurements were performed
% RScale is the scale/div for the time-base of the scope and N is
% number of data points
time = (RScale*10/N:(RScale*10/N):RScale*10)';

%% File Generation

% It is recommended the file are created in a different directory to stop
% creating chaos in the current directory
cd TBC;
path = cd; % The path necessary for file
creation
for a = 1 : Nm, % Nm is the amount of waveforms
recorded
    % Creates the file with the following fields
    % data[comment]_[date]_#.dat
    % the comment could be used for indicating differences like SRD or no
    % SRD
    fullfilename =
fullfile(path, ['data', comment, '_', date, '_', num2str(a), '.dat']);
```



```

        fid=fopen(fullfilename, 'wt');           % Opens the file and tells
matlab to write and/or create the file
        for b = 1: N,                           % N is the Number of points
            A = num2str(time(b,1), '%E %2.7f'); % Converts the time to a string
with 7 significant numbers and the exponents is a capital E
            B = num2str(Sin1(b,a), '%E %2.7f'); % Converts the sine wave to
string
            C = num2str(Sin2(b,a), '%E %2.7f'); % Converts the 90 deg sine wave
to string
            D = num2str(Pulse(b,a), '%E %2.7f'); % Converts the pulse data to
string
            data = [A ',' B ',' C ',' D];       % Combine the strings into one
and places the , seperators in
            fprintf(fid, [data '\n']);         % Writes the data to a the file
        end;
        fclose(fid);                           % Closes the file to release
the file from memory

        clc;
        display(['Files completed : ', num2str(a), '/', num2str(Nm)]); % Displays
Status
    end;
    cd ..

%% Avegrages the 100 pulses
PulseAvg = Pulse(:,1);
for c = 2 : Nm,
    PulseAvg = Pulse(:,c)+PulseAvg;
end;
PulseAvg = PulseAvg/Nm;

Points = find((time >= 17e-9)&((time <= 30e-9)));
Pulse1 = Pulse(:,1);

if filePick == 1,
    save PulseNoSRD.mat N Nm Points Pulse1 PulseAvg time
elseif filePick == 2,
    save PulseSRD.mat N Nm Points Pulse1 PulseAvg time
end;

```

This section of code processes the results from the TBC

```

% TBC Result process
% -----
% Jaco Badenhorst
% 29th June 2007
%
% This M-File imports TBC data files and averages them so that
% they can be resample to be FFT over a defined time window
%% Start up and clear all bases

% Standard Memory wipe and graph close
clear all;
close all;
clc;

HomePath = cd;
filePick = 2;

```

```

% -----
%% Setup and directory change
cd B:\M_Work\Matlab\ScopeMeas\27-06-07\TBC\Corrected28June07

% Number of points
N = 4096;
% Number of waveforms
M = 100;
% Number of points for the FFT
Nfft = 2^8;
% Beginning of "Window" time
timeDb = 17; %ns

% End of "Window" time
timeDe = 32.4747; %ns
% Beginning of FFt "Window" time
timeB = (timeDb+1)*1e-9;
% End of FFT "Window" time
timeE = (timeDe-1)*1e-9;
% Sets the size and position for the figures
Fsize = [ 560.0000e+000  528.0000e+000  560.0000e+000  420.0000e+000];
% -----
%% Figure Setup
LabelX = 'Time [ns]';
LabelY = 'Amplitude [V]';
Units = 1e9;
% -----
%% Start of loop for all the files.
for a = 1 : M,
%% opening of TBC file and clearing the header
% Picks the correct data files
    if filePick == 2
        fileName = ['TBC_data_SRD_', num2str(a), '.dat'];
    elseif filePick == 1
        fileName = ['TBC_data_', num2str(a), '.dat'];
    end;
% Opens the file
    FileId = fopen(fileName);
    LineData = deblank(fgetl(FileId));
    textF = 1;
% this part of the programs clears the header file of the TBC
    while textF == 1,
        textF = 0;
        if LineData(1) == '!'
            textF = 1;
        else
            break;
        end;
        LineData = fgetl(FileId);
    end;
%% Wave form Extraction
% The following section extracts the data from each of the TBC files
    c = 0;
    while true,
        if ~ischar(LineData),
            break
        end;
        c = c+1;
        LineData = sscanf(LineData, '%f');
        DataVec(c, :, a) = LineData(2:3);
        LineData = fgetl(FileId);
    end;
end;

```

```

    end;
    fclose(FileId);

%% end of the for loop
end;
% -----
%% Collects the TBC Averaged data
clear a;

if filePick == 2
    fileName = 'TBC_data_SRD_interpolated.dat';
elseif filePick == 1
    fileName = 'TBC_data_interpolated.dat';
end;
FileId = fopen(fileName);
LineData = deblank(fgetl(FileId));
textF = 1;
while textF == 1,
    textF = 0;
    if LineData(1) == '!'
        textF = 1;
    else
        break;
    end;
    LineData = fgetl(FileId);
end;
c = 0;
while true,
    if ~ischar(LineData),
        break
    end;
    c = c+1;
    LineData = sscanf(LineData,'%f');
    DataVec(c,:,M+1) = LineData;
    LineData = fgetl(FileId);
end;
fclose(FileId);
% -----
%% Returns to working Dir for storage of data
% Clears variables not used anymore
clear FileId LineData c textF fileName a

cd(HomePath);
% Clears variables not used anymore
clear HomePath
% -----
%% Loads the data from the measured waveforms and draws the final graphs

% Picks a "Default" waveform
Mainwave = DataVec(:, :, 1);

% Collects the data inside the time window as picked by the user in the
% setup part of the M-file
Test = find((DataVec(:, 1, 1) >= timeDb) & (DataVec(:, 1, 1) <= timeDe));

PulseBegin(:, :, 1) = DataVec(Test(1):Test(1)+1064, :, 1);
Pulse = PulseBegin(:, :, 1);

MainwaveTime = Pulse(:, 1);

```

```

b = 1;

figure('Position',[10 Fsize(2) Fsize(3) Fsize(4)])

plot(PulseBegin(:,1,1)+22,PulseBegin(:,2,1),'^m','MarkerEdgeColor','m',...
      'MarkerFaceColor','m','MarkerSize',5);hold on;
plot(PulseBegin(:,1,1)+22,PulseBegin(:,2,1),'--r','linewidth',2);
plot(Pulse(:,1)+22,Pulse(:,2),'-k','linewidth',3);hold off

title(['Averaged for ',num2str(b),' waveforms']);
xlabel(LabelX);
ylabel(LabelY);
legend(['Waveform # ',num2str(b)],'Original Waveform','Averaged
Waveform',0);
% pause
% Picks the axis for all the graphs
Paxis = axis;

% This section of code averages the TBC data and plots it
if M > 1,
    for b = 2 : M,
        Test = find((DataVec(:,1,b) >= timeDb)&(DataVec(:,1,b) <= timeDe));
        PulseBegin(:,1,b) = DataVec(Test(1):Test(1)+1064,:,b);
        Ttime = DataVec(:,1,b);
        Tpulse = DataVec(:,2,b);
        if b <= M,
            Pulse(:,2) = (Pulse(:,2) +
interplq(Ttime,Tpulse,MainwaveTime));
            end;
        figure(1);

plot(PulseBegin(:,1,b)+22,PulseBegin(:,2,b),'^m','MarkerEdgeColor',...
      'm','MarkerFaceColor','m','MarkerSize',5);hold on;
plot(PulseBegin(:,1,1)+22,PulseBegin(:,2,1),'--r','linewidth',2);
plot(Pulse(:,1)+22,Pulse(:,2)/b,'-k','linewidth',3);hold off;

title(['Averaged for ',num2str(b),' waveforms']);
xlabel(LabelX);
ylabel(LabelY);
legend(['Waveform # ',num2str(b)],'Original Waveform',...
      'Averaged Waveform',0);

axis(Paxis);

end;
end;

Test = find((DataVec(:,1,M+1) >= timeDb)&(DataVec(:,1,M+1) <= timeDe));
PulseAvgTBC = DataVec(Test(1):Test(1)+1064,:,M+1);
% -----
%%
clear DataVec Mainwave Test TPulse ans a b c Tpulse
% Calculates the timescale for FFT samples
timescale = ((timeB+(timeE-timeB)/Nfft) : (timeE-timeB)/Nfft : timeE)';

% Loads the Data from the working directory
if filePick == 1,
    load PulseNoSRD.mat PulseAvg time

```

```

elseif filePick == 2,
    load PulseSRD.mat PulseAvg time
end;

% Finds the points required for the FFT window
Points = find((time >= timeDb/Units)&((time <= timeDe/Units)));

% Windows the data for the FFT
time      = time(Points); PulseAvg = PulseAvg(Points);

% Interpolates the data points for The FFT for both the TBC corrected data
% and the scope averaged waveform
PulseTBCavgfft = interp1q(PulseAvgTBC(:,1)/Units,PulseAvgTBC(:,2),...
    timescale);
PulseAvgfft    = interp1q(time,PulseAvg,timescale);
Pulsefft      = interp1q(Pulse(:,1)/Units,Pulse(:,2)/M,timescale);

% figure(2): Compare the Scope Avg with TBC Avg
figure('Position',[60+Fsize(2) Fsize(2) Fsize(3) Fsize(4)])

plot(time*Units+22,PulseAvg,'-b','linewidth',3);hold on;
plot(Pulse(:,1)+22,Pulse(:,2)/M,'-.k','linewidth',3);hold off;
xlabel(LabelX);
ylabel(LabelY);

% Sets all waveforms to the same size
axis(Paxis)

% figure(3) : Scope averaged waveform
figure('Position',[10 Fsize(2)/8 Fsize(3) Fsize(4)])

plot(time*Units+22,PulseAvg,'-b','linewidth',3);hold on
plot(timescale*Units+22,PulseAvgfft,'-
or','linewidth',1,'MarkerEdgeColor','r',...
    'r','MarkerFaceColor','r','MarkerSize',5);hold off
xlabel(LabelX);
ylabel(LabelY);
% Sets all waveforms to the same size
axis(Paxis)

% figure(4) : TBC waveform
figure('Position',[60+Fsize(2) Fsize(2)/8 Fsize(3) Fsize(4)])

plot(Pulse(:,1)+22,Pulse(:,2)/M,'-.k','linewidth',3);hold on;
plot(timescale*1e9+22,Pulsefft,'-
or','linewidth',1,'MarkerEdgeColor','r',...
    'MarkerFaceColor','r','MarkerSize',5);hold off;
xlabel(LabelX);
ylabel(LabelY);
% Sets all waveforms to the same size
axis(Paxis)
% -----
%% Final Save and Figure Labeling
Pulse(:,2) = Pulse(:,2)/M;

clear DataVec FileId Fsize HomePath LineData M N Points Mainwave
clear MainwaveTime Test TPulse Ttime ans a b c textF Tpulse fileName
clear LabelX LabelY Paxis timeB timeDb timeDe timeE PulseBegin

```

```

if filePick == 1,
    save('TBC_Corrected.mat')
elseif filePick == 2,
    save('TBC_Corrected_SRD.mat')
end;

figure(4)
title('a.) TBC Corrected Pulse with the FFT samples');
legend('TBC corrected and averaged',[num2str(Nfft),' FFT Samples'],1);

figure(3)
title('b.) Impulse 100 time averaged on sampling scope with FFT samples');
legend('100 scope averaged',[num2str(Nfft),' FFT Samples'],1);

figure(1)

figure(2)
title('Scope Averaged and TBC corrected Impulse');
legend('Scope Averaged','TBC corrected Waveform',1);
% -----

```

This code processes the FFT results

```

% TBC FFT process
% -----
% Jaco Badenhorst
% 29th June 2007
%
% This M-File imports TBC processed data files and compares the FFT's

%% Start up and clear all bases and pick data file

% Standard Memory wipe and graph close
clear all;
close all;
clc;

%The datafile as well as the amount of Zeroes
filePick = 2;
Z        = 2^11;

% -----
%% Setup and file load

if filePick == 1,
    load TBC_Corrected.mat
elseif filePick == 2,
    load TBC_Corrected_SRD.mat
end;

timescale = (timescale - timescale(1));

TBCWaveform = PulseTBCAvgfft;

```

```

ScopeWaveform = PulseAvgfft;

save temp.mat ScopeWaveform TBCWaveform Nfft filePick timescale Units Z

clear all

load temp.mat; delete temp.mat;

if Units == 1e12,
    Xunit = 'ps';
    Funit = 'GHz';
    Funits = 1e9;
elseif Units == 1e9
    Xunit = 'ns';
    Funit = 'GHz';
    Funits = Units;
elseif Units == 1e6,
    Xunit = '\mus';
    Funit = 'MHz';
    Funits = Units;
else
    Xunit = '';
end;

% -----
%% Ensures the data are all the same length
NaNpoints = find(isnan(TBCWaveform)==1);
if NaNpoints ~= 1,
    TBCWaveform(NaNpoints,1) = zeros(length(NaNpoints),1);
end;

figure(1)

plot(timescale*Units,TBCWaveform,'sk'); hold on
plot(timescale*Units,ScopeWaveform,'ob'); hold off

title(['The ',num2str(Nfft),' samples for the FFT']);
legend('TBC samlpes','Scope avgerage',1)

xlabel(['Time [',Xunit,']']);
ylabel('Amplitude [V]');
% -----
%% Frequency range
clear NaNpoints

tmax = max(timescale);
fmax = 1/tmax*Nfft;

f = linspace(0,fmax,Nfft+Z);
% -----
%% FFT
clear tmax fmax

ScopeWaveform_fft = fft([ScopeWaveform; zeros(Z,1)]);
TBCWaveform_fft = fft([TBCWaveform; zeros(Z,1)]);
FFT_points = (Nfft+Z)/2;

```

```

TBCWaveformPhase = 180*unwrap(angle(TBCWaveform_fft(1:FFT_points)))/pi;
ScopeWaveformPhase = 180*unwrap(angle(ScopeWaveform_fft(1:FFT_points)))/pi;

m = (TBCWaveformPhase(ceil(length(TBCWaveformPhase)/2))-...
     TBCWaveformPhase(1))/(ceil(length(TBCWaveformPhase)/2)-1);

y = m*(1:length(TBCWaveformPhase));

TBCWaveformPhase = TBCWaveformPhase-y';

m = (ScopeWaveformPhase(ceil(length(ScopeWaveformPhase)/2))-...
     ScopeWaveformPhase(1))/(ceil(length(ScopeWaveformPhase)/2)-1);

y = m*(1:length(TBCWaveformPhase));

ScopeWaveformPhase = ScopeWaveformPhase-y';

TBCWaveform_fft = 20*log10(abs(TBCWaveform_fft(1:FFT_points)));
ScopeWaveform_fft = 20*log10(abs(ScopeWaveform_fft(1:FFT_points)));
clear m y
% -----
%% Plot

figure(2);
subplot(2,1,1);
plot(f(1:FFT_points)/Funits,TBCWaveform_fft,'-k','linewidth',2); hold on
plot(f(1:FFT_points)/Funits,ScopeWaveform_fft,':b','linewidth',3);
hold off;
test = axis;
axis([0 6 test(3) test(4)]);
if filePick == 1,
    title(['Spectra of the impulse without a SRD at the output and ',...
          num2str(Z),' zero padded']);

elseif filePick == 2,
    title(['Spectra of the impulse with a SRD at the output and ',...
          num2str(Z),' zero padded']);
end;
ylabel('Magnitude [dB_V]');
xlabel('Frequency [GHz]');
legend('TBC and averaged','Scope averaged',3);
subplot(2,1,2);
plot(f(1:FFT_points)/Funits,TBCWaveformPhase,'-k','linewidth',2);hold on
plot(f(1:FFT_points)/Funits,ScopeWaveformPhase,':b','linewidth',3);
hold off;
test = axis;
axis([0 6 -500 1000]);

ylabel('Linearised Phase [deg]');
xlabel('Frequency [GHz]');
% -----
clear Nfft Funits ScopeWaveform

```


Appendix E: TBC corrected Impulse with SRD

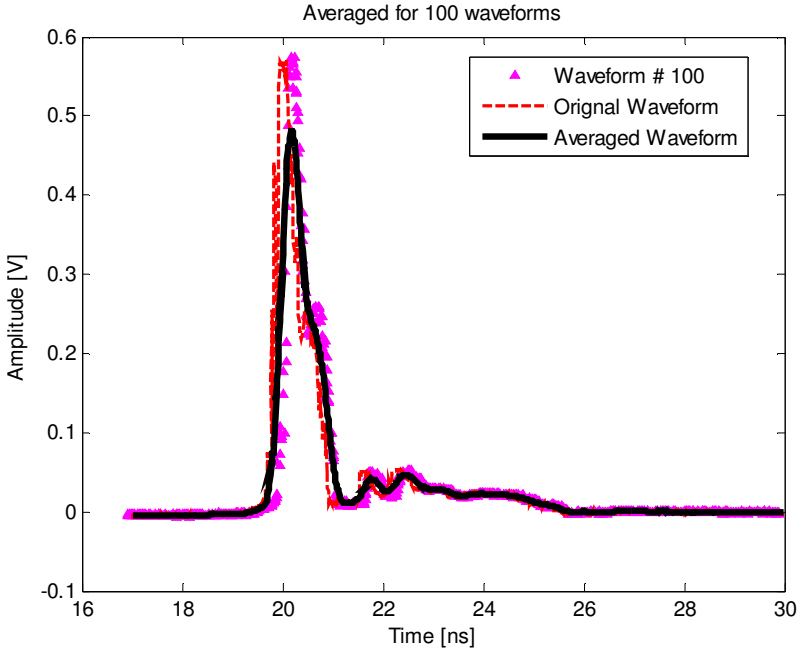


Figure A 5: A graph showing the original waveform (dashed), the 100th waveform and the averaged waveform (solid line), for this impulse a SRD was added to the output of the IGen

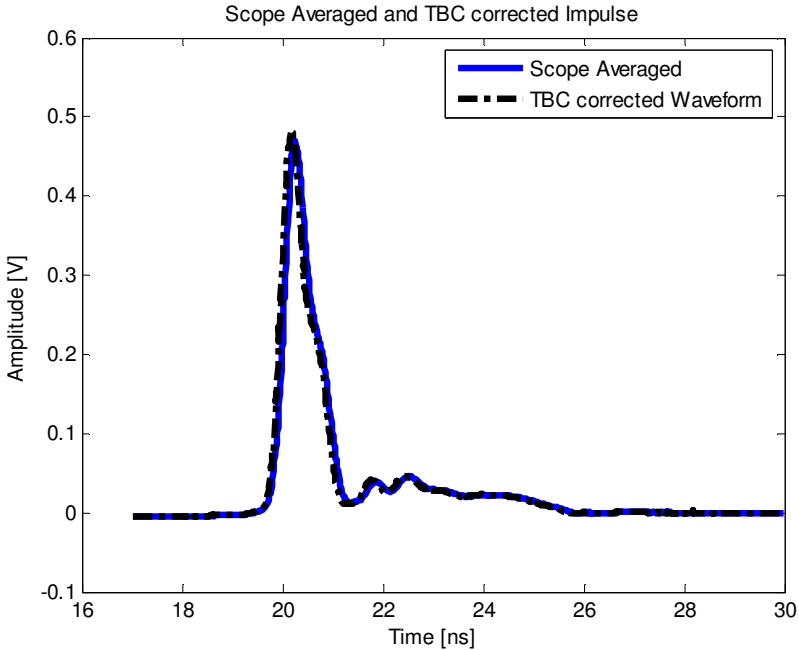


Figure A 6: The solid line represents the scope averaged waveform, while the dot dash line represents the TBC corrected and averaged waveform. From this graph the phase difference between the two sets of data is not as clearly seen as in Figure 5-11

Appendix F: Results for the parameter sweep from section 6.2.2

Results for width sweep (D_s)

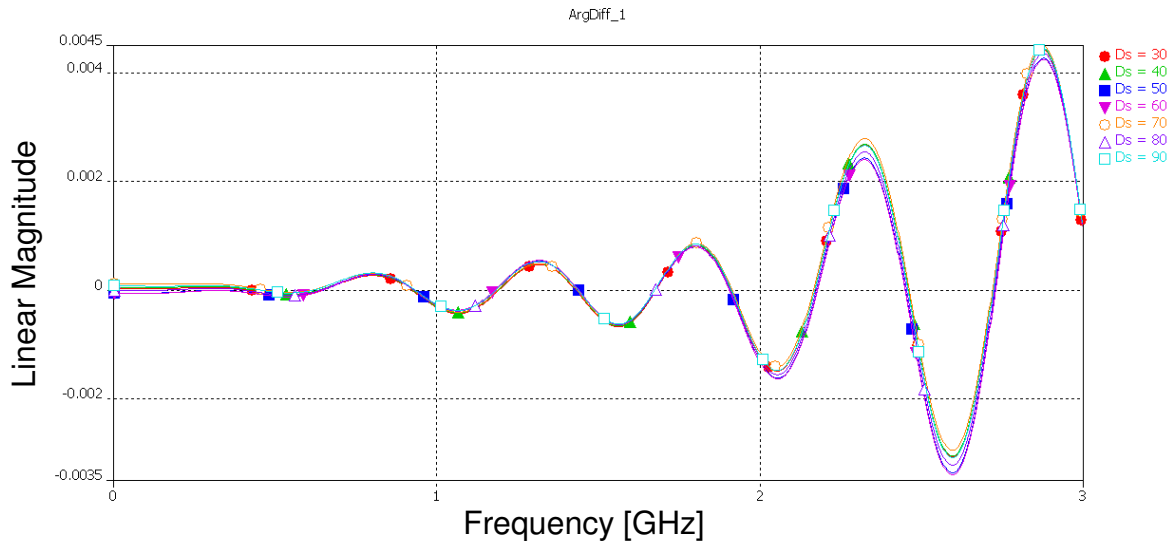


Figure A 7: Magnitude difference for the values of D_s shown in the legend

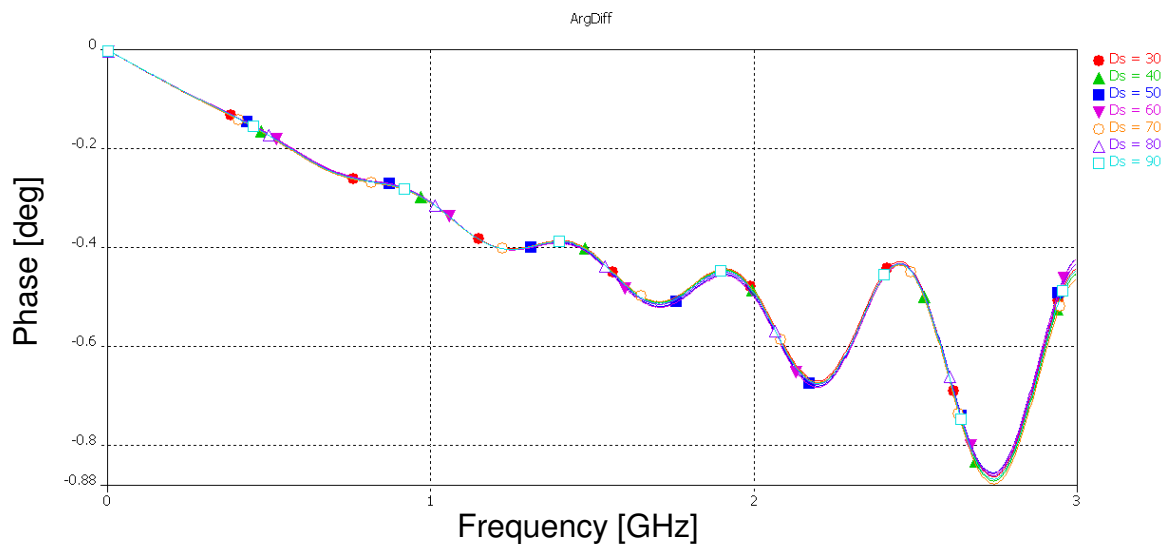


Figure A 8: Phase difference for the values of D_s shown in the legend

Results for height sweep (S)

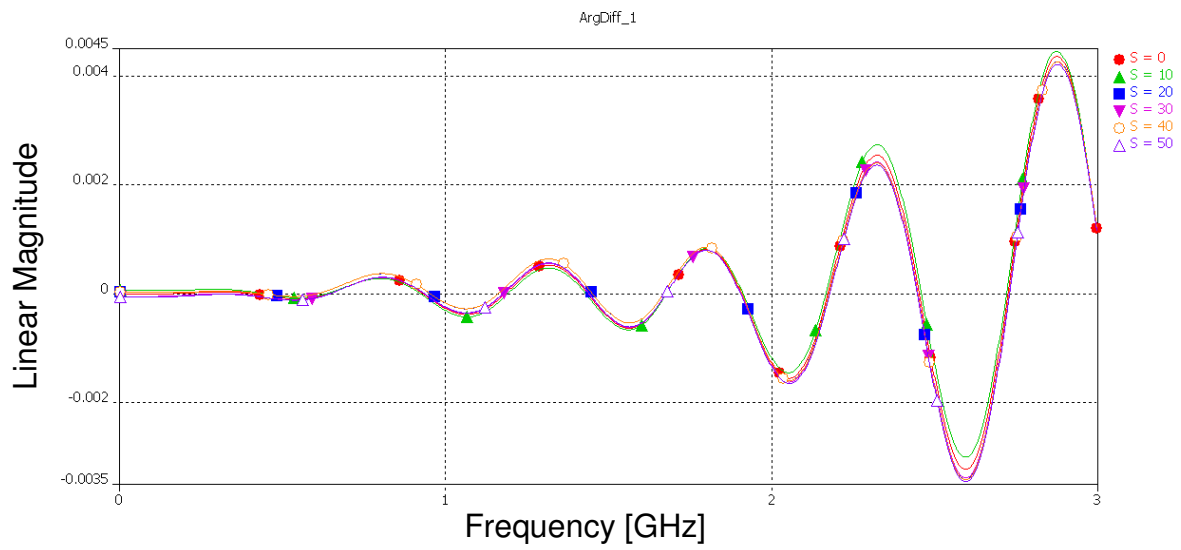


Figure A 9: Magnitude difference for the values of S shown in the legend

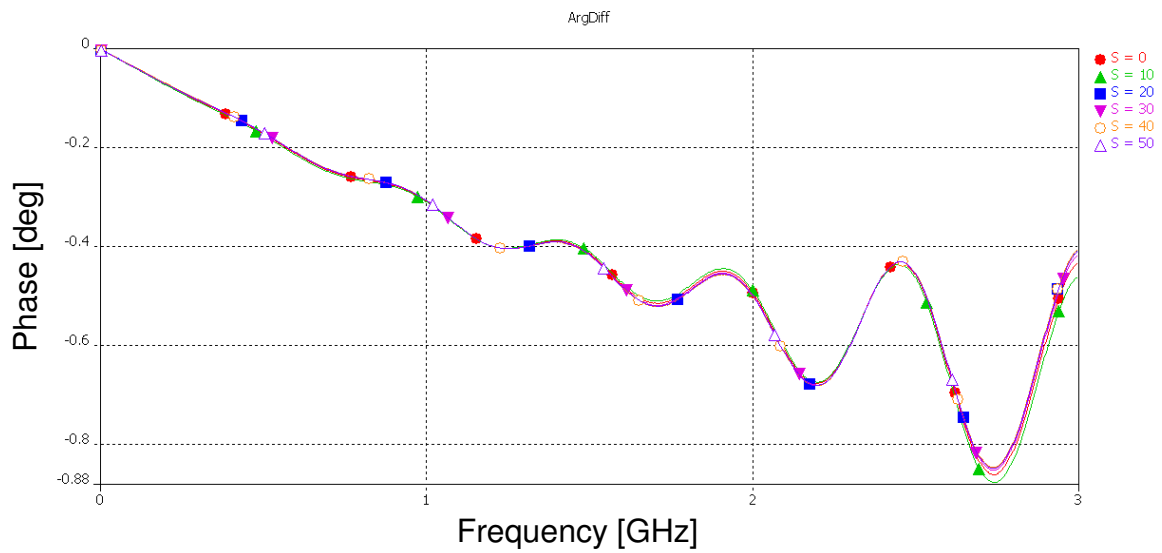


Figure A 10: Phase difference for the values of S shown in the legend

Appendix G: Frequency-domain results for Chapter 6

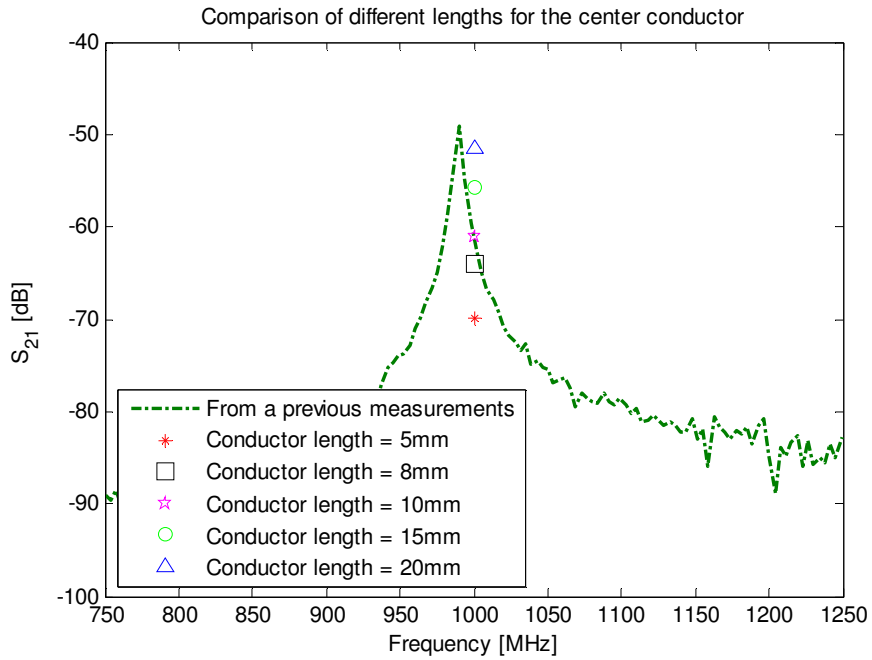


Figure A 11: The S_{21} measured for the Fprobe when the length of the probe is cut back from 20mm to 5 mm which were used for the measurements of on the 8510

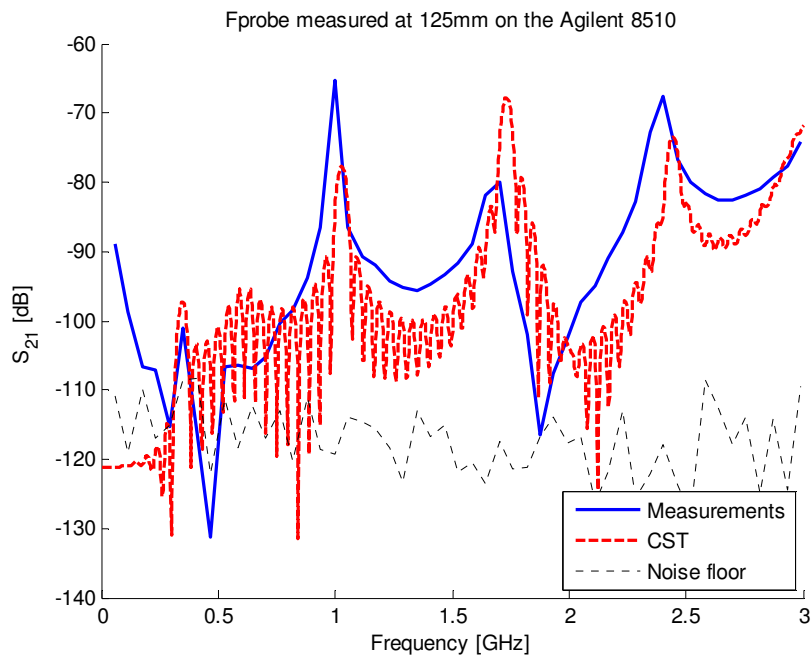


Figure A 12: CST simulated data compared to the 8510 measurement while the Fprobe is at P4

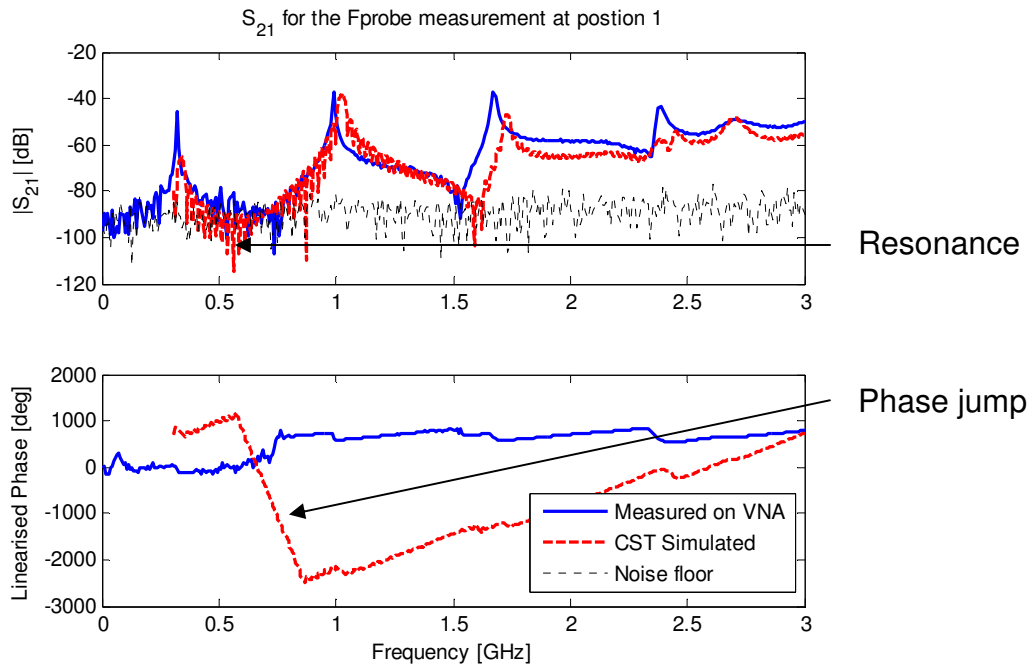


Figure A 13: The measured S_{21} for the Fprobe using the VNA when the Fprobe is at P1

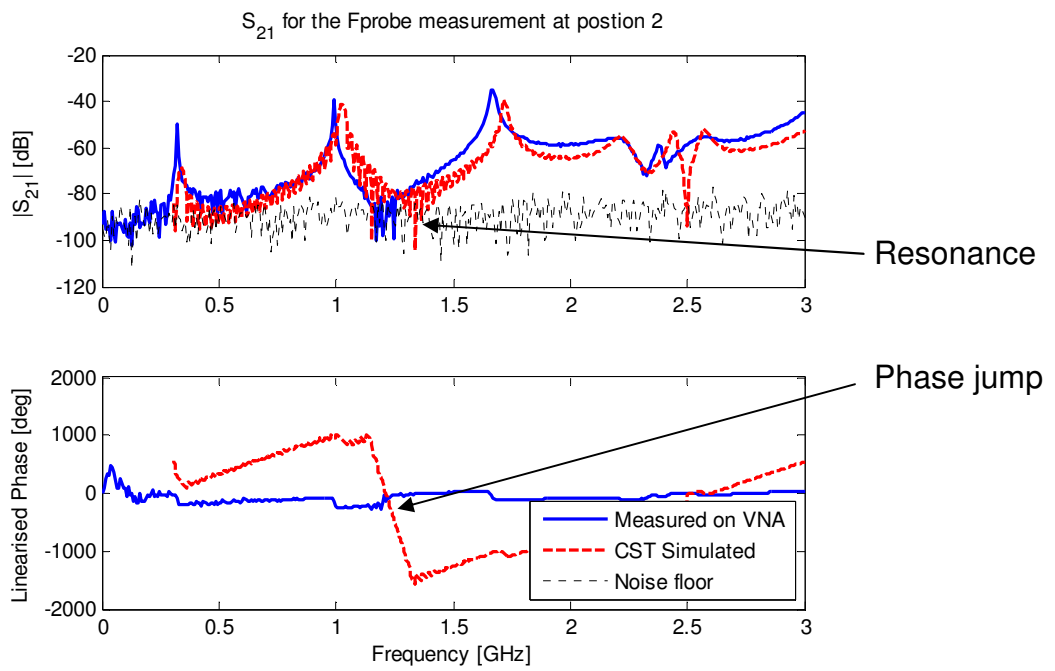


Figure A 14: The measured S_{21} for the Fprobe using the VNA when the Fprobe is at P2

Both Figure A 13 and Figure A 14 has a resonance in the simulated results. This is contributed to how the simulation solver conditions. The simulation was purposely set to calculate results for 40ns.

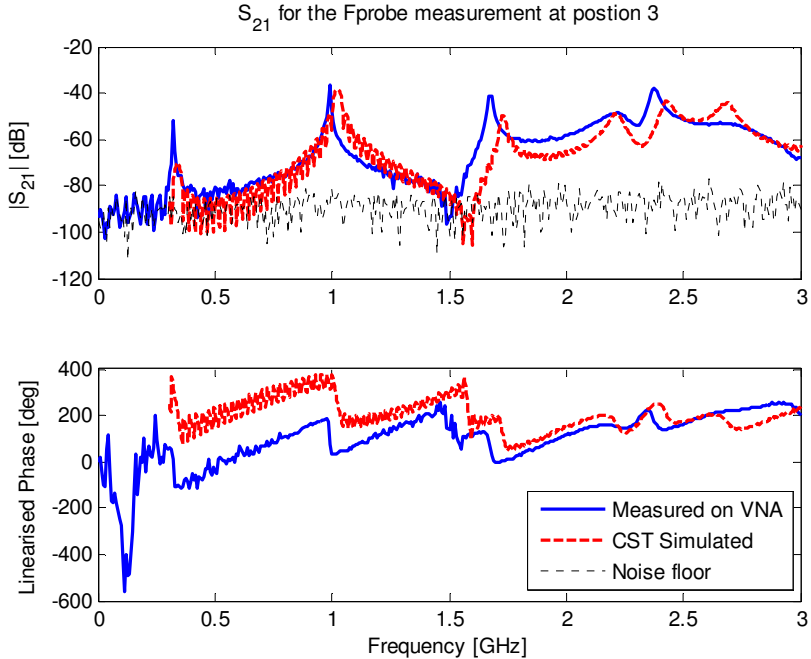


Figure A 15: The measured S₂₁ for the Fprobe using the VNA when the Probe is at P3

Appendix H: Time-domain results for Chapter 6

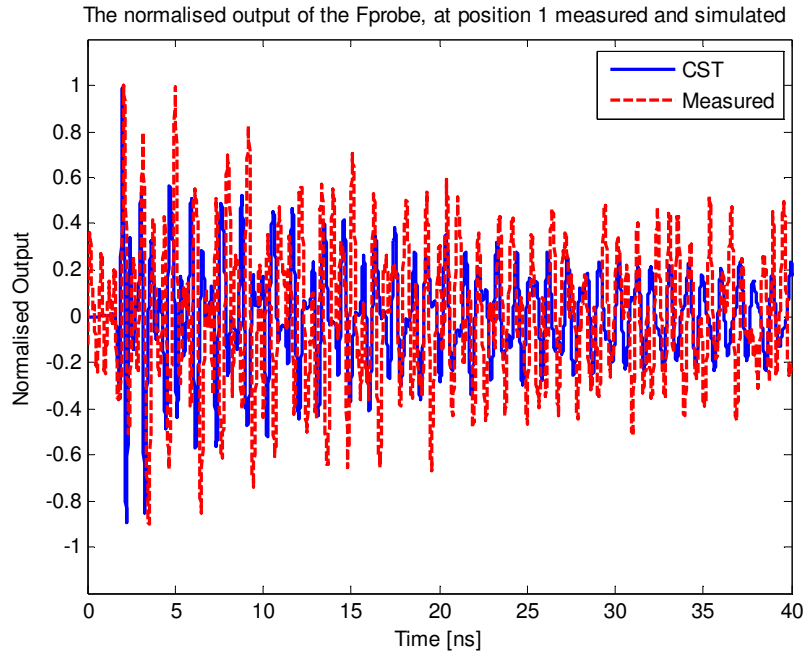


Figure A 16: Time signal measured on the sampling scope for the Fprobe at P1

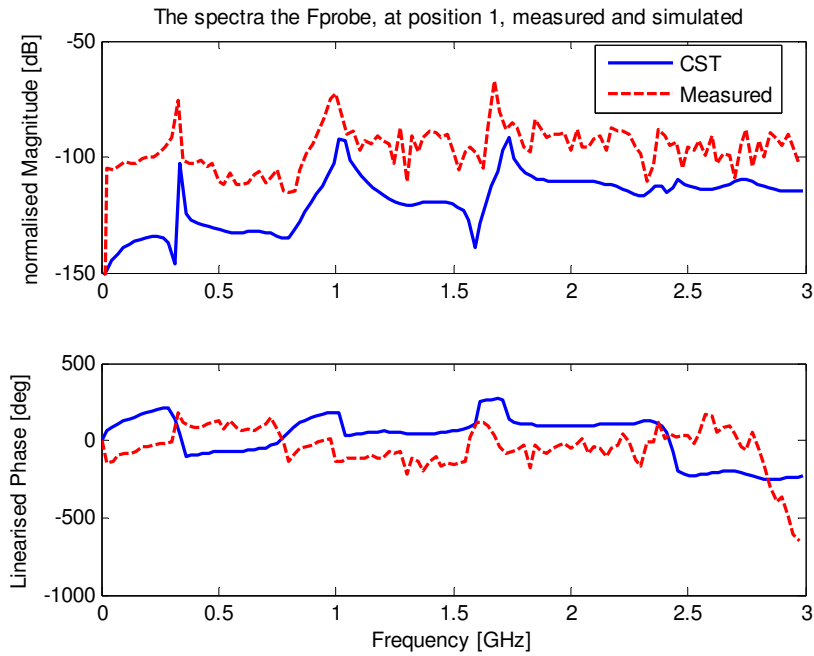


Figure A 17: Spectra for the signal measured at P1

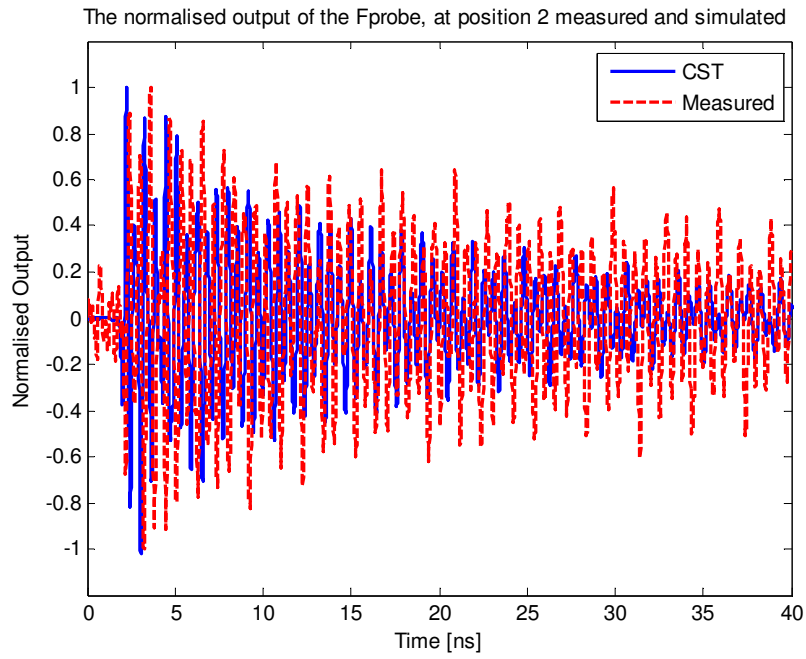


Figure A 18: signal measured on the sampling scope for the Fprobe at P2

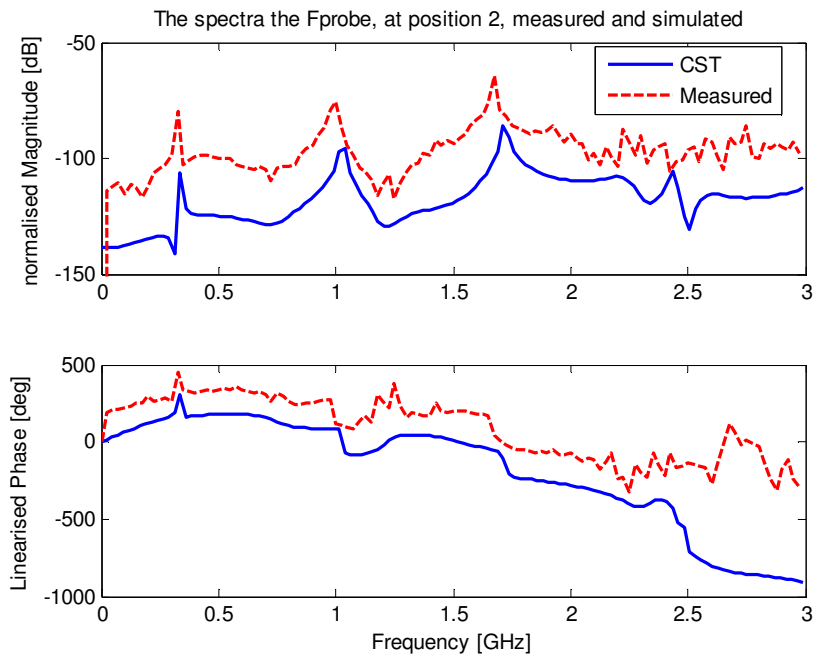


Figure A 19: Spectra for the signal measured at P2

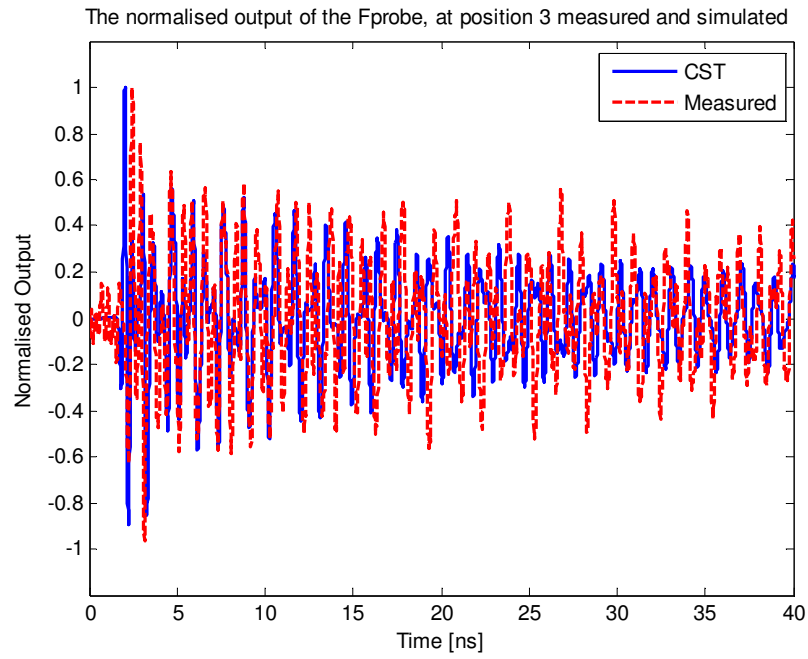


Figure A 20: signal measured on the sampling scope for the Fprobe at P3

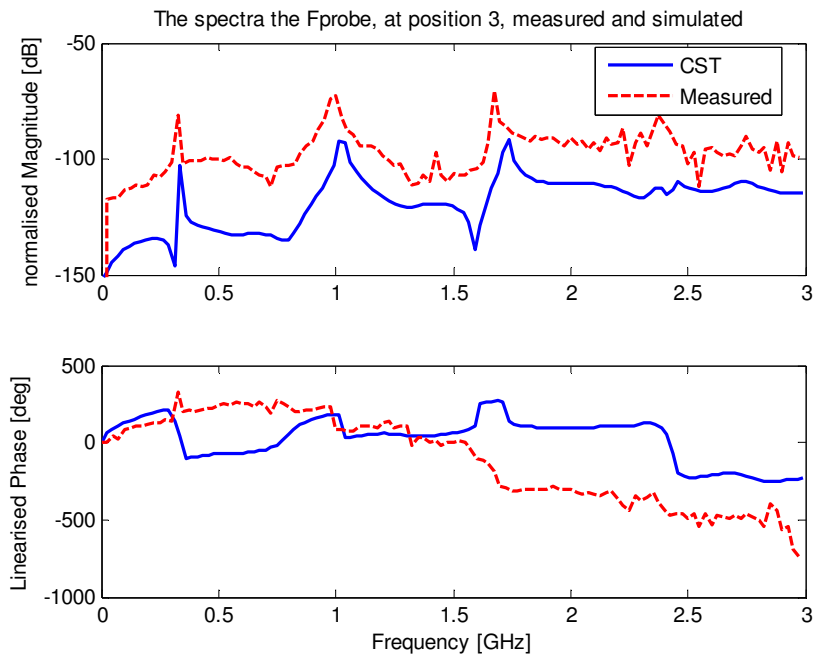
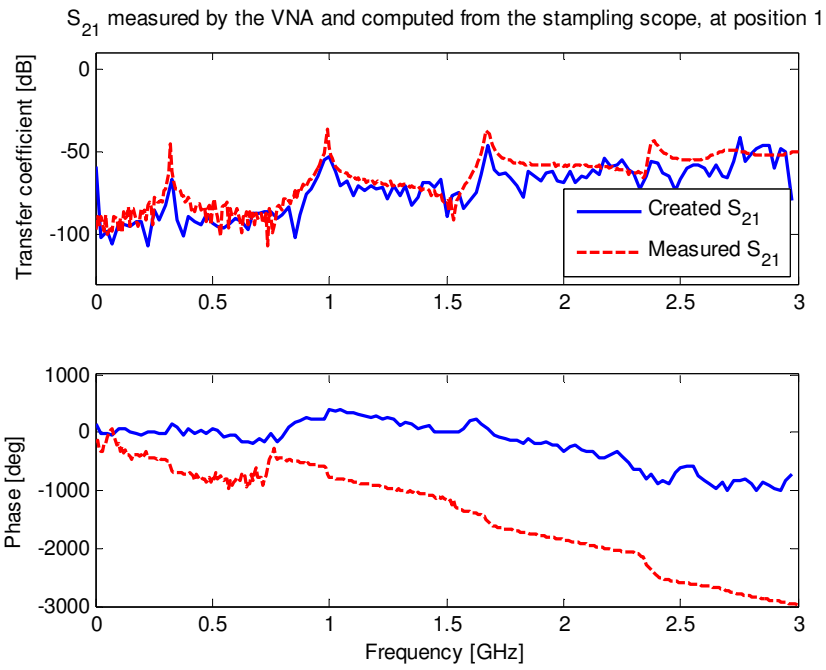


Figure A 21: Spectra for the signal measured at P3



9

Figure A 22: The S_{21} calculated on the sampling scope compared to the measured result from the VNA at P1

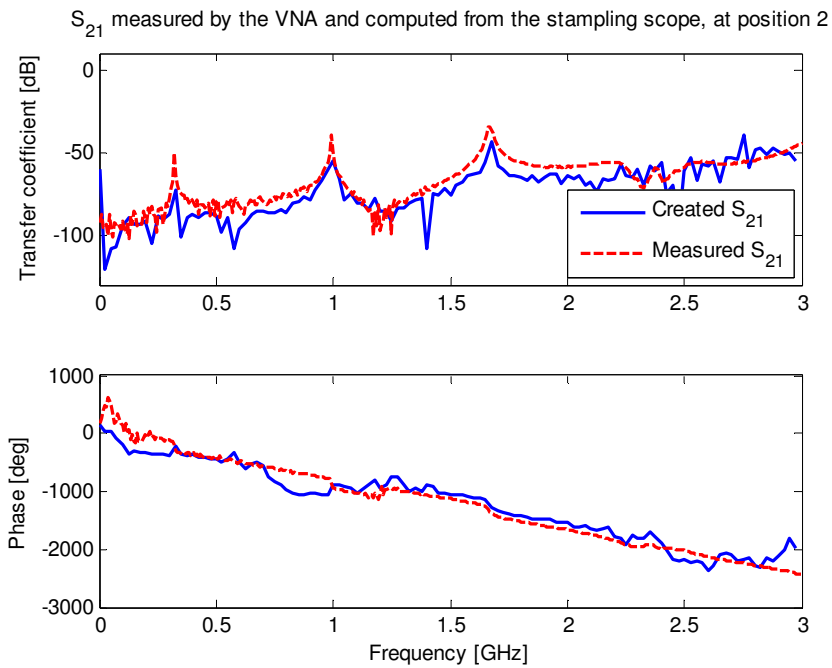


Figure A 23: The S_{21} calculated on the sampling scope compared to the measured result from the VNA at P2

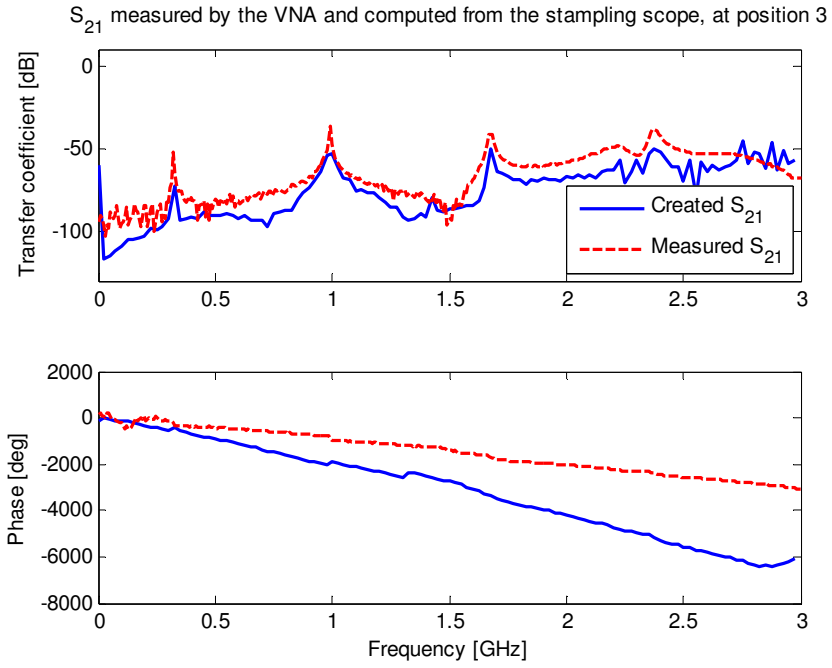


Figure A 24: The S_{21} calculated on the sampling scope compared to the measured result from the VNA at P3

Appendix I: Final results for the sampling scope compared to the VNA

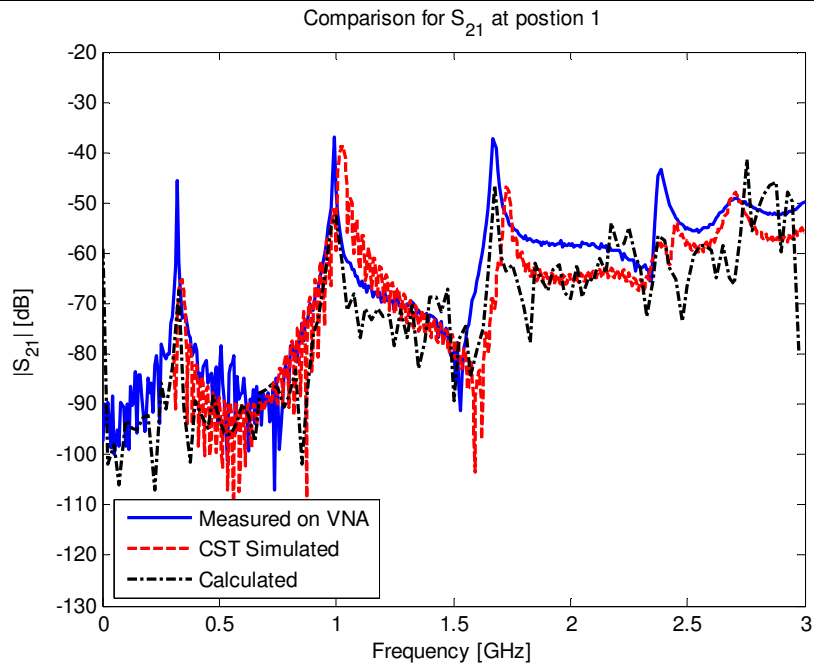


Figure A 25: Compared S_{21} for the calculated, measured and simulated results for the Fprobe at P1

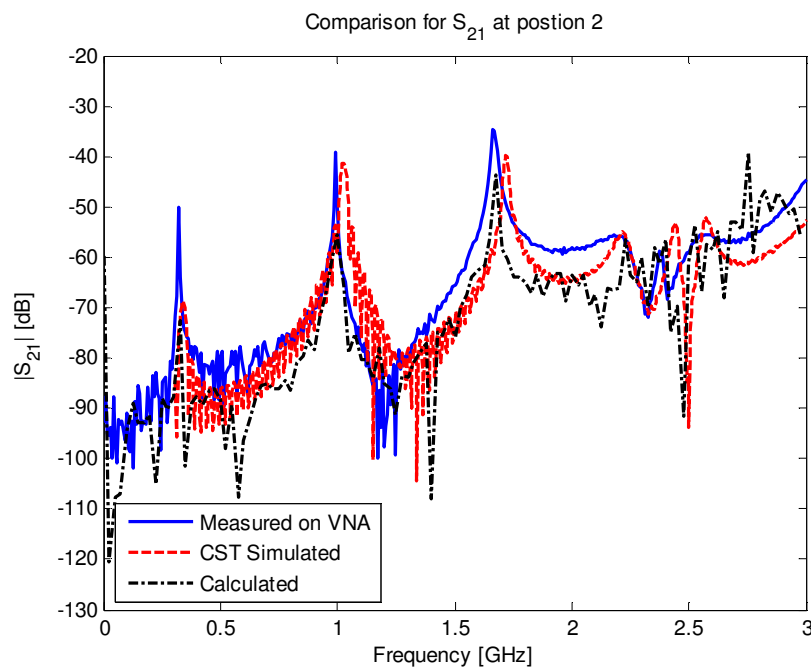


Figure A 26: Compared S_{21} for the calculated, measured and simulated results for the Fprobe at P2

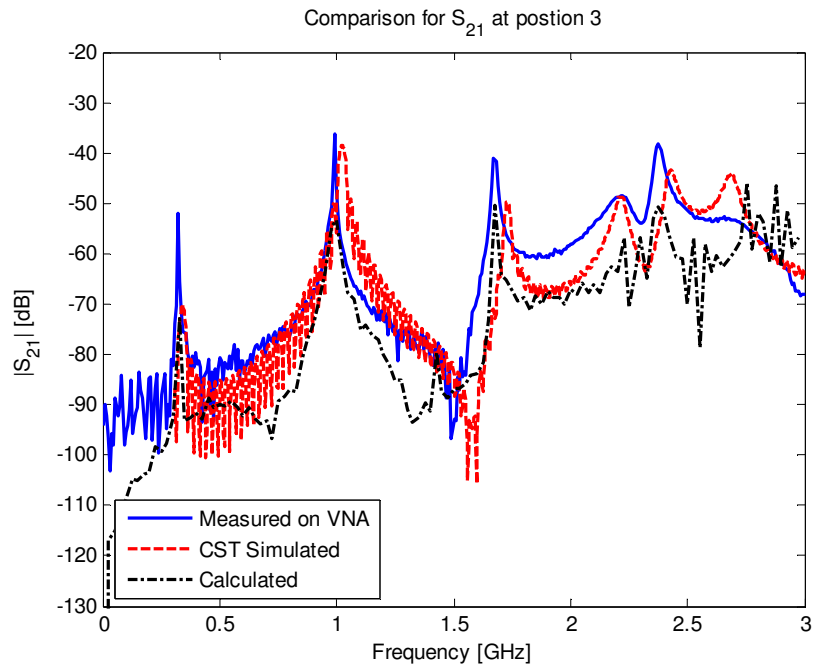


Figure A 27: Compared S_{21} for the calculated, measured and simulated results for the Fprobe at P3